

POLITECNICO DI TORINO

Corso di Laurea Magistrale in Ingegneria Energetica e Nucleare

Tesi di Laurea Magistrale

**Safer Lithium-Metal Batteries through
Lithium Protection and
Thermal-Electrochemical Modelling**



Relatori

prof. Massimo Santarelli

prof. Silvia Bodoardo

prof. Domenico Ferrero

Candidato

Sabrina Trano

Marzo 2021

Safer Lithium-Metal Batteries through Lithium Protection and Thermal-Electrochemical Modelling

Sabrina Trano

Marzo 2021

Abstract

In the perspective of the energy transition, both market field and research communities recognised the electric energy storage as the main medium for this purpose. Specifically speaking, lithium ion batteries are already one of the technologies of choice to accomplish the road-transport electrification. Indeed, this work is devoted to the study of a high energy density cell technology. The latter is the most important requirement for an Electric Vehicle, and it can be achieved thanks to a high voltage cathode combined with a very high capacity anode. In the light of this, in this work a $Ni_{0.6}Mn_{0.2}Co_{0.2}O_2$ electrode, whose specific energy can reach 175 Wh/kg, was chosen as cathode, while lithium metal foil has been exploited as anode, since it shows the outstanding specific capacity of 3860 Ah/kg and the lowest electrochemical potential (-3.040 V vs SHE). To better investigate such electrochemical system, and make it safer, in this work are addressed two leading issues: the mathematical modelling and the lithium protection. The former is a smart and effective tool in the drive toward developing better, safer and durable batteries. Herein, a thermal-electrochemical model was implemented in finite element package Comsol Multiphysics 5.5. This model takes advantage of the coupling of macro and microscale descriptions: the first one describes charges and species transport in solid and liquid phases of both porous electrodes and electrolyte. Lithium concentrations and electrochemical potentials are assumed to depend only on the spatial coordinate x along the cell thickness. The microscopic field deals with the lithium intercalation, which depends on the radial dimension of a spheric electrode particle sited at some spatial location along x . This pseudo dimension combined with the 1D, is called the pseudo two dimensional (P2D) model. Relying on the porous electrode theory, Li-ions and charges transport are described by Fick's and Ohm's law, respectively. Governing equations for concentrations and potentials are the conservation of mass and charge which are coupled at the solid-liquid interface by the Butler-Volmer equation. Transport and intercalation phenomena generate heat, which is calculated in the P2D model and then inserted in a 3D thermal model where the average temperature of the cell is computed. The last one is thereby implemented in the first model to update thermodynamic and kinetic variables. In order to run close simulations, physical, chemical and kinetic properties have been experimentally evaluated or extracted from literature. Once the materials have been fully parametrized, the model has been launched for the validation phase at different C-rates. A second part of the thesis focuses on the protection of the lithium anode. Since it is thermodynamically unstable, as soon as it is immersed in the electrolyte, they react forming

an heterogeneous film named Solid-Electrolyte Interphase (SEI). On the protrusion of this layer, Li-ions reduce forming dendrites which can reach the cathode, causing short circuits and thus thermal runaways. A solution proposed in this work to avoid this escalation is a methacrylate-based polymer electrolyte, in which zirconia nanoparticles are added, and liquid EC:DEC LiPF₆ 1M has impregnated it. The addition of inorganic material is for a higher Young's modulus of the resulting Composite Gel Polymer Electrolyte (CGPE), which can suppress the dendrite growth, along with the absence of crystalline phase which enhances the electrolyte conductivity. The proposed membrane has been physically and electrochemically characterized, giving back encouraging results of high conductivity, transference number and uniform plating. Hence, a full cell improved with the composite membrane has been further implemented and studied.

Contents

Abstract	2
Acronyms	7
List of Figures	8
List of Tables	12
1 Introduction	13
1.1 Electrochemical storage	14
1.2 Lithium ion battery	15
1.3 Lithium metal battery	20
1.4 Steps of this work	24
2 Modelling	27
2.1 The electrochemical model	30
2.2 The thermal coupling	36
2.3 Model parameters	38
2.3.1 Geometric parameters	38
2.3.2 Particle radius	39
2.3.3 Cell assembly	40
2.3.4 Diffusion coefficient	41
2.3.5 Equilibrium Electrode Potential	44
2.3.6 Entropy factor	46
2.3.7 Electrode volume fraction	47
2.3.8 Exchange current density	47

2.3.9	Physico-chemical parameters from literature	50
2.3.10	Thermal-model parameters	51
2.4	Model results and validation	54
2.4.1	Electrochemical validation	54
2.4.2	Thermal analysis	56
3	Lithium protection	59
3.1	Composite Gel Polymer Electrolyte	61
3.1.1	Materials of interest	62
3.1.2	Membrane synthesis	66
3.1.3	Membrane preparation	66
3.2	Physical-chemical characterization	67
3.2.1	Thermogravimetric Analysis	67
3.2.2	Fourier transform infrared spectroscopy	70
3.2.3	FESEM Scanning	72
3.2.4	X-Ray Diffraction	74
3.3	Electrochemical characterization	76
3.3.1	Electrochemical impedance spectroscopy	76
3.3.2	Linear sweep voltammetry	78
3.3.3	Chronoamperometry and EIS	79
3.3.4	Galvanostatic cycling and EIS	81
3.4	Cell cycling	85
4	Conclusions	91
	Bibliography	95

Acronyms

EES	Electric Energy Storage
V2G	Vehicle to Grid
EV	Electric Vehicle
BEV	Battery Electric Vehicle
HEV	Hybrid Electric Vehicle
PHEV	Plug-in Hybrid Electric Vehicle
SEI	Solid Electrolyte Interphase
LCO	Lithium cobalt oxide
LMO	Lithium manganese oxide
LFP	Lithium iron phosphate
SOC	State of Charge
NCA	Lithium nickel cobalt aluminium oxide
NMC	Lithium nickel manganese cobalt oxide
GHG	Greenhouse gas
OCV	Open Circuit Voltage
LUMO	Lowest unoccupied molecular orbital
HOMO	Highest occupied molecular orbital
SHE	Standard Hydrogen Electrode
P2D	Pseudo-two-Dimensional
EC:DEC	Ethylene carbonate:diethyl carbonate
FESEM	Field Emission Scanning Electron Microscopy
GITT	Galvanostatic Intermittent Titration Technique
EIS	Electrochemical Impedance Spectroscopy
DSC	Differential Scanning Calorimetry
BMA	Butyl methacrylate
PEGDA	Poly(ethylene glycol)diacrylate
CGPE	Composite Gel Polymer Electrolyte
TGA	Thermogravimetric analysis
FTIR	Fourier Transform Infrared Spectroscopy
XRD	X-ray Diffraction

LSV	Linear Sweep Voltammetry
BMS	Battery Management System
SOH	State of Health
SPM	Single Particle Model
PDE	Partial differential equation
FEM	Finite Element Method
CPE	Constant Phase Element
DOD	Depth of Discharge
PEO	Polyethylene oxide
SPW	Solvent-free Polymer Electrolyte
GPE	Gel Polymer Electrolyte
CPE	Composite Polymer Electrolyte
BPO	Benzoyl peroxide
MIR	Mid infrared
ATR	Attenuated total reflection
PITT	Potentiostatic Intermittent Titration Technique
WT	Weight

List of Figures

1.1	Comparison of different Electric Energy Storages based on their specific power, energy and storage weight [3]	14
1.2	Schematic overview of LCO characteristics.	17
1.3	Schematic overview of LMO characteristics.	18
1.4	Schematic overview of LFP characteristics.	18
1.5	Schematic overview of NCA (a) and NMC(b) characteristics.	19
1.6	Mosaic structure of the SEI [9]	21
1.7	Formation and growth of lithium dendrites [8]	22
2.1	Schematic representation of a liquid organic electrolyte Li-metal cell [17]	28
2.2	General classification of Li-ion models [18]	30
2.3	Li-metal battery P2D model scheme. Modified figure from [18]	31
2.4	Scheme of the inner part of any kind of cell	37
2.5	xz view of meshed coin cell	38
2.6	FESEM picture of NMC622	39
2.7	Schematic assembly of a El-Cell, which is used from now in experimental parametrization and electrochemical characterization	40
2.8	Potential vs time curve of performed GITT on the cell	41
2.9	Discharging pulse [26]	42
2.10	Result of GITT (a) in temperature dependence (b) in logarithmic scale vs 1000/T	44
2.11	Variation of NMC622 equilibrium potential with increasing stoichiometry	45
2.12	Entropy coefficient vs SOC	46
2.13	Example of a Nyquist plot	48
2.14	EIS spectra for NMC cathode at different temperature.	49

2.15	Equivalent circuit proposed for this EIS spectra fitting.	50
2.16	NMC622 result curves for TGA (a) and DSC (b), thermal stability interval is outlined by vertical dashed lines.	53
2.17	Voltage profiles of direct measurements (blue line) and model results (orange line) at C/10 (a) and C/5 (b)	55
2.18	Voltage profiles of direct measurements (blue line) and model results (orange line) at C/10 (a) and C/5 (b)	56
2.19	Temperature profile for simulations at 1C (blue line), C/5 (orange line) and C/10 (grey line)	57
2.20	Evolution of average temperature in the cell volume throughout the discharge phase.	58
3.1	Pioneering development of polymer electrolyte throughout the years [39]	60
3.2	Composite Gel Polymer Electrolyte	62
3.3	Structural formula of BPO	63
3.4	3D representation and structural formula of BMA. The Vinyl group has been underlined	64
3.5	Schematic segmental motion of Li ions typical of ethers, including PEGDA [30]	65
3.6	3D representation and structural formula of PEGDA. The two Vinyl group has been underlined	65
3.7	Schematic polymerization. Since PEGDA chain are characterized by two Vinyl group both of them can bond themselves with another BMA or PEGDA creating a network: this is the cross-linking	66
3.8	GloveBox MBrau® UNIlab plus model	67
3.9	Evidence of translucent appearance and flexibility being blend of blank BMA10PEGDA(a,c), BMA10PEGDA38(b,f), BMA10PEGDA63(c,g) and BMA10PEGDA80(d,h)	68
3.10	Weight percentage vs temperature curves of ZrO_2 (orange line),BMA (pink line), PEGDA (blue line), BMA10PEGDA (black line), BMA10PEGDA38 (green line), BMA10PEGDA63 (red line) and BMA10PEGDA80 (violet line).	69
3.11	Absorbance spectrum of monomer BMA (a) and crosslinker PEGDA (b). The peak typical of vinyl group is underlined.	70
3.12	Absorbance spectrum of Zirconia nanoparticles. Infrared radiation don't have enough energy to excite ZrO_2 bonds	71

3.13 FTIR spectra for BMA10PEGDA (a), BMA10PEGDA38 (b), none of them shows the peak at 1630 ascribed to the stretching vibration of C=C bonds.	71
3.14 FTIR spectra BMA10PEGDA63 (a), BMA10PEGDA80 (b), none of them shows the peak at 1630 ascribed to the stretching vibration of C=C bonds.	72
3.15 FESEM picture of pristine ZrO ₂	73
3.16 FESEM images of BMA10PEGDA (a) and BMA10PEGDA80 (b) cross-sections. . .	73
3.17 FESEM images of BMA10PEGDA (a) and BMA10PEGDA80 (b) surfaces.	74
3.18 FESEM images of BMA10PEGDA (a) and BMA10PEGDA80 (b) cross-section, with thickness measurements.	74
3.19 XRD spectra for BMA10PEGDA, with a visible peak in correspondence of 18.80°.	75
3.20 XRD spectra for ZrO ₂ available in the electrochemical laboratory and for ZrO ₂ took from literature.	75
3.21 XRD spectrum for BMA10PEGDA38 (a), BMA10PEGDA63 (b) and BMA10PEGDA80	76
3.22 Ion conductivity results at different temperatures for all the membranes: Celgard (black line), BMA10PEGDA (red line), BMA10PEGDA63 (green line), BMA10PEGDA80 (blue line)	77
3.23 LSV for CPE and Celgard in the potential range from 0 to 6.0 V. Stability window is mapped out with two vertical dashed lines.	79
3.24 Results for the Li Celgard + liquid electrolyte Li of Chronoamperometry (a) and impedance measurement (b) before and after the potential step.	80
3.25 Results for the Li CGPE Li of Chronoamperometry (a) and impedance measurement (b) before and after the potential step.	81
3.26 Results for the Li Celgard + liquid electrolyte Li of Galvanostatic cycling (a) and impedance measurements (b).	83
3.27 Bode graphs of EIS measurements after the short circuit occurred at 1 mAcm ⁻² for the cell with Celgard (a),(c) and the BMA10PEGDA (b),(d).	83
3.28 Results for the Li BMA10PEGDA + liquid electrolyte Li of Galvanostatic cycling (a) and impedance measurements (b).	84
3.29 Results for the Li CGPE Li of Galvanostatic cycling (a) and impedance measurements (b).	84
3.30 Symmetric El-Cel with CGPE cycling for over 200 hours with no short circuit verification.	85

3.31	Voltage profile versus time for the full cell equipped with the CGPE. Results for C-rate of C/10 (purple line) and C/20 (blue line)	86
3.32	Schematic representation of an ideal cell on the left-hand and the intercalation/deintercalation competition causing the voltage noise on the right-hand. Modified figure from [57].	87
3.33	Charge and discharge at 50°C of a full cell with pressed CGPE. No voltage noises are present.	88
3.34	Two full cell equipped with Celgard and pressed CGPE are compared by their capacity density evolution through the cycles.	89

List of Tables

2.1	Geometric parameters	39
2.2	Electrochemical parameters from literature and Comsol library	51
2.3	Density values for all materials and the averaged one.	52
2.4	Specific heat capacity at constant pressure values for all materials and the averaged one.	53
2.5	Thermal conductivity values for all materials and for the perpendicular and parallel conductivity components.	54

Chapter 1

Introduction

Year after year, we are witnessing the symptoms of climate change and thus we are urged to act. Many steps have to be taken and parallel roads to be followed. The energy transition is the path that can lead to the displacement of conventional energy sources in aid of a sustainable mix. A reconceptualization of electricity production, distribution and consumption is required to achieve a clean energy transition. For this purpose, energy storage technologies are our allies number one to rise the biggest challenge of our time: the shift from depletable to sustainable sources of energy. Recently, power grids all around the world, are shifting from a fossil fuel based mix to a one with increasing sustainable suppliers of energy. The exploitation of these fluctuating renewable resources, such as wind and solar irradiation, requires some solution in order to overcome their intermittency while meeting the strict quality criteria of the existing networks. In the electricity grid, balance between consumer demand and power supply has to be maintained. Unfortunately demand profile is characterized by high value only during certain time interval, peaks not always easy to predict, substantial changes in consumer habits and so request for power within season changes as well as geographical location. On the other hand, renewable sources can be predictable but definitely not controllable, like coal and nuclear power plant. Above all, they usually don't fit the demand curve. Electric Energy Storage (EES) already helps us to handle some of these challenges: operational variability, network balancing, optimal demand management. But above all, they can allow us to build a distribution grid in which renewable resources represent the greatest power supplier. They will play a primary role in the scenario of a distribution grid, working both as storage when lots of renewable energy is at disposal and as a power supply when energy is needed from the network. At the same time, a safe and efficient battery technology could avoid the

40 % of the European cause of pollution: the road-transport. For this purpose, secondary batteries have attained much importance. Yet, while reaching the goal of the road-transport electrification, Vehicles to Grid (V2G) can, at the same time, support the integration of renewable sources in the power supply system. Millions of li-ion batteries powering electric vehicles, would represent a huge storage capacity to the grid, allowing us to rely more safely on fluctuating renewables while quitting fossil fuel for the road-transport.

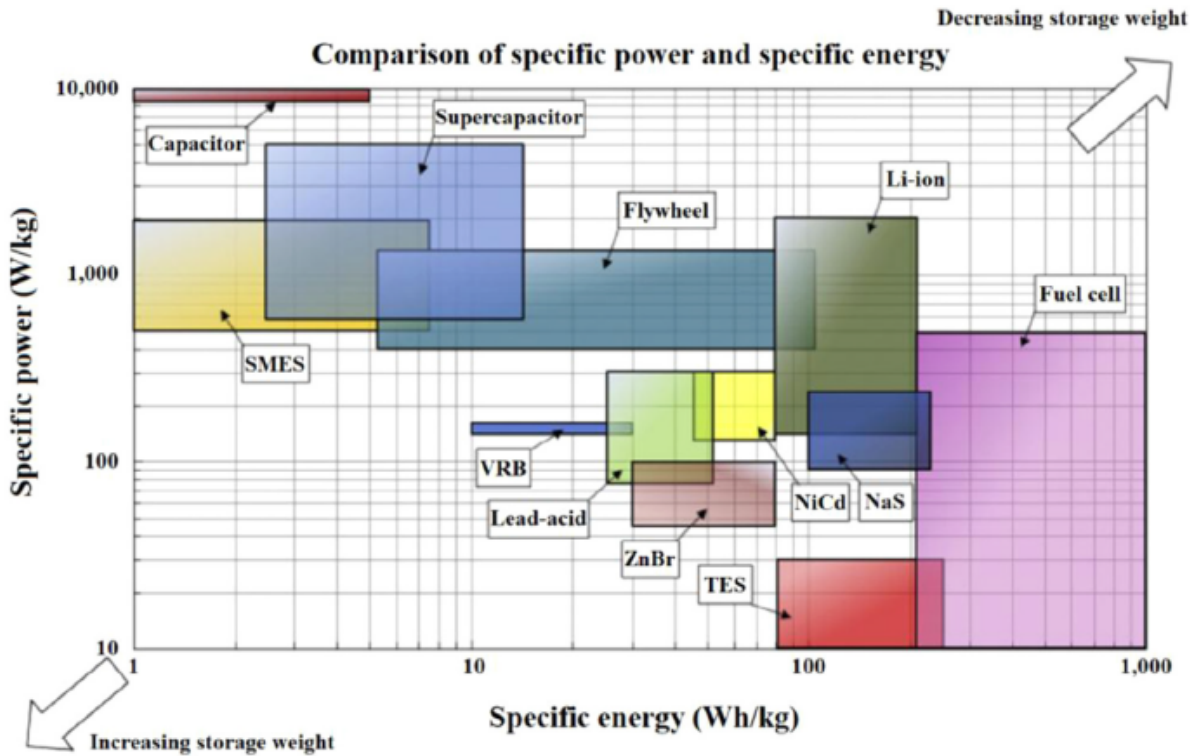


Figure 1.1: Comparison of different Electric Energy Storages based on their specific power, energy and storage weight [3]

1.1 Electrochemical storage

Among all the energy storage systems, such as mechanical, thermal and electrical, the most flexible is the electrochemical one. Decades of research in this area allowed to create different electrochemical technologies, each of them with its own performance characteristics: size, weight, energy capacity, power density, specific working conditions, full charge and discharge times, self-discharge rate, life time, cost issues and so on. Indeed, in this field, we can find the widest diversity of chemistries, which comprises, only to mention few of them, lead-acid, nickel-cadmium and nickel metal hydride, sodium-sulphur and sodium nickel chloride, lithium-ion batteries. Each one presents

some advantages as well as some drawbacks.

The invention of the battery brings back to Alessandro Volta who stacked discs of copper and zinc immersed in salty water obtaining a flow of electrons running along wires connecting the metal discs. That happened in 1800, afterwards, the human being kept investigating the electrochemical possibilities. One of the first cell of relevance was the Leclanché cell used for railroad telegraphs and electric bells, invented in 1866. The anode was metallic zinc, which has a weak ability to plating causing dendritic precipitation. This cell was the first example of non-rechargeable cell, also identified as primary battery. In 1972 Sanyo introduced on the market a primary battery consisting in metallic lithium as anode and manganese dioxide as cathode. Unfortunately, given the lithium high reactivity with liquid electrolyte, which eventually causes dendritic growth and dangerous short circuits, professional world lost interest in lithium metallic cell. The lead-acid battery was the very first rechargeable storage system in history, conceived in 1859, largely developed during nineties, it still maintains a good market share thanks to the low production costs and its mature technology. At that time, also two nickel-based battery were investigated: nickel-cadmium and nickel hydride batteries. The former takes advantage from the cadmium high specific charge ($477 \frac{Ah}{kg}$) using it as cathode, but quite soon this battery gave up its market share to the latter. Indeed, using a hydrogen-absorbing alloy as cathode, it permitted to reach energy densities comparable to the Li-ion ones. But still these nickel-based devices have too high self-discharge rates and costs higher than lead acid. Very suitable for large stationary energy storage system, are batteries with sodium as anode. One kind of battery has sulfur as cathode while a safer one has nickel chloride. Both can work up to 300 °C and their production costs decrease with size.

1.2 Lithium ion battery

During the eighties, portable electronic devices such as video cameras, notebook computers and cell phones started to become essential daily tools. As a consequence, markets claimed rechargeable battery suitable for mobile applications, that means asking for greater capacity while reducing size and weight. For this purpose, researchers started to re-evaluate the potential of lithium for the electrochemical storage. Indeed, this metal is widely available, non-toxic but above all very light and electropositive. Unfortunately, critical deposition of lithium on the negative electrode during discharging prevented for a long time the employment of lithium batteries, because of safety and efficiency reasons. Luckily, several scientists had the idea of using intercalation compounds of

lithium as anode materials, which can donate Li-ions to the cathode through a reversible chemical reaction. They also came up with a negative electrode consisting of lithium compounds combined with carbon, namely the lithium graphite (LiC_6). While the positive, as explained above, had to be a transition-metal oxide enriched with lithium ions, such as $LiCoO_2$. Such cell, completed with an electrolyte made of organic carbonates and lithium hexafluorophosphate ($LiPF_6$), represented the first produced lithium ion battery. In 1991, the commercial breakthrough of this promising electrochemical solution was reached thanks to SONY and Asahi Kasei[1].

Since then, many efforts have been devoted to the development of this particular electrochemical system, exploring different materials for cathodes, anodes and electrolytes. Thus, this commitment led to such a technological diversification that Li-ion batteries are perfectly suitable for a huge range of applications. As already said, the primary Li-ion battery market was represented mostly by portable electronic devices. Mobile phones, tablets, cordless, notebooks, cameras, MP3 players, video games kept requiring, over the years, smaller and smaller batteries characterized by higher specific energy and power. Therefore, the Li-ion cell has been the technology of choice. However, nowadays, Li-ion batteries are not only the dominant technology in portable devices market but also the most suitable for challenging emerging applications. Indeed, it found use in different fields: aerospace sector for satellites and aviation; medical area in hearing aids and implantable devices, for example aimed at drug-delivery and glucose sensing; micro-electronic branch for miniature transistors, sensors and actuators; wearable technology application such as flashlights, radio-controlled toys and solar LED systems[3]. Nevertheless, probably the most interesting market evolution is the increase of battery demand for road-transport: since 2010 to 2019 the number of electric cars existing on world's roads rose from only 17 thousand units to 7.2 million[4]. Moreover, in spite of the global electric vehicle market heavily affected by the COVID-19 pandemic, mostly in China and USA where sales dropped a little, still we are seeing growth in number of EVs all around the globe. As a matter of fact global EV market penetration increased even in the first quarter of 2020 reaching a share of 2.8 percent[5]. Taking into account that Li-ion is the technology of choice in the EV field, it makes totally sense that nowadays the largest Li-ion market share has been taken by the road-transport sector over the portable electronics. Automobile manufacturers are offering Battery Electric Vehicles (BEVs), Hybrid Electric Vehicles (HEVs) and Plug-in Hybrid Electric Vehicles (PHEVs) equipped with Li-ion solutions as a primary power source, since they offer high specific energy, charge retention capacity and low maintenance. At last but not the least, Li-ion technology can provide a big contribution toward the energy transition being integrated in

power supply systems, both off-grid and grid-connected. At least two interesting reasons make this solution even more sustainable than using other Electric Energy Storages (EES). One is the possibility to recycle the batteries whose capacity dropped to 80% of initial value, using them for the grid ancillary services. The second one is the idea of using BEVs and PHEVs as grid energy storages when they are connected to the grid, this concept is called the Vehicle to Grid (V2G) and it is intensively under study for its impressive potential.

As mentioned above, the success showed by this technology is due to the outstanding specific energy and power, high roundtrip efficiency, long calendar and cycle life, low operation and maintenance costs, acceptable self-discharge rate, good recharge time, and so forth. But beyond those, what is allowing this chemistry to be present in so many application field, is its technology diversity and performance parameter adjustability. By changing the cathode metal-oxide, specific energy can be increased from 90 up to $250 \frac{Wh}{kg}$, which makes them very suitable for portable applications; on the other side, a PHEV may require instead very high specific power, in this case the options are multiple, such as making larger but thinner cathodes and anodes in order to enhance the solid electrolyte interphase (SEI) along with the charge flow, or again, relying on a different active material which performs a better ion diffusion; still, employing a polymeric gel as electrolyte instead of a liquid one, this would erase the need of a case and in this way they can be produced in any desired shape, which is practical in case of wearable electronics. Since the choice of a certain lithium metal oxide is what mainly determines the battery characteristics, commercial Li-ion cells are named after them.

The already mentioned LCO chemistry was the first commercialized Li-ion battery, made of $LiCoO_2$ cathode and LiC_6 anode, and is maybe the most mature technology among all the Li-ions. At the beginning, a noticeable specific energy of $150-190 \frac{Wh}{kg}$ made this battery very attractive for cell phones, tablet and portable PC. Additionally, it can handle from 500 to 1000 full cycles resulting in a calendar life of few years, which is relatively modest for the meant applications.

Yet, two main reasons leave this technology out of the picture for all main battery industries. Because of the narrow cobalt-oxide thermal stability, the battery already at $150 \text{ }^\circ\text{C}$ is not working safely anymore. As a matter of fact, battery failure incidents affecting airplanes for several months



Figure 1.2: Schematic overview of LCO characteristics.

in 2013 and some safety test [6] [7], confirmed its unsuitability for consumer use. Additionally, serious environmental and ethical concerns have risen in recent years for the Li-ion reliance on cobalt. Despite its reserves are very low, the Democratic Republic of Congo is mining the soil without any interest in a more sustainable cobalt production or opportune safety standard for miners, who very usually are children [12]. Thus, since the cobalt content in LCO batteries is not negligible, other chemistries are preferable to LCO.



Figure 1.3: Schematic overview of LMO characteristics.

The LMO battery is a free-cobalt technology which uses manganese dioxide (MnO_2) usually combined with lithium graphite (LiC_6) or lithium titanate ($Li_4Ti_5O_{12}$) anodes. One of the most used oxide in LMO batteries is $LiMn_2O_4$ which belongs to the spinel family whose structure promotes the ion flow resulting in high diffusion coefficient and thus in high specific power. However, it performs a quite low specific energy ($100-140 \frac{Wh}{kg}$), resulting unsuitable for portable application. Nevertheless,

LMO batteries are inherently safer: thermal runaway can occur at approximately $250 \text{ }^\circ\text{C}$. Furthermore, the battery is cobalt-free, relies on abundant and eco-friendly materials and can last for 1500 full cycles. As a result, LMO batteries are mostly used in e-bikes and medical devices.

The lithium iron phosphate ($LiFePO_4$) batteries perform the highest durability, up to 2000 full cycles, inherent safety and reliance on abundant and eco-friendly materials. It shows tolerance if abused and behaves constantly good throughout all the SOC range (from 15% to 100%). Some interest has been shown for incorporating it into EV above all for its high specific power, but its specific energy, comprised between $90 \frac{Wh}{kg}$ and $140 \frac{Wh}{kg}$, is too low compared to other chemistries. Moreover an LFP



Figure 1.4: Schematic overview of LFP characteristics.

battery is not really affordable for middle class consumers. Still, considering the former important advantages, it is encountering a lot of success in e-bikes, while being also one of the best candidates for power supply systems storage mostly due to its long cycle life and the reliance on eco-friendly and abundant materials. Given the unavoidable need for high specific energy for portable devices, cobalt-free chemistries (LFP and LMO) can't compete in this field.

The answer to all these market and social requirements is a tradeoff between cobalt withdrawal and high specific energy: NCA and NMC chemistries.

Batteries with lithium nickel cobalt aluminium oxide ($LiNiCoAlO_2$) cathodes, usually completed with lithium graphite anodes, perform best in the specific energy aspect with a maximum value of $250 \frac{Wh}{kg}$. It also shows reasonably good specific power with a life span comparable to the one of LMO. In addition, it leans on a lower amount of cobalt compared to LCO, typically 15 mole percent, meeting way more the cobalt mining concerns. Indeed, NCA batteries have been commercially available for almost 20 years and meeting the automotive requirements of energy density, safety and stability, they are already a strong reality in automotive battery field, for example as main storage mean in Tesla EVs. Lastly, this chemistry has all the prerequisites for supporting the energy supply system.



Figure 1.5: Schematic overview of NCA (a) and NMC(b) characteristics.

Although, NCA cells have to compete with a promising and emerging technology: NMC battery. Despite its recent commercialization (2004), it is already dominating the EV and PHEV markets, while being used in portable electronics, power tools and medical devices too. Such a market share is explicable by its characteristics. Firstly, it relies on the same content of cobalt as the NCA battery. Then, since the road transport electrification has such a huge potential in reducing Greenhouse gasses (GHG) emissions, even more when paired with renewable energy sources, a lot of interest has been addressed to NMC chemistry study and development, to a point where it is already a mature technology. It is inherently safe, costs are currently lowering thanks to its market share and it performs better than NCA in durability, since it can endure for 2000 cycles. Regarding the specific power and energy, they can be varied by changing the proportion of the three components: nickel, manganese and cobalt. A higher amount of nickel enhances the specific

energy up to $200 \frac{Wh}{kg}$, while rising the proportion of manganese at the expense of specific energy, the gain is in the specific power aspect. This freedom in changing cell performances allows to produce NMC battery tailored for almost every kind of electric vehicles. For instance, a PHEV requires higher power over energy capacity, while in EV this ratio doesn't need to be so high. Both of these applications requirements can be met by the NMC technology. As evidence of this, in general the electric vehicles market is opting for NMC cell instead of NCA, because of the former longer lifetime, that for example, in a PHEV represent about two years of life extra with respect to NCA battery pack. So manufacturers are preferring more durable than lighter EV.

1.3 Lithium metal battery

Up to recent days lithium based cells were constituted by compounds capable to donate lithium ions, and practically almost all of them were graphite-anode-based batteries. Thanks to all the efforts put into Li-ion technology research over the last decades, these state of art Li-ion batteries are nearly approaching their theoretical specific energy ($350 \frac{Wh}{kg}$). Still, this won't be enough to cope with the new long-range electric vehicles requirements of high energy density. Specifically speaking, graphite anode is the limiting factor in the theoretical energy density value. Thus, alternative high capacity anodes are the answer to the cutting-edge exigent appliances. Without any doubt, the most promising anode is lithium metal, with a theoretical extra-high capacity of $3860 \frac{mAh}{g}$, the lowest negative electrochemical potential (-3.040 V vs standard hydrogen electrode) and the smallest atomic radius of all metals which explains its quick transfer nature. Applying Li metal as anode, higher Open Circuit Voltage (OCV) can be obtained being lower the delithiation potential of the anode. If coupled with a high-voltage cathode, a cell of this kind can provide high discharging voltages and so deliver outstanding energy density of about $440 \frac{Wh}{kg}$. [8] At the anode-electrolyte interface, electrons and Li-ions combine and get stored on the electrode via intercalation or deposition. The understanding of what happens at this interface is critically fundamental in order to obtain a safe working, efficient and durable battery. Despite the excellent characteristics of lithium metal, its ultrahigh negative potential and high reactivity, typical of the alkali group, result in serious instability when it encounters electrolytes. The latter are only supposed to transport Li-ions from electrode to electrode. But, in order to be actually stable in the battery, the electrolyte needs to have the lowest unoccupied molecular orbital (LUMO) higher than the Fermi energy level of the anode. As well as, its highest occupied molecular orbital (HOMO)

has to be lower than the Fermi energy of the cathode. If it isn't so, solvents, additives and salts composing the electrolyte are reduced at the anode surface resulting in active lithium consumption, electrons stolen from the collector and electrolyte decomposition. Hence, having an anode with low negative potential has the drawback of resulting in a redox potential interval of the electrodes that lies outside of the electrochemical stability window of the electrolyte. This makes lithium metal, whose redox potential is clearly the lowest (-3.04 vs SHE), unavoidably reactive with every kind of electrolyte: aqueous and nonaqueous liquid, polymer and inorganic solid. As soon as lithium metal

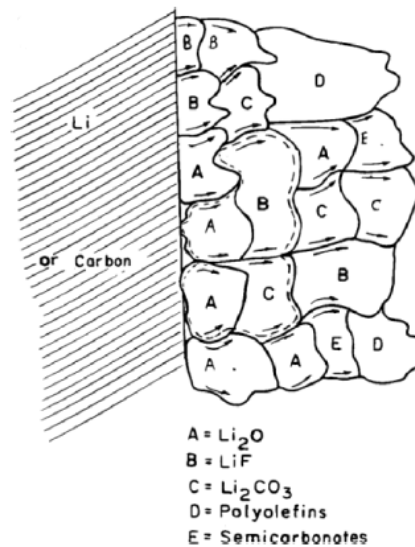


Figure 1.6: Mosaic structure of the SEI [9]

is immersed into electrolyte, many reductive decompositions of the solution components occur, and a mixture of insoluble multiphase products deposit on the negative electrode according to a so called "mosaic" structure [9]. As showed in figure 1.6. The formed passivation layer acts like a solid electrolyte and thus it is named as SEI: Solid Electrolyte Interphase. Let's say first that overall SEIs are fragile and not homogenous both on the surface and along the thickness. This heterogeneity is responsible for the SEI mechanical instability which brings, during stripping and plating cycles, to breaks and cracks. These cracked areas offer fresh lithium at disposal to react with solution, resulting in additional loss of pristine lithium and useful electrolyte. But, moreover, these cracked areas are characterized by local higher electrical fields which represent hot spots for Li-ion reduction. It is worth noticing that a vicious loop is created since more cracks means more irregularities, but more irregularities means more cracking. Reactions between Li, electrons and solution species keep occurring unless electrons or solvent start lacking, otherwise the SEI carry on growing in thickness. The nature of the SEI, its composition, structure, thickness, and mechanical

properties depends on the chosen electrolyte, because parasitic reactions are more likely or not to happen, and will generate certain organic and inorganic composites depending on the salts and solvents involved in the reactions. So SEI properties, such as electron tunneling, Li-ion conductivity, chemical and mechanical stability both at the Li metal anode face and the electrolyte one, will differ depending on the electrolyte. This is to be kept in mind, knowing that SEI formation is unavoidable but also necessary for the proper working of the anode: an homogeneous, smooth, thin, flexible and compact SEI can protect the anode for several reasons. It would block electrons leakage from the anode and cover pristine lithium, avoiding thus further side reactions, so that the Coulombic Efficiency and cycle life of the Li anode is greatly improved. Moreover, the passivation made by the SEI can extend the voltage window tolerable by the electrolyte up to 4 Volt or more [8]. It may even enhance Li ion diffusion, obtaining also a homogenous transport of cations. But, most of all, a smooth SEI surface can abolish undesirable electric field at the film protrusions which are responsible for inhomogeneous deposition of reduced Li-ion on the anode. The latter is a vital issue to consider, since it leads to lithium dendrite growth and its related problems that prevented for a long time the Li-metal technology to be exploited up to nowadays. Contrary to lithium compound anode which can be defined as insertion hosting electrode, Li metal anode is a conversion hostless electrode, which means that ions are reduced and deposited directly on the anode surface. Hence, a Li metal cell with a non ideal SEI is characterized by unstable Li deposition and thus dendrite growth. Severe and dangerous chain-linked consequences are exposed hereafter:

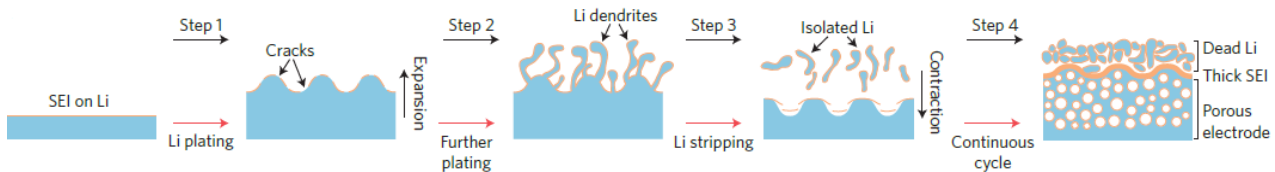


Figure 1.7: Formation and growth of lithium dendrites [8]

- Step 1: accounting for the conversion-pattern, not supplied with a matrix hosting reduced lithium ions, during plating process the volume change of the lithium domain below the SEI film, is virtually infinite. And this uncontrolled expansion can break the fragile SEI, creating cracks and protrusions.
- Step 2: as plating keeps going, Li-ions are more likely to reduce over the protrusion tips,

where the local electric fields tend to attract them, making dendrites grow. Eventually this uncontrolled deposition can lead the Li-needles to penetrate the separator down to the cathode, causing a consequent cell short circuit. The latter brings us to the main concerns about using this technology: thermal runaway, electrolyte combustion and cell explosion. Moreover, longer dendrites represent higher lithium surface in contact with the electrolyte and thus further parasitic reactions.

- Step 3: the following stripping phase remove Li from the main volume contracting it, but also from the dendrite roots, causing their detachment from the anode. These small pieces wrapped instantaneously by a SEI film are insulated and inert, thus they are named as "Dead Li". Such a waste of electrolyte and lithium active material decreases further more the Coulombic Efficiency.
- Step 4: series of plating and stripping processes and thus of the aforementioned steps, eventually create a layered electrode constituted from the top by a slab of Dead Li, a heterogeneous and very thick SEI, and finally on the bottom a porous electrode. This composition forces Li-ions and electrons to diffuse through very long and intricate pathways among dead Li and pores, which result in a very high diffusion resistance. Furthermore, liquid electrolyte can easily flow into pores and allow again side reactions.[8]

The reviving of lithium metal cell has conducted to a lot of new strategies to protect the metal anode for a long-term, stable, safe and efficient battery. The first shoot was given to the non-aqueous liquid electrolyte: intensified attention have been devoted in seeking the optimal salts, solvents and additives since they determine the physico-chemical morphology of the SEI. Some electrolyte additives were designed to promote the formation of a stable SEI, side reaction preventing, mechanically performing to suppress dendrite growth, ion conducting and electronically insulative. Their working principle consists in extending the window stability of the electrolyte, that means having higher HOMO and lower LUMO, in order to react before the other electrolyte component and creating a protecting SEI. Giving an example, adding cesium hexafluorophosphate (CsPF_5) to the electrolyte consisting of 1.0 M LiPF_6 in propylene carbonate, the SEI starts emerging already at 2.05 V vs Li/Li+, before the Li deposition begins, allowing the formation upon the SEI of a lithium layer highly compact and well-aligned nanorods. Yet, these kind of electrolyte usually have a Coulombic Efficiency of 99.8 % which equals to 0.2 % of Li lost per cycle. Solid-state electrolyte can overcome the flammability of liquid electrolyte, their easy penetration into anode

pores, and reduce the lithium losses. But, the aim of this solution is mainly to have a high shear modulus that can suppress the dendrite propagation. Two principal categories constitute the solid electrolyte: inorganic ceramic electrolyte and solid polymer electrolyte. The former exhibits ion conductivity comparable with the liquid ones, and a very high elastic modulus. But higher is the modulus lower is the surface adhesion with the electrodes resulting in high interfacial resistance. Moreover, side reactions are not totally avoided since their electrochemical stability window is quite narrow. On the other side solid polymer electrolyte shows satisfying adhesion and good stability but low mechanical properties and ion conductivity.[11] These two lasts can be improved easily and continuous efforts are being invested on this purpose. Even artificial protective SEI layer, constructed *ex situ* to coat the Li-metal anode, are under investigation.

Li-metal batteries are the promise for the next generation high energy density technologies, needed for the urgent energy transition of our century. Research is working to make it possible, and results are anything but disappointing.

1.4 Steps of this work

The work reported herein is motivated to contributing towards the development of safe and high performing Li-metal batteries. This thesis is devoted to providing some instruments to reach this goal. The first one, which is exposed in the first half of the document, is a thermo-electrochemical model for high energy density and high voltage Li-metal battery. They are composed by a commercial NMC622 cathode, lithium metal anode, separator Celgard 2500 and EC:DEC LiPF₆ 1M electrolyte. Modelling the operation of a particular cell is useful to better design the latter, in order to avoid its capacity fading, fast aging and above all dangerous thermal runaways. The chosen model, the Pseudo-two-Dimensional (P2D), based on electrochemical kinetic and transport equation and on the coupling of particle radius domain and cell thickness domain, is implemented on the finite element package Comsol Multiphysics 5.5. The model is constructed on Fick's and Ohm's law, the energy and mass conservation equations and the Butler-Volmer equation. Crucial is to know the thermal behaviour of a certain cell to prevent any dangerous situation. Thus, a 3D thermal model is coupled to the electrochemical, by the heat generation (computed by P2D) and the mean volume temperature (calculated by the thermal model). In order to run a close simulation, physical, chemical and kinetic properties have been experimentally evaluated or found in literature. Conducting test in the laboratory, NMC622 has been fully parametrized: geometric length have

been measured, particle radius has been averaged by FESEM images, a GITT test gave the diffusion coefficient, a slow galvanostatic experiment allowed to plot the equilibrium potential, by galvanostatic cycling, electrode volume fraction has been computed, though EIS measurements and impedance curve fitting, electrode initial current density has been derived and, lastly, by means of DSC measurements NMC622 heat capacity has been obtained. When it wasn't possible to perform on-hand tests or in cases of widely studied materials as lithium, Celgard and EC:DEC LiPF_6 , parameters have been searched in literature, including, all the previous parameters for the anode, separator and electrolyte, the NMC622 entropy factor, transference number, density, thermal conductivity and others more. Finally, comparing electrochemical and thermal simulation results with experimental data, the proposed model has been validated. The second part of the thesis is focused on the lithium protection. To reach this goal, a polymeric electrolyte has been proposed, synthesized and characterized. Polymer have been recently recognised as a promising material for electrolyte, able to enhance enormously battery performance, protecting and preserving its material, as well as, avoiding lithium dendrite growth. A (butyl methacrylate)/poly(ethylene glycol)diacrylate (BMA-co-PEGDA) membrane in which different amount of inorganic zirconia nanoparticles were embedded, and further swollen with ethylene carbonate and diethyl carbonate (EC:DEC) 1:1 LiPF_6 , is the Composite Gel Polymeric Electrolyte (CGPE), that have been prepared in an Argon atmosphere to permit the thermo-initiated radical polymerization. Then, the membranes have been physical characterized by TGA, FTIR, FESEM and XRD. TGA results provided information about thermal stability of precursors and as-prepared membranes; FTIR spectra confirmed the achievement of complete polymerization, which creates a fine polymeric network with preferential pathways for Li-ions; FESEM images proved that polymer are so manageable to agglomerate high content of ZrO_2 , maintaining flexibility and rigidity; XRD spectra proved the disappearance of crystalline phase in the polymer, due to the encompassing of zirconia nanoparticles. To follow, the electrochemical characterization has been accomplished to attest polymer benefits. As a result of polymers, being amorphous, and the addition of ceramic, having erased the crystalline phase, the segment movements are faster and so the ion conductivity, obtained by EIS measurements, increased by almost 3 order of magnitude with respect to Celgard. In particular, membrane with 63 % wt of zirconia, showed the best value, and thus, only that one has been further characterized. Through LSV, CGPE stability window has been assessed satisfying wide. A chronoamperometry test, followed by EIS spectra, validated the hypothesis that creating preferential pathways with reticulated polymers, embedding ceramic nanoparticles, increases the transference number of the

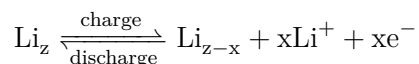
electrolyte. And in closing, galvanostatic cycling combined with EIS measurements demonstrated, through a symmetric cell equipped with the CGPE able to cycle for over 100 cycles, that dendritic growth has been suppressed.

Chapter 2

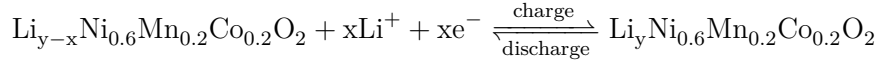
Modelling

A useful tool in the effort to scale up Li-ion technology, making it even safer and more efficient, is the battery modelling. As a matter of fact, electrochemical models are largely implemented in the automotive application in order to fully understand battery behaviour under extreme operating conditions, such as, high transient loads and temperature rise, and, thus, overcome problems with a fine-tuned solution. The thermal-electrochemical model of this work simulates the discharge at constant current rate of a Li-metal|EC:DEC| $Ni_{0.6}Mn_{0.2}Co_{0.2}O_2$ cell. Mathematical modelling always starts with a schematic representation of the basic unit: the cell. The Figure 2.1 depicts the scheme of sandwich-structured cell representative of this work, consisting of two electrodes, one current collector and a separator, emerged in a liquid electrolyte. A Li-foil is serving as current collector and negative electrode where the oxidation takes place. Here, during the discharge process, as the consequence of the oxidation reaction, electrons travel towards the electric circuit while lithium ions diffuse in the opposite direction until they arrive at the interface with electrolyte reacting with it. Those products diffuse through the polymeric separator, namely a Celgard2500, which insulates electronically the two electrodes preventing short circuits while conducting ion-electrolyte products to the positive electrode. The latter is the above mentioned lithium insertion compounds $Ni_{0.6}Mn_{0.2}Co_{0.2}O_2$ whose conductive lattice receives electrons arriving from the external circuit and Li-ions which are here reduced and intercalated. The opposite process occurs in case of battery charging. The chemical reactions taking place in the cell are the following:

Negative electrode reaction



Positive electrode reaction



A porous morphology has been developed for the positive electrode in order to gain more active solid-electrolyte interface area since the liquid pervades the solid matrix. The latter as shown in 2.1 can be seen as an ensemble of spherical particles of radius r_p in which Li-ions diffuse and react over their surfaces.

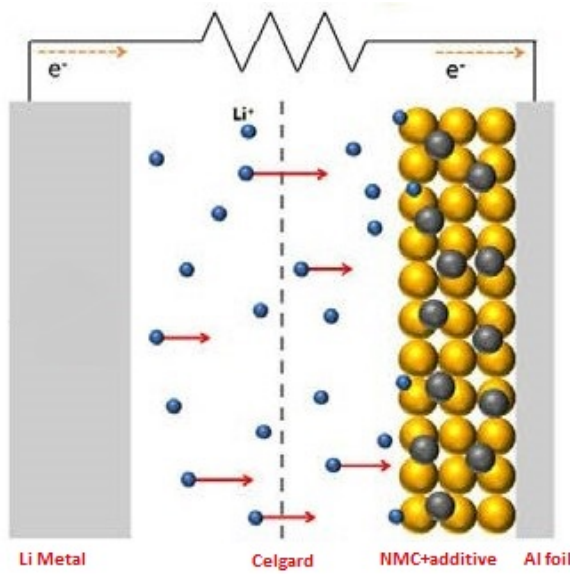


Figure 2.1: Schematic representation of a liquid organic electrolyte Li-metal cell [17]

For the sake of battery modelling, the next step is to define the dependent variables of interest, their governing equations, the related initial values and boundary conditions. Depending on the application to which the simulation is devoted, a method of solution of the obtained electrochemical system has to be selected among the others. The following step is not a simple task, but it is necessary to make the simulation run. It is to measure, searching on literature or estimate physical, chemical and kinetic properties and parameter to be implemented in the model. The more accurate is the parametrization, the more reliable is the model. Finally, the last step is to validate the model, by verifying whether the obtained parameter set are consistent with experimental data or not. Following this working chain, the variables investigated in the model are the following: solid-state Li-ion concentration c_s [$\frac{\text{mol}}{\text{m}^3}$]; liquid-phase Li-ion concentration c_l [$\frac{\text{mol}}{\text{m}^3}$]; solid-state potentials in

the electrodes ϕ_s [V]; liquid-phase potential in the electrolyte ϕ_l [V]; internal battery average temperature T [K]. Generally speaking, the choice of the mathematical model depends on what it is meant for. Simulating cell behaviour under special operating condition, or being used in the Battery Management System (BMS), rather than predicting the battery performance and State Of Health (SOH) after a cycling or calendar aging. The multitude of models can be divided in two main family: empirical models and electrochemical models. The former, again, can be categorized in two: fully empirical model such as the artificial neural networks and the semi-empirical model like the equivalent circuit models. These examples provide empirical extrapolation from experimental data of a cell working under certain conditions. So, it is only available for this specific studied case, in these constant working condition, giving as output result the SOC and the SOH. As understandable, it can not be transposed to another cell, but neither be updated with battery characteristics as it ages. Yet, this family of models is widely used for BMS since they are computational fast and simple to implement. [15]. Predictions much more accurate and rigorous are obtained by implementation of models based on electrochemical kinetics and transport equations. They are efficiently applicable for parameter estimation and age investigation since they can be updated as the battery ages. Additionally, they are valid for different kind of batteries, materials and geometries, and also they can closely simulate extreme working conditions like high charge and discharge rate. Among them, two are the most used: the Pseudo-Two-Dimensional (P2D) model and the Single Particle Model (SPM). The former applies electrochemical and kinetic reactions along two 1D domains: the cell thickness and the electrode particles radii. These two realms are connected and they affect each other. The second one, the SPM, can be considered as the simplification of the primer. It ignores the electrolyte properties and models the electrodes as two single particles. This model is not able to simulate high rated working conditions, but is computationally less demanding and provides fast response, ideal for BMS and online control. For the sake of exhaustiveness, here the last group of models, the simplified methods, are mentioned. Very easy to be implemented and low computational effort needing, they are the simplified version of P2D and SPM. For example one of them assumes the time-dependent variables to have polynomial profiles. Purposely designed for BMS and online monitoring.[18] The figure 2.2 proposes a simple summarizing diagram.

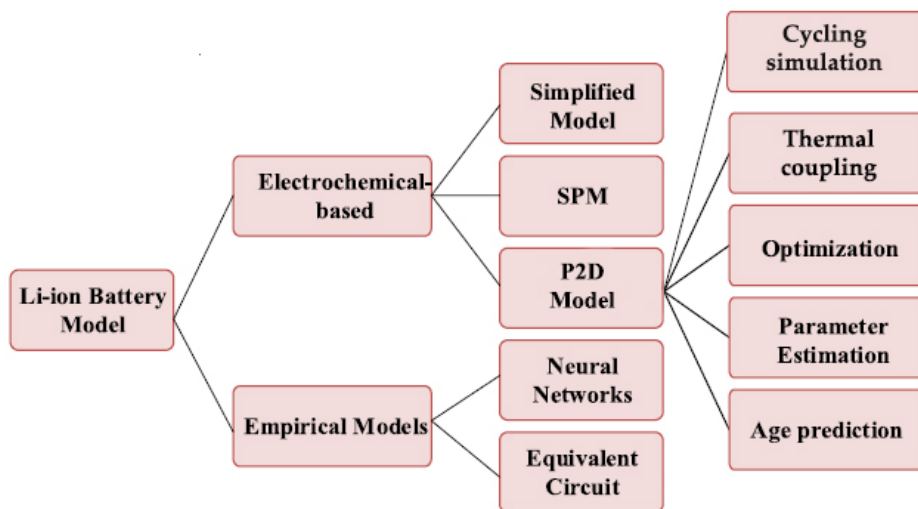


Figure 2.2: General classification of Li-ion models [18]

2.1 The electrochemical model

As already mentioned above, the aim of this work is to develop a high energy density battery, assuring, at the same time, safe working. In order to prevent short circuits and thermal runways, accurate simulation and reliable parameters are needed to perfectly design this kind of battery. In the light of that, the pseudo-two-dimension model has been chosen. The strength of this model derives from the coupling of macro and microscale descriptions of kinetic and diffusion phenomena occurring in the cell. The microscopic field deals with the lithium diffusion at the solid active material and electrolyte interface in the electrode. Here, the concentration of lithium varies along the radius (r_p) of spherical particles which model the porous electrode, as shown in 2.3. At the same time, charges and species transport in solid and liquid phases of both electrodes and electrolyte are described in a macroscopic way. Li-ion concentrations, c_s and c_l , as well as, electrochemical potentials, ϕ_s and ϕ_s , depend on the spatial coordinate x running along the cell thickness. This two 1D domains are connected and inter-dependent through the several governing equation forming the model.

Reactions of oxidation and reduction occurring at the electrode release electrons and ions which

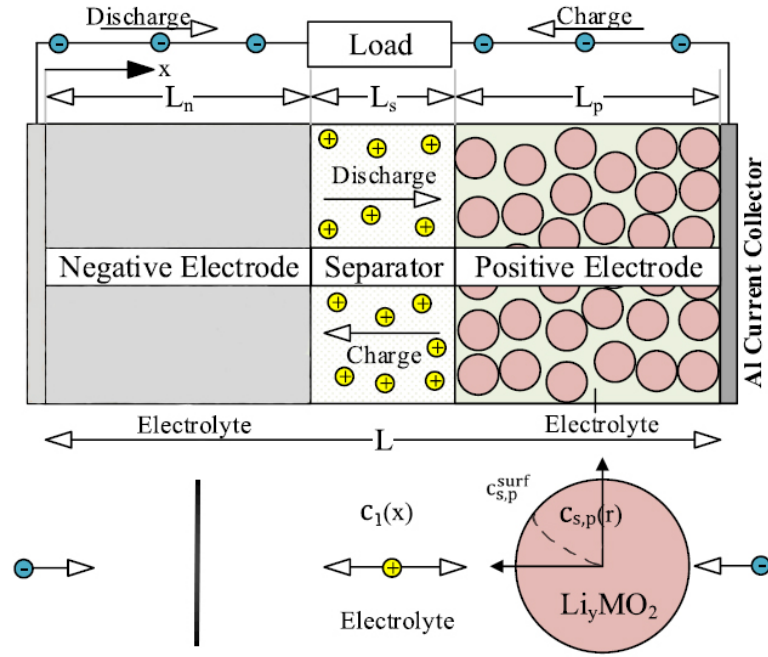


Figure 2.3: Li-metal battery P2D model scheme. Modified figure from [18]

diffuse. Electrons conduction in the solid phase is described by the Ohm's law:

$$i_s = -\sigma_{s,eff} \nabla \phi_s \quad (2.1)$$

$$\sigma_{s,eff} = \epsilon_s^{1.5} \sigma_s \quad (2.2)$$

where

- i_s is the solid current density [$\frac{A}{cm^2}$]
- $\sigma_{s,eff}$ is the effective electrical conductivity of solid state active material [$\frac{1}{\Omega cm}$]
- σ_s is the electrical conductivity of solid state active material [$\frac{1}{\Omega cm}$]
- ϵ_s is solid phase volume fraction

At the same time, in the electrolyte, flowing ions determine the presence of a current, which is obtained by the concentrated solution theory:

$$i_l = \underbrace{-\sigma_{l,eff} \nabla \phi_l}_{\text{migration phenomenon}} + \underbrace{\frac{2RT\sigma_{l,eff}}{F} (1-t_+) \left(1 + \frac{\partial \ln f}{\partial \ln c_l}\right) \nabla \ln c_l}_{\text{diffusion phenomenon}} \quad (2.3)$$

$$\sigma_{l,eff} = \epsilon_l^{1.5} \sigma_l \quad (2.4)$$

where

- i_l is the electrolyte current density [$\frac{A}{cm^2}$]
- $\sigma_{l,eff}$ is the effective ionic conductivity of electrolyte phase [$\frac{S}{m}$]
- R is the gas constant equal to 8.314 [$\frac{J}{Kmol}$]
- T is the temperature [K]
- F is the Faraday constant equal to 96 485 [$\frac{C}{mol}$]
- t_+ is the transference number
- f is the mean molar activity
- $\frac{\partial \ln f}{\partial \ln c_l}$ is the activity dependence
- σ_s is the electrical conductivity of solid state active material [$\frac{1}{\Omega cm}$]
- ϵ_s is solid phase volume fraction

The mass Li-ion flux is based on three transport phenomena: migration, which is ascribed to an electric potential; diffusion, which is driven by a concentration gradient; and convection, related to a pressure difference, which is negligible in lithium-ion batteries. [21] The charge conservation law applies second order partial differential equations (PDEs) to the electrons and Li-ion. Their solutions provide the potential distribution and current conservation along the cell thickness[20].

$$\begin{cases} \nabla i_s = J_{Li,s} \\ \nabla i_l = -J_{Li,l} \end{cases}$$

$J_{Li,s}$ and $J_{Li,l}$ are the current density fluxes of charges in solid and liquid phases [$\frac{A}{cm^3}$]. Boundaries conditions for the conservation laws are 2.5 and 2.6 for the solid active material and 2.7 for the electrolyte:

$$-\sigma_{s,eff} \frac{\partial \phi_s}{\partial x} \Big|_{x=0} = -\sigma_{s,eff} \frac{\partial \phi_s}{\partial x} \Big|_{x=L} = i_{app} \quad (2.5)$$

$$-\sigma_{s,eff} \frac{\partial \phi_s}{\partial x} \Big|_{x=L_n} = \sigma_{s,eff} \frac{\partial \phi_s}{\partial x} \Big|_{x=L_p} = 0 \quad (2.6)$$

$$\frac{\partial \phi_l}{\partial x} \Big|_{x=0} = \frac{\partial \phi_l}{\partial x} \Big|_{x=L} = 0 \quad (2.7)$$

Along the cell thickness, given that anode, electrolyte and cathode are connected, is imposed the continuity condition for concentration, potential, molar flux and current[14].

$$-J_{Li} = \frac{di_s}{dx} \quad (2.8)$$

$$J_{Li} = \frac{di_l}{dx} \quad (2.9)$$

$$\frac{di_l}{dx} = -\frac{di_s}{dx} \quad (2.10)$$

The sum ($i_s + i_l$) has to be constant for every x coordinate.

Focusing now on the radial domain, kinetic of insertion and extraction of Li-ion at the interface between solid and liquid phase in the electrodes, is expressed by the means of the Butler-Volmer equation. It actually defines the rate of diffusion reaction taking place at the active solid material-electrolyte interface. The reactions are assumed to be symmetric [13]. In the electrode phase:

$$J_{Li,s} = a_v i_0 \left[\exp\left(\frac{\alpha_a F \eta}{RT}\right) - \exp\left(\frac{-\alpha_c F \eta}{RT}\right) \right] \quad (2.11)$$

In the electrolyte phase:

$$J_{Li,s} = -a_v i_0 \left[\exp\left(\frac{\alpha_a F \eta}{RT}\right) - \exp\left(\frac{-\alpha_c F \eta}{RT}\right) \right] \quad (2.12)$$

where

- a_v is the active specific surface area [$\frac{1}{m}$]
- i_0 is the exchange current density [$\frac{A}{m^2}$]
- α_a is the dimensionless anodic transfer coefficient
- α_c is the dimensionless cathodic transfer coefficient

- η is the surface over-potential [V]

The dimensionless coefficient α_c and α_a determine the direction of the net reaction occurring in the cell, that's the ion flux direction and so the exchange current direction. Hence, these two are tightly interdependent since $\alpha_c = 1 - \alpha_a$. The specific area of the interface between solid particle and electrolyte is made explicit:

$$a_v = \frac{(3\epsilon_s)}{r_p} \quad (2.13)$$

where

- ϵ_s is the volume fraction of the solid active material
- r_p is the spherical particle radius [m]

The over-potential η can be defined as the actual potential difference needed to the kinetic reaction to take place compared with the lower thermodynamically expected value. Hence, is defined as follows:

$$\eta = \phi_s - \phi_l - E_{eq} \quad (2.14)$$

The equilibrium potential E_{eq} [V] of the electrode material refers to the condition of the equilibrium state of the lithium-ion battery where concentration of lithium ions within the solid and the liquid becomes uniformly distributed: so, when no potential is applied.[17] The exchange current density i_0 is defined as:

$$i_0 = F k_a^{\alpha_a} k_c^{\alpha_c} (c_{s,max} - c_s)^{\alpha_a} c_s^{\alpha_c} \left(\frac{c_l}{c_{l,ref}} \right)^{\alpha_a} \quad (2.15)$$

where

- k_a is the anodic rate constant of the electrochemical reaction [$\frac{m}{s}$]
- k_c is the cathodic rate constant of the electrochemical reaction [$\frac{m}{s}$]
- $c_{s,max}$ is the maximum concentration of lithium in the solid phase [$\frac{mol}{m^3}$]
- $c_{l,ref}$ is the reference concentration of lithium in the solution [$\frac{mol}{m^3}$]

The exchange current density is a value that expresses the rate of electrons migration as a result of the ions transport between the electrolyte and the electrode. It is the current measured at null over-potential. Thus, it depends on the applied potential through the anodic and cathodic

coefficients, and on the lithium concentration at the solid phase and empty lattice sites through the group $(c_{s,max} - c_s)$. When the concentration of lithium in the solid phase is at its maximum or minimum the exchange current is null. While, it reaches its maximum when $c_s = c_{s,max}/2$. [17]

The mass conservation law is the other governing equation of the system and it applies second order partial differential equations (PDEs) in the spherical domain and in the electrolyte phase.

$$\begin{cases} \frac{\partial c_s}{\partial t} = \nabla(-D_{s,eff}\nabla c_s) \\ \epsilon_l \frac{\partial c_l}{\partial t} = \nabla(D_{l,eff}\nabla c_l) - \nabla\left(\frac{i_{t\pm}}{F}\right) + \frac{\nabla i_l}{F} \end{cases}$$

where $D_{s,eff} [\frac{m^2}{s}]$ is effective solid phase ion diffusion coefficient of the electrode particles, while $D_{l,eff} [\frac{m^2}{s}]$ is the effective electrolyte ion diffusion coefficient.

$$D_{s,eff} = \epsilon_s^{1.5} D_s \quad (2.16)$$

$$D_{l,eff} = \epsilon_l^{1.5} D_l \quad (2.17)$$

where

- D_s is the intercalation diffusivity of the solid active phase $[\frac{m^2}{s}]$
- D_l is the diffusion coefficient of the electrolyte material $[\frac{m^2}{s}]$

All the effective diffusion and conduction coefficient have been corrected by elevating the volume fractions to the power of 1.5, which is the value assumed for the Bruggeman coefficient. This adjustment is done in order to take into account the negative effect of high tortuosity in the porous electrode on energy and power densities. [46] Also, it has to be kept in mind that $\nabla i = J_{Li}$. The boundary conditions of the mass conservation laws permit to close the connection between the two 1D domains.

$$\frac{\partial c_l}{\partial x} \Big|_{x=0} = \frac{\partial c_l}{\partial x} \Big|_{x=L} = 0 \quad (2.18)$$

$$\frac{\partial c_s}{\partial r} \Big|_{r=0} = 0 \quad (2.19)$$

$$-D_{s,eff} \frac{\partial c_s}{\partial r} \Big|_{r=r_p} = -\frac{J_{Li}}{a_v F} \quad (2.20)$$

The last boundary condition connects, through the Butler-Volmer, the equations of the radial

coordinate with the charge balance along the thickness dimension. The negative electrode, the lithium metal anode, is modelled as an electrode surface since it is a foil and no diffusion, neither particle intercalation occurs into it. Instead, here Li-ions deposition and stripping on its surface take place. So, the porous electrode theory and the two 1D domains coupling is not used. Finally, in this model other two boundaries are needed: the negative electrode is set at 0 Volt electric potential, while at the positive electrode current collector is applied the discharge current. Initial values are the electrolyte concentration and the differential potential equal to the E_{eq} of the positive porous electrode. The discharge is stopped at 3 Volt through a stop condition.

2.2 The thermal coupling

In the literature is widely accepted the fact that the operating temperature plays a key role in the aging phenomenon and in the overall cell performance[22],[23]. High temperatures are responsible for both enhanced electrochemical parameters but also accelerated degradation of the cell. Thus, in order to accurately design a safe and durable cell and optimize its operating conditions, heat generation and thermal variables have to be considered. In fact, another commendable feature of the electrochemical based models, especially the P2D model, is the fact they can be easily coupled with the thermal analysis. Guo et al. [24] presented a thermo-P2D model where heat equations connect the two systems. Numerical prediction shown satisfying accordance with the experimental data. In the light of the latter, this kind of model has been implemented in this work.

In the current report, the temperature dependence of the thermodynamic and kinetic variables have been considered, which include electrode equilibrium potentials, thermodynamic factor and reaction rate constants, as well as, physical properties related with transport phenomena, namely the diffusion coefficients. During charge and discharge cycles, some heat sources and sinks are generated because of electrochemical kinetics and transport phenomena. Firstly, since the battery is not an ideal working system, some irreversibilities occur generating irreversible heat. This is proportional to the over-potential caused by ohmic resistance, plus the activation and diffusion polarization.

$$Q_{irr} = (\nabla i_l)\eta + i_l \nabla \phi_l + i_s \nabla \phi_s \quad (2.21)$$

Beside the irreversible heat, another one is generated by the reversible electrochemical reactions taking place in both directions and behaving as both source and sink, depending on the direction

of the reaction.

$$Q_r = (\nabla_{i_l})T \frac{dE_{eq}}{dT} \quad (2.22)$$

The total generated heat is

$$Q_{tot} = Q_r + Q_{irr} \quad (2.23)$$

In the thermal model the cell is treated as a 3D geometry, but considering only the internal active material, allowing the further implementation, in a second time, for different external cell geometry. This 3D geometry, thus, consists of very thin cylinders piled up (see figure 2.4). From the bottom, it consists in a lithium-metal anode, Celgard separator, NMC622 cathode and aluminium current collector. This geometry has been meshed with tetrahedral elements, whose shape better refines uniformly rounded geometries, with a maximum element size of $8 * 10^{-4}$ [m].2.4

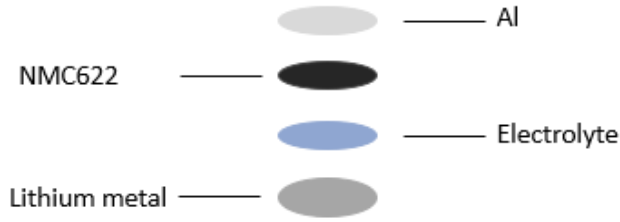


Figure 2.4: Scheme of the inner part of any kind of cell

Thanks to well meshed surfaces, heat transfer equations are computed in the model.

$$\rho C_p \frac{\partial T}{\partial t} = Q_{tot} + \underbrace{\nabla(k_T \nabla T)}_{\text{conduction}} - \underbrace{\nabla(h(T - T_a))}_{\text{convection}} - \underbrace{\nabla(\sigma_T e_T (T^4 - T_a^4))}_{\text{radiation}} \quad (2.24)$$

where

- ρ is the density [$\frac{kg}{m^3}$]
- C_p is the specific heat capacity at constant pressure [$\frac{J}{kgK}$]
- k_T is the thermal conductivity [$\frac{W}{mK}$]
- σ_T is the Stefan Boltzman constant equal to $5.67 * 10^{-8}$ [$\frac{W}{m^2K^4}$]
- e_T is the emissivity

- T_a is the ambient temperature [K]

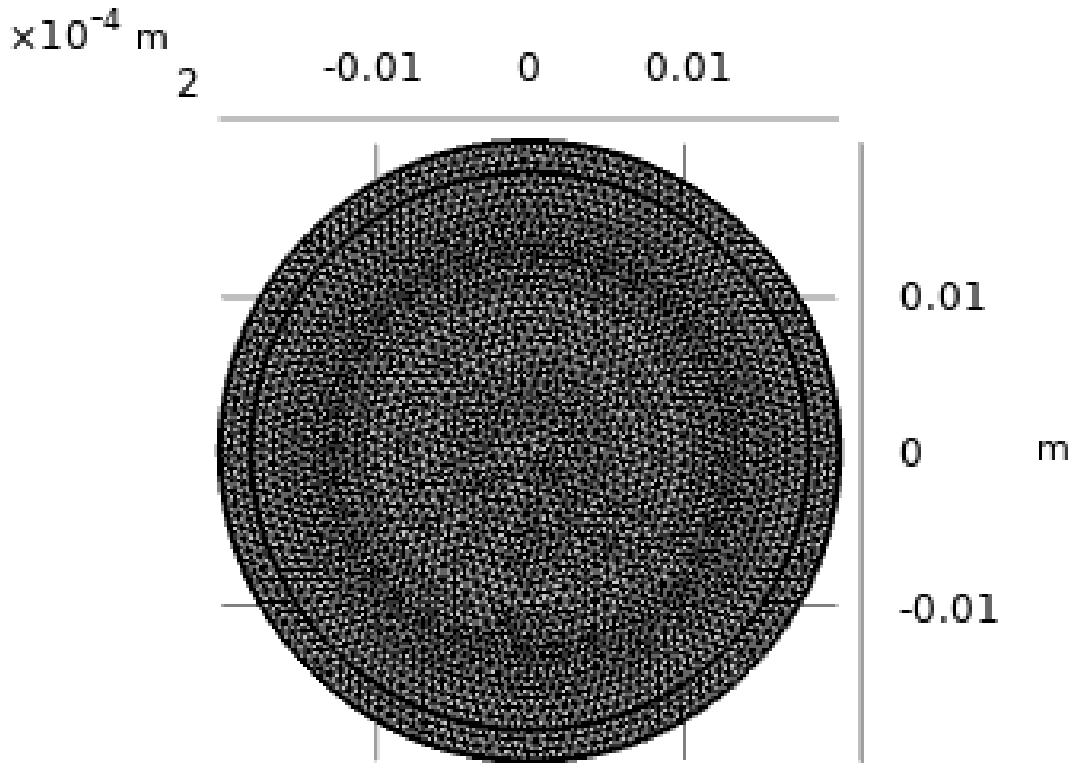


Figure 2.5: xz view of meshed coin cell

The thermal-electrochemical model was implemented in finite element package COMSOL Multiphysics 5.5. The finite element method (FEM) ensure accuracy even in modelling systems with irregular geometries, unusual boundary conditions and heterogeneous material compositions. [16] The last step but not the least important, which is outlined in the following chapter, is the parametrization of the cell. Good measures, dedicated researches and close estimates of cell and material properties are crucial for satisfying simulations. The more accurate are the transport and kinetic parameters and physical properties, the more successful is the model.

2.3 Model parameters

2.3.1 Geometric parameters

First step, in order to model the 1D and 3D geometry and properly discretize it, is to collect some geometric parameters. By the means of a digital thickness gauge and of a solvent to wet the NMC foil in order to scratch NMC layers from the aluminium one, all the thickness of interest have been

measured. The value for the lithium anode was provided by the manufacturer. The radius of the circumference are the ones implemented in the coin cells.

Table 2.1: Geometric parameters

Material	thickness (mm)	diameter (mm)
Al	0.018	15
NMC	0.06	15
Celgard	0.025	18
Lithium	0.03	18

2.3.2 Particle radius

The particle radius is required for the modelling of the radial domain, but also for the evaluation of the active specific surface area of the electrode. In order to derive this quantity, different measures of the NMC particle diameters, visible on the FESEM pictures of the foil cross-section, have been evaluated. From the FESEM image (figure 2.6) can be noticed that the morphology is quite heterogeneous, and almost no where can be noticed a repeating pattern. Indeed, for the radius estimation an average radius has been computed, considering that smaller particles prevail in number on the bigger ones. The weighted mean is equal to $6.9 \mu\text{m}$. In figure 2.6 some radii have been highlighted to give an idea of values dispersion.

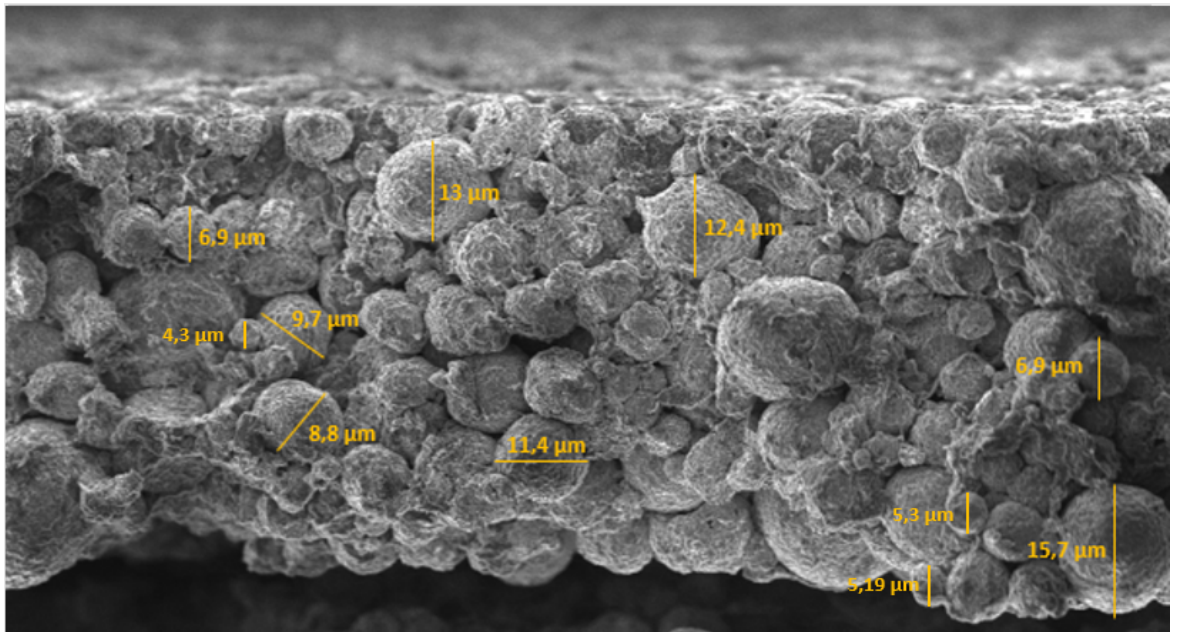


Figure 2.6: FESEM picture of NMC622

2.3.3 Cell assembly

In this work, in order to obtain electrochemical parameters to be implemented in the model, commercial cells, model ECC-Std, manufactured by EL-CELL [53], have been assembled and tested. Their schematic structure and assembly, as well as a picture of their appearance when ready to be tested, are depicted in figure 2.7. Inside the Cell Base, components of the unit battery

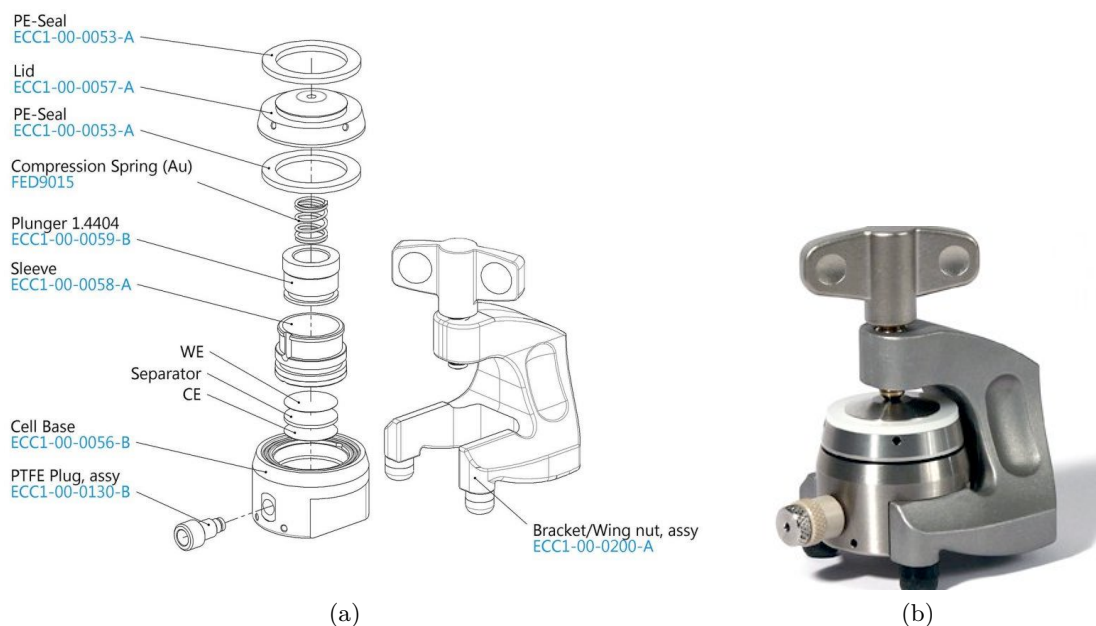


Figure 2.7: Schematic assembly of a El-Cell, which is used from now in experimental parametrization and electrochemical characterization

are enclosed in laminate film, as explained previously: from the bottom are found lithium foil, commercial monolayer separator of polypropylene Celgard 2500, liquid electrolyte EC:DEC 1:1 LiPF_6 1M, NMC622 cathode and aluminium current collector. A cylindrical Sleeve contains the latter to prevent the loss of components concentricity. Later, plunger made of stainless steel, is inserted into the sleeve vain, to press the component pile. For the similar purpose, a gold compression spring, once it is closed on the top with the lid, keeps the pressure between components in order to avoid any gas bubbles and ensuring the electrolyte permeation in the cathode pores. All these items are held together by the bracket. In addition, the cell is assembled in argon atmosphere, inside a chamber called glovebox (figure 3.8), this caution is needed because of the high reactivity of lithium with oxygen. In fact, a sealing ring is also inserted between the lid and the cell base in order to make the cell gas-tight. The as-assembled cell is displayed in figure (b) of 2.7.

2.3.4 Diffusion coefficient

A galvanostatic intermittent titration technique (GITT) has been performed in order to investigate the chemical diffusion coefficient of the lithium-ions through the NMC622 cathode. The GITT procedure consists of a series of current pulses, each followed by a relaxation time.[25] Firstly an EL-cell, composed by lithium as anode, NMC622 porous electrode as cathode, commercial separator Celgard and EC:DEC 1M 1:1 LiPF_6 electrolyte, was assembled and then charged and discharged 3 times at $C/10$ current rate between 3 and 4.4 V, in order to activate it first. Then it was fully charged again at $C/10$ and so the GITT was started. [26]

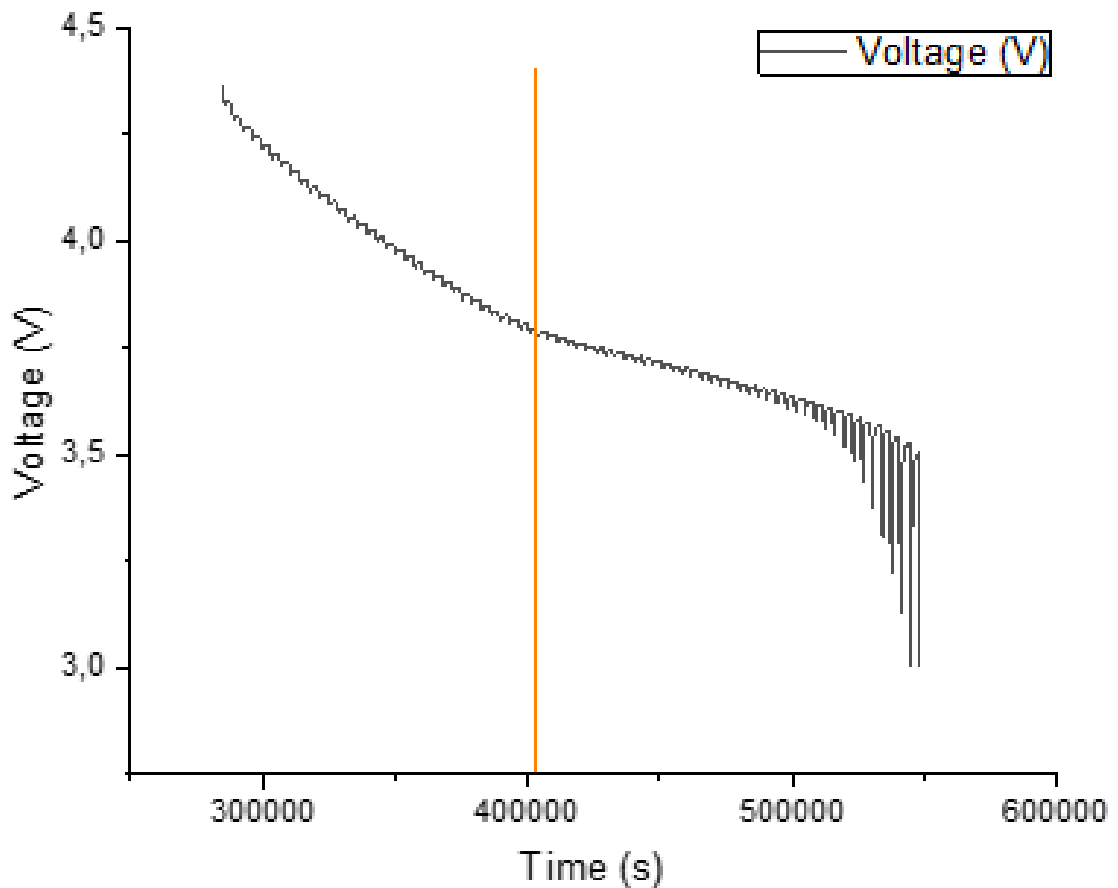


Figure 2.8: Potential vs time curve of performed GITT on the cell

The cell is repeatedly discharged at $C/20$ rate for 15 minutes followed each time by a relaxation period of 45 minutes. So potential (V) vs time (s) curve is obtained in figure 2.8. Looking closely to one pulse response (figure 2.9), we can observe that when the discharging pulse occurs the potential quickly decreases proportionally to IR where R is the sum of the uncompensated resistance and the charge transfer resistance. After that, the potential starts decreasing slowly, due to the

galvanostatic discharge pulse. Instead, during the following relaxation time the potential suddenly increases proportionally to IR and then again keeps increasing very slowly until it reaches the equilibrium ($\frac{dE}{dt} = 0$) at the open circuit voltage.

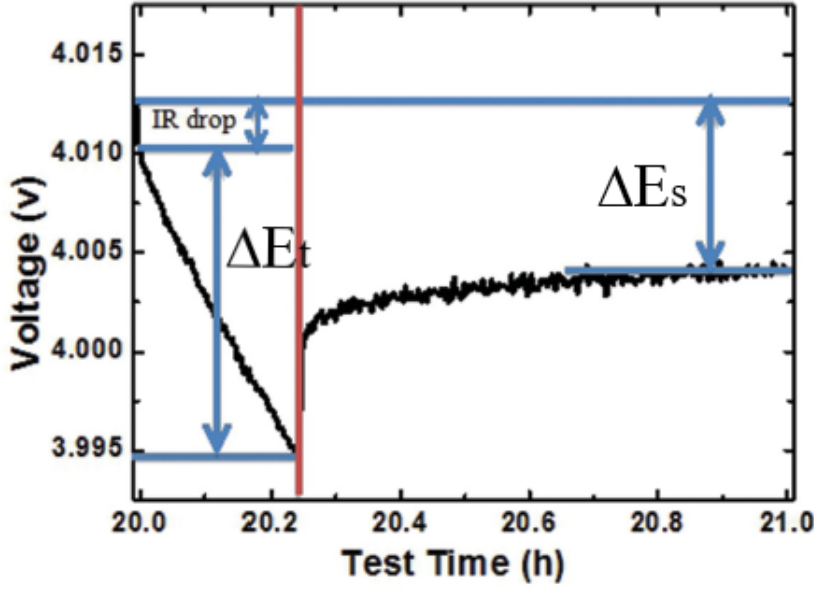


Figure 2.9: Discharging pulse [26]

Since the discharge current is constant, the voltage is function of time; assuming this is a 1D diffusion process and neglecting the double layer effect and the phase transformation, the chemical diffusion coefficient $D_s [\frac{m^2}{s}]$ can be calculated according to the Fick's law by the following equation:

$$D_s = \frac{4}{\pi} \left(\frac{IV_m}{z_A F S} \right)^2 \left[\frac{\left(\frac{dE}{d\delta} \right)}{\left(\frac{dE}{d\sqrt{t}} \right)} \right]^2 \quad (2.25)$$

where

- I is the current applied [A]
- V_m is the molar volume of the electrode $[\frac{cm^3}{mol}]$
- z_a is the charge number
- F is the Faraday constant equal to $96485 \frac{C}{mol}$
- S is electrode-electrolyte contact area $[cm^2]$
- $\frac{dE}{d\delta}$ is the slope of the titration curve of each titration step

- $\frac{dE}{d\sqrt{t}}$ is the potential variation over the time pulse

If sufficient small currents are applied for short time intervals, so that $dE/d\sqrt{t}$ can be considered linear and the coulometric titration curve can be also considered linear over the composition range involved in that step [26], the (2.25) becomes:

$$D_s = \frac{4}{\pi\tau} \left(\frac{n_m V_m}{S} \right)^2 \left(\frac{\Delta E_s}{\Delta E_t} \right)^2 \quad (2.26)$$

where τ is the duration of the current pulse in seconds, and n_m is the number of moles, while ΔE_s is the steady-state voltage difference between the previous step and the current one, measured both at the equilibrium ($\frac{dE}{dt} = 0$), and ΔE_t is the potential drop due to the galvanostatic discharge pulse (that is the one without the strictly drop due to IR). For the sake of comprehension, these intervals are pointed out in figure 2.9. Furthermore, approximating the NMC particles as spherical, and finding a consistent value for an equivalent radius r_p so that it can compensate the variance of particle radius due to their Gaussian distribution, as done in paragraph Particle radius, the (2.26) can be rewritten as:

$$D_s = \frac{4}{\pi\tau} \left(\frac{r_p}{3} \right)^2 \left(\frac{\Delta E_s}{\Delta E_t} \right)^2 \quad (2.27)$$

since it holds true that

$$r_p = \frac{3\bar{V}}{\bar{S}} \quad (2.28)$$

where \bar{V} and \bar{S} are the average volume and the average surface area of the particles, respectively.

Naming x the ratio between the lithium contained in the porous matrix over the maximum lithium concentration, it is mandatory notice that the GITT is accurate only for $0.2 < x < 0.5$ interval. Wherein the GITT curve is actually linear. Hence, the diffusion coefficient is computed using a pulse included in the $0.2 < \text{SOC} < 0.5$ range.[26] As mentioned above, the thermal model considers the temperature dependency of electrochemical parameters; the diffusion coefficient is undoubtedly one of them, so here an empirical Arrhenius relationship has been invoked. Through the equation 2.27 a reference diffusion coefficient $D_{s,ref}[\frac{m^2}{s}]$, related to a reference temperature $T_{ref}[K]$, is obtained. Clearly, the reference temperature is the one at which the GITT has been conducted, which is the ambient one, $T_{ref}=288.15$ K.[27] Finally, the diffusion coefficient depending on temperature is estimated by the Arrhenius equation 2.29

$$D_s = D_{s,ref} \exp\left[-\frac{E_a}{R}\left(\frac{1}{T} - \frac{1}{T_{ref}}\right)\right] \quad (2.29)$$

Where E_a is the activation energy of the specific cathode, which in this case is equal to $58 \frac{kJ}{mol}$ [28]

Results are reported in figures 2.10 and they have been found consistent with data in literature.

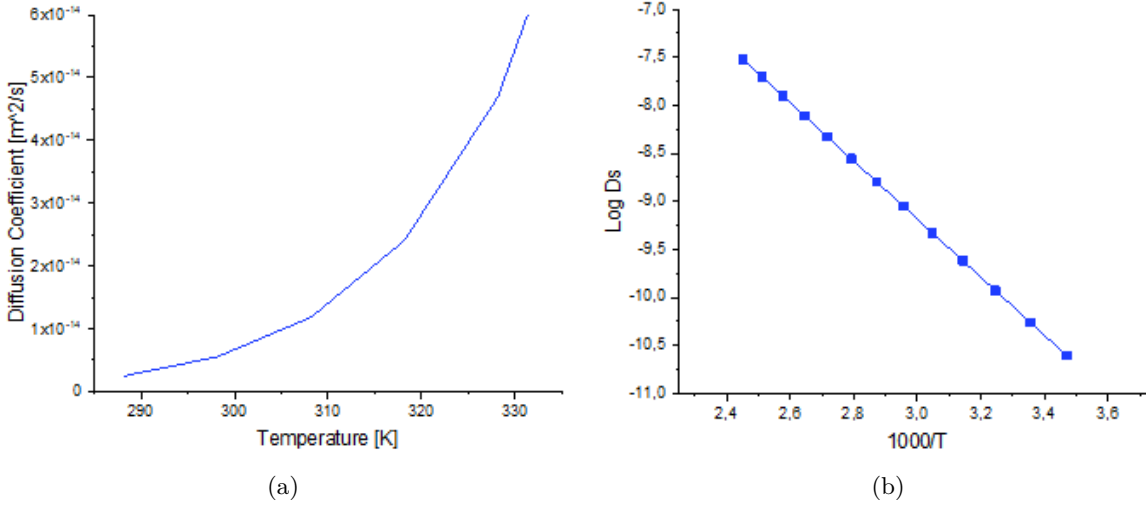


Figure 2.10: Result of GITT (a) in temperature dependence (b) in logarithmic scale vs $1000/T$

2.3.5 Equilibrium Electrode Potential

The equilibrium state of a lithium-ion battery refers to a state where concentration of lithium ions within the solid and the liquid becomes uniformly distributed, and, as a result, no potential difference is present: thus the equilibrium potential curve is the Open Circuit Voltage (OCV) curve varying with the amount of lithium-ions intercalated in the porous electrode.[17] Theoretically, in order to determine the real equilibrium potential, relaxation experiments are required. They consist in very small charge or discharge pulses, followed by relaxation steps during which no current is applied (open circuit voltage conditions), and the measured potential is the one obtained when it stops changing during the relaxation step. Since this kind of measurement is too much time requiring, a very slow galvanostatic experiment, that will give back a pseudo equilibrium potential curve, has been performed in this work.[16] Any changes in electrodes composition affect the shape of the equilibrium potential curve, thus, it is mandatory to determine this parameter by direct measurements. Condition of C/25 charge or discharge current rate, for the galvanostatic experiment, are considered to be slow enough so that the potential measured approximates the

real open circuit voltage for each stoichiometry [32],[15]. Unfortunately, it wasn't possible to find any equilibrium potential vs capacity curve for the NMC622 in literature, which, for the sake of validation, would have been compared with the measured one. Yet, a sort of check out can be performed: as soon as the discharge is completed and the potential is therefore at 3 V we can wait one minute of rest and check again the equilibrium potential. If the new rested value is not too far from the 3 V, it can be assumed that the cell was, closely, at the equilibrium state and, thus, the C-rate was slow enough to consider the obtained curve reliable.[16]

The equilibrium potential of the lithium is always zero. On the other hand, the equilibrium potential of the cathode material changes with the state of charge, and thus, results from the galvanostatic experiment are displayed in figure 2.11. The equilibrium potential E_{eq} changes along with the lithium concentration variation in the electrode. For this reason, the OCV measurements are plotted against the stoichiometry x , which is defined as the ratio of the instantaneous lithium concentration in the solid active material and the maximum concentration; $x = \frac{c_s}{c_{s,max}}$. When the cell is fully charged, the positive electrode is considered bare of lithium, and so $x=0$; during the discharge, ions intercalate in the positive electrode and x increases up to the value of 1, when the ion concentration in the positive electrode is at its maximum value. So the reported figure is a voltage vs stoichiometry curve.

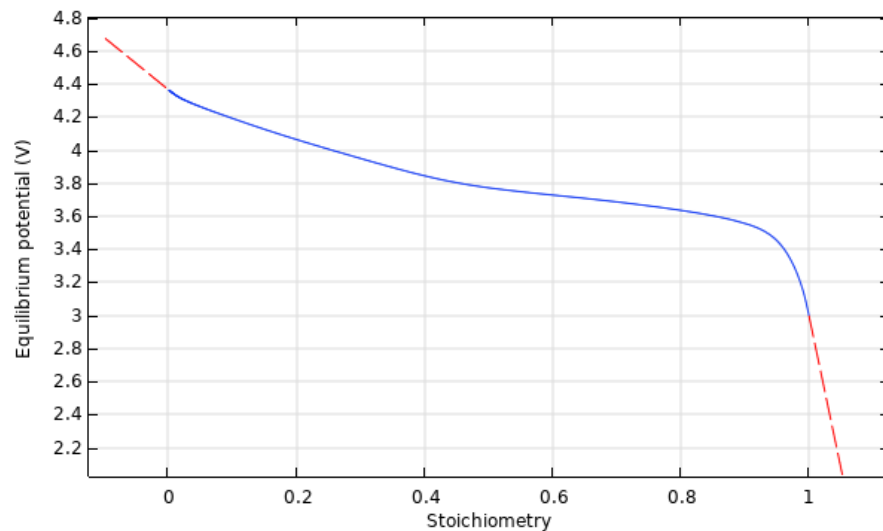


Figure 2.11: Variation of NMC622 equilibrium potential with increasing stoichiometry

2.3.6 Entropy factor

The equilibrium potential is one of the electrochemical parameters which depends on the thermal behaviour of the battery according to the equation

$$E_{eq}(T) = E_{eq}(T_{amb}) - (T - T_{amb}) \frac{dE_{eq}}{dT} \quad (2.30)$$

where $\frac{dE_{eq}}{dT}$ [$\frac{mV}{K}$] is the entropy coefficient. The latter reflects the variation of entropy due to the reversible reactions occurring at the electrodes. Curves of the entropy change with the SOC for NMC622 cathodes have been found in literature [33] and related entropy coefficient has been derived through the expression 2.31.

$$\frac{dE_{eq}}{dT} = \frac{\Delta S}{F} \quad (2.31)$$

And reported on the graph 2.12

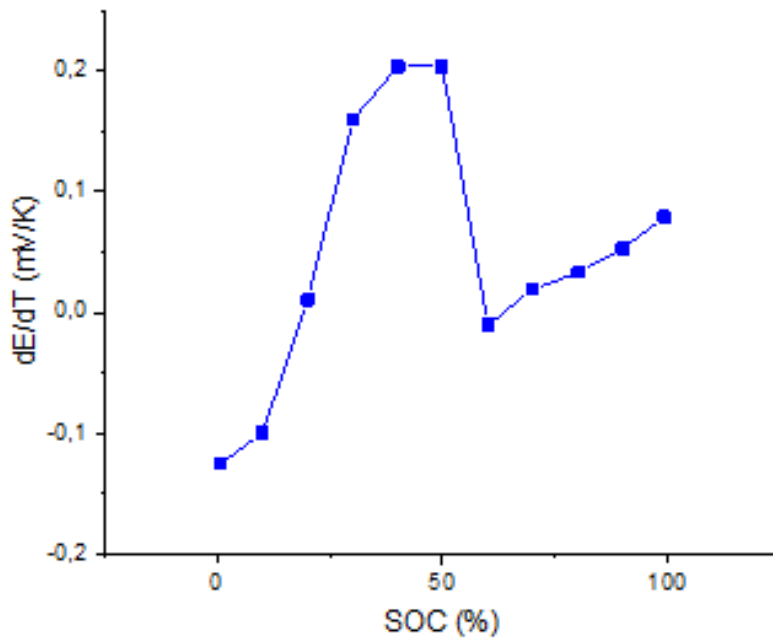


Figure 2.12: Entropy coefficient vs SOC

The abrupt slope change in dE/dT profile, at about 55% SOC, can be ascribed to a disordered-to-ordered phase transition in the layered cathode which requires less overpotential, thus, generates less heat. [59]

2.3.7 Electrode volume fraction

For the purpose of the modelling, an indispensable parameter is the fraction of volume occupied by the active material of NMC622 cathode involved in reactions. The volume fraction of active material in the lithium metal foil is assumed equal to 1, since its entire volume can possibly participate to the redox reactions. Instead, in order to obtain the NMC622 volume fraction ϵ_s , the following balance equation is called up:

$$\epsilon_s c_{s,max} d\Delta x F = it \quad (2.32)$$

where

- d is thickness of the electrode [mm]
- Δx is the variation of the stoichiometry
- i is the current density [$\frac{A}{mm^2}$]
- t is the duration time of the charge or the discharge [s]

Applying this formula to a full discharge of a battery, Δx is equal to 1, having assumed that x (defined as $x = \frac{c_s}{c_{s,max}}$) is zero at the beginning of discharge and 1 when the discharge is over. Indeed, a full battery was cycled 3 times at a 0.1C current rate in order to activate it and then again was discharged at 0.1C current rate. Determining the discharge time from the experimental data a volume fraction ϵ_s equal to 0.3217 was found.

2.3.8 Exchange current density

An Electrochemical impedance spectroscopy (EIS) analysis is conducted by giving, as input, an AC voltage (that usually is alternated around the OCV value), which causes an AC current in response, that will have a phase angle difference θ with respect to the AC voltage. AC voltage $V(t)$ and AC current $I(t)$ are described by equations:

$$V(t) = V_m \sin(\omega t) \quad (2.33)$$

$$I(t) = I_m \sin(\omega t - \theta) \quad (2.34)$$

$$\omega = 2\pi f \quad (2.35)$$

where

- V_m [V] and I_m [A] are the maximum voltage and current, respectively
- ω is the angular frequency [rad/s]
- f is the frequency [Hz]

The resistance countered in the cell, is expressed by the complex number called impedance Z , which is, indeed, defined as:

$$Z(\omega) = \frac{V(t)}{I(t)} \quad (2.36)$$

It is dependent with the voltage and current waves frequency, and being a complex number it is described by two element: the real part (Z') and the imaginary part (Z''). Both of them depend, cosinusoidally and sinusoidally, on the phase angle θ , and can be expressed on the complex plane as a point. For each frequency, which is linearly varied during EIS measurements, there is a point, and the union of all this impedance (Z) values is the Nyquist graph. An explicative example is given in figure 2.13.

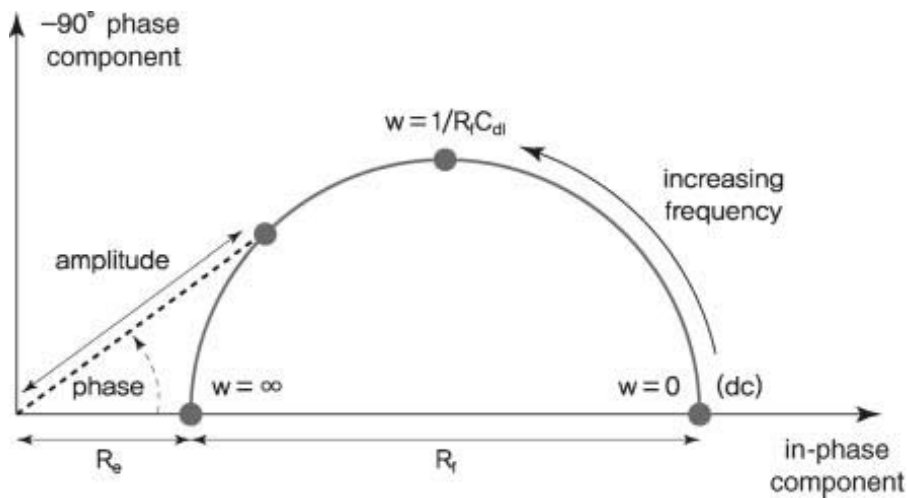


Figure 2.13: Example of a Nyquist plot

The current response implies the presence, within the cell, of resistance, capacitance and inductance, which, indeed, are the one needed to be measured. Generally speaking, impedance measurements can be modelled by an equivalent circuit composed by resistance, capacitance and inductance components, which, assuming certain values, give back the fitted curve of the Nyquist plot. In this work, EIS measurement, at OCV voltage, with a potential amplitude of 10 mV, and in the frequency range of 10 mHz to 500 kHz, at different temperature, namely 25°C, 30 °C, 40°C,

50°C and 60°C, have been performed in order to compute the charge transfer resistance R_{ch} and, thus, the reference exchange current density j_0 . In figure 2.14 are showed EIS spectra of an half cell Li|Celgard+EC:DEC LiPF₆ 1M|NMC622 for all the inspected temperature. Visualization

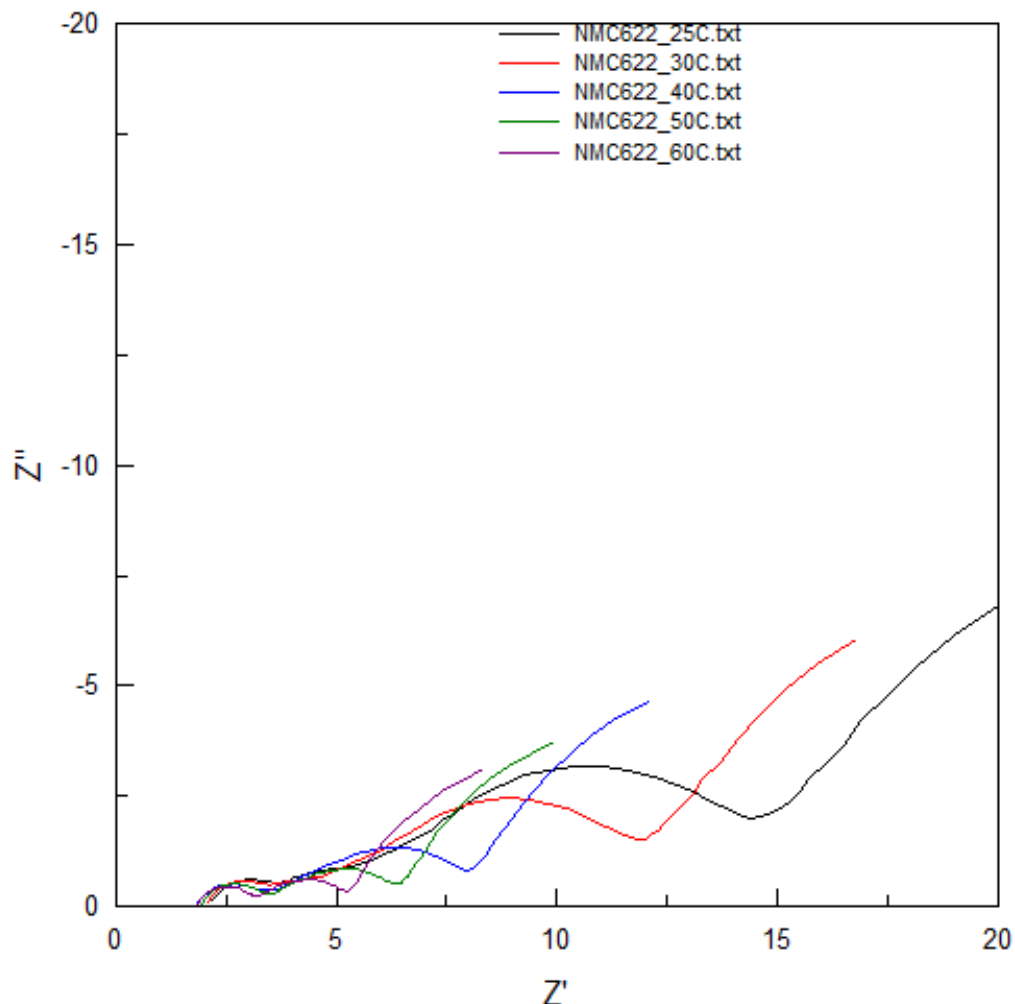


Figure 2.14: EIS spectra for NMC cathode at different temperature.

of these curves, helps to verify that the first semicircle for all the curves, doesn't change very much with the increasing of temperature, since it is due to the SEI resistance, which doesn't depend so much with the temperature. The semicircle besides, whilst, is representative of the charge transfer resistance, which varies significantly with temperature. The proposed equivalent circuit, represented in figure 2.15, models different phenomena, occurring in the cell and causing a certain overpotential, through electrical components, including resistance R and constant phase element (CPE): the ion transport in electrolyte has a resistance component R_1 ; the parallels R_{SEI} and (CPE_{SEI}) describe the diffusion through the SEI; ion movement in the porous electrode and

ion diffusion through the active material/electrolyte interface is modelled with R_{ch} and CPE_{ch} ; and finally a CPE_1 is used to fit non linear data at low frequencies. [20] The charge transfer

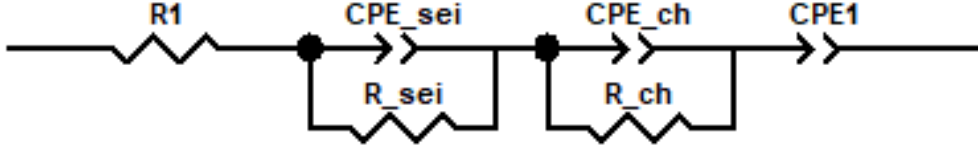


Figure 2.15: Equivalent circuit proposed for this EIS spectra fitting.

resistance in the electrode R_{ch} is the one required to obtain the reference exchange current j_0 . Indeed, considering the Butler-Volmer equation (2.11), for small overpotential η , like in case of EIS tests, the B-V can be linearized to the form:

$$j = j_0 \frac{F\eta}{RT} \quad (2.37)$$

The overpotential can be expressed also by means of R_{ch} , accordingly to:

$$\eta = jSR_{ch} \quad (2.38)$$

where $S [m^2]$ is the active electrode/electrolyte surface area. Finally, the reference exchange current density for the porous NMC cathode, has been computed through:

$$j_0 = \frac{RT}{R_{ch}SF} \quad (2.39)$$

Using the R_{ch} for 25°C, which has been computed equal to 3.46 Ω , j_0 is calculated equal to 2.88 A/m^2 .

2.3.9 Physico-chemical parameters from literature

Since it has been proven that for C-rate lower than 10C, the variation of transport number doesn't affect the results [61], a mean value of experimental data found in [45] is used and reported in table 2.2. On the other hand, temperature and concentration dependence of the thermodynamic

factor $\left(1 + \frac{\partial \ln f}{\partial \ln c_l}\right)$ is considered and reported thereby from the source [45]:

$$\left(1 + \frac{\partial \ln f}{\partial \ln c_l}\right)(1 - t_+) = 0.601[1 - 0.399334c_l^{0.5} + 1.63394(1 - 0.0052c_l^{1.5}(T - 294))] \quad (2.40)$$

Its dependence on temperature is almost negligible, whereas it increases with the electrolyte ions concentration. Furthermore, the initial electrolyte salt concentration is provided by the manufacturer. The effective transport parameter correction, the Bruggeman coefficient, which allows us to take into account the effect of tortuosity on diffusion of the electrolyte and conduction of the electrolyte and the porous electrode, is the one suggested by the software Comsol. For the electrolyte conductivity and diffusion coefficient the same concentration and temperature dependent parameters, already proposed in Comsol, have been assumed.

Maximum Li-ion concentration that the porous NMC622 cathode can stand and its electrical conductivity are the ones referred in [47].

Aluminium conductivity is well known and so the one from the Comsol library has been chosen.

Table 2.2: Electrochemical parameters from literature and Comsol library

Parameter	Unit	Electrolyte	NMC Porous electrode	aluminium current collector
Transport number		0.363		
Electrolyte salt concentration	mol/m^3	1000		
Bruggeman coefficient		1.5	1.5	
Maximum concentration	mol/m^3		59493	
Electrical conductivity	S/m	0.771	10	$3.774 \cdot 10^7$

2.3.10 Thermal-model parameters

Density

The density assumed for the inner active volume is the average density of all the component, which are negative electrode, separator, positive electrode, positive current collector. All of their density contribution to the average is weighted on their volume. The density of each of them ρ_i is multiplied for their volume fraction, and then they are added together.

$$\bar{\rho} = \rho_{NE} \frac{V_{NE}}{V_{TOT}} + \rho_{SP} \frac{V_{SP}}{V_{TOT}} + \rho_{PE} \frac{V_{PE}}{V_{TOT}} + \rho_{CC} \frac{V_{CC}}{V_{TOT}} \quad (2.41)$$

Density for lithium electrode, Celgard and aluminium current collector are the one proposed in Comsol library. While for NMC it was easily computed knowing his weight and volume.

Table 2.3: Density values for all materials and the averaged one.

Li-metal Kg/m^3	Celgard Kg/m^3	NMC622 Kg/m^3	aluminum Kg/m^3	Average value Kg/m^3
535	1043	2906	2700	1804

Heat capacity

For the heat capacity at constant pressure stands exactly the same assumption made for the mass density.

$$\bar{C}_p = C_{NE} \frac{V_{NE}}{V_{TOT}} + C_{SP} \frac{V_{SP}}{V_{TOT}} + C_{PE} \frac{V_{PE}}{V_{TOT}} + C_{CC} \frac{V_{CC}}{V_{TOT}} \quad (2.42)$$

For the specific heat capacity of the NMC622 cathode material, a Differential Scanning Calorimetry (DSC) has been performed. It is a thermoanalytical technique that consists in providing a heat flux to a sample in order to increase its temperature at a certain rate and look at the flux demanded. Indeed, results are given as the difference of heat required by the sample with respect to a reference material (maintained at the same sample's temperature), as a function of the temperature. For the analysis, NMC powders and reference material were equilibrated at constant temperature of 40 °C for 2 minutes. Then, with a rate of 5°C per minute, samples, placed in high pressure capsules filled with argon, have been heated up to 350°C. A Thermogravimetric analysis (TGA) (widely explained in paragraph [Thermogravimetric Analysis](#)) has also been performed on the NMC material in air atmosphere up to 800°C. The latter, briefly, consists in heating the material in order to observe its mass variation, caused by oxidation and decomposition. In figure 2.16, TGA (a) and DSC (b) results are depicted. The TGA analysis is aimed at detecting the temperature stability window of the material, which in this case is comprised between 40°C and 233 °C, where no decomposition or oxidation is taking place. The curve in this interval is, indeed, almost horizontal, unless a very small slope probably ascribed to the humidity loss. Only for temperatures higher than 233°C, significant changes in curve slope and so in material composition, can be revealed. Once the temperature range, in which the substance is stable, has been found, DSC data has been extrapolated from this exact interval in order to compute the specific heat

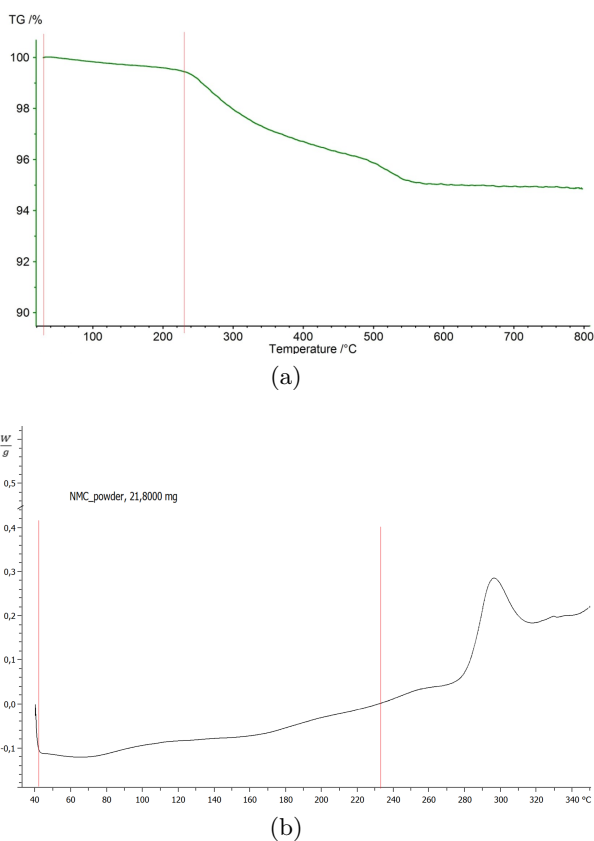


Figure 2.16: NMC622 result curves for TGA (a) and DSC (b), thermal stability interval is outlined by vertical dashed lines.

capacity of NMC622 substance. [60] The heat capacity is determined by the equation:

$$c_p = \frac{1}{m} \frac{\frac{\partial Q}{\partial \tau}}{\frac{dT}{d\tau}} \quad (2.43)$$

where $\frac{\partial Q}{\partial \tau}$ is the heat flux provided by the DSC plot, m is the sample mass and $\frac{dT}{d\tau}$ is the temperature rate of the sample. [60] The specific heat capacity obtained is equal to 1280 J/(Kg K).

Table 2.4: Specific heat capacity at constant pressure values for all materials and the averaged one.

Li-metal	Celgard	NMC622	aluminum	Average value
$J/(KgK)$	$J/(KgK)$	$J/(KgK)$	$J/(KgK)$	$J/(KgK)$
3600	1688	1280	900	1967

Thermal conductivity

Thermal conductivity has instead been assumed anisotropic, thus, a value along the thickness direction K_{\perp} (perpendicular to the discs surfaces) and a value along the discs surfaces K_{\parallel} (parallel

to the discs surfaces), have been computed by the equations 2.44 and 2.45, respectively.

$$\frac{L_{tot}}{K_{\perp}} = \frac{L_{NE}}{K_{NE}} + \frac{L_{SP}}{K_{SP}} + \frac{L_{PS}}{K_{PE}} + \frac{L_{CC}}{K_{CC}} \quad (2.44)$$

$$K_{\parallel} = \frac{L_{NE}K_{NE} + L_{SP}K_{SP} + L_{PE}K_{PE} + L_{CC}K_{CC}}{L_{TOT}} \quad (2.45)$$

where L_i are the respective thickness. As for density and capacity, values for lithium, Celgard and aluminium have been taken from Comsol library. Since very few literature up to now have treated NMC622 material, it wasn't possible to find any value neither to experimentally obtain the NMC622 thermal conductivity. Since the value for NMC811, easy to retrieve, has the same chemical elements of NMC622 and very similar proportion, NMC622 thermal conductivity has been assumed equal to the NMC811.

Table 2.5: Thermal conductivity values for all materials and for the perpendicular and parallel conductivity components.

Li-metal $W/(mK)$	Celgard $W/(mK)$	NMC622 $W/(mK)$	aluminum $W/(mK)$	K_{\perp} $W/(mK)$	K_{\parallel} $W/(mK)$
84.8	1.21	1.58	238	2.25	52.27

2.4 Model results and validation

2.4.1 Electrochemical validation

At this point, when all the required parameters have been evaluated and measured, it's time to validate these parameters themselves and the completed model. For this purpose, firstly, experimental data have been obtained by direct measurements. A full cell has been assembled and galvanostatically cycled at different C-rate, namely C/10, C/5, C/2 and 1C. Then, the model, coded to simulate the discharge phase, has been launched for each different C-rates. Arrived at this stage, experimental data and simulation results have been compared also graphically. Lower C rate (C/10 and C/5) curves are showed in figure 2.17. On the premise that the model simulates the discharge of a cell that has been fully charged and then made rest for a certain time, its voltage profile starts from the open circuit voltage, that is slightly lower than the cut-off voltage of 4.4 V (0.14 V lower). Then, as can be noticed from figures (a) and (b) of 2.17, the simulated discharge time is moderately lower than the experimental. Moreover, the model plots become more accurate

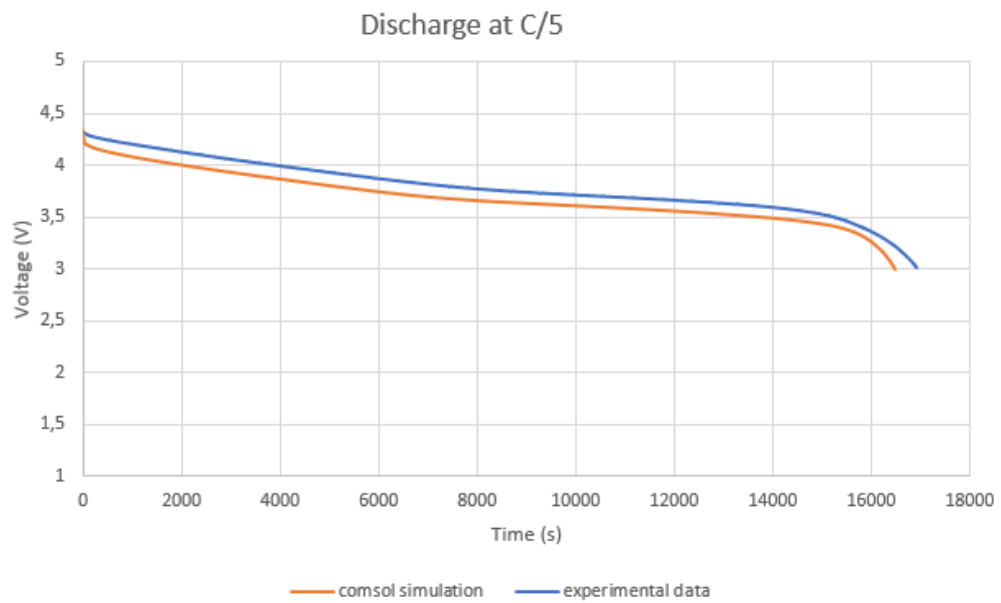
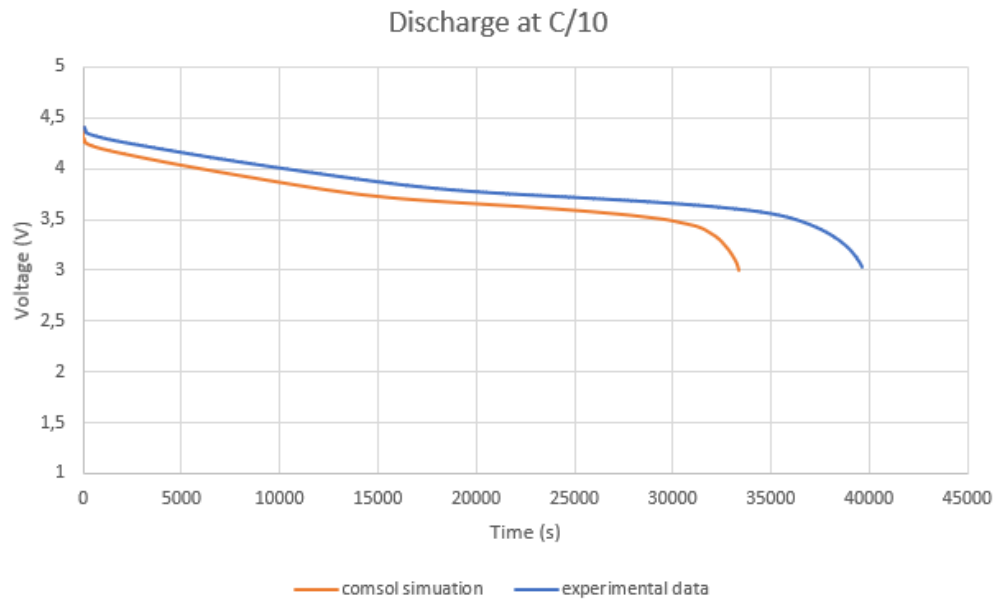


Figure 2.17: Voltage profiles of direct measurements (blue line) and model results (orange line) at C/10 (a) and C/5 (b)

with the increase of the C-rate, from C/10 to 1C. Potential profiles for 1C rate and C/2 rate are exhibited in figure 2.18. This is representative of the fact that the model is more performant in predicting the cell behaviour along with the inner temperature increase, since more than one electrochemical parameter has been considered variable with temperature, including the diffusion coefficient and the equilibrium potential.

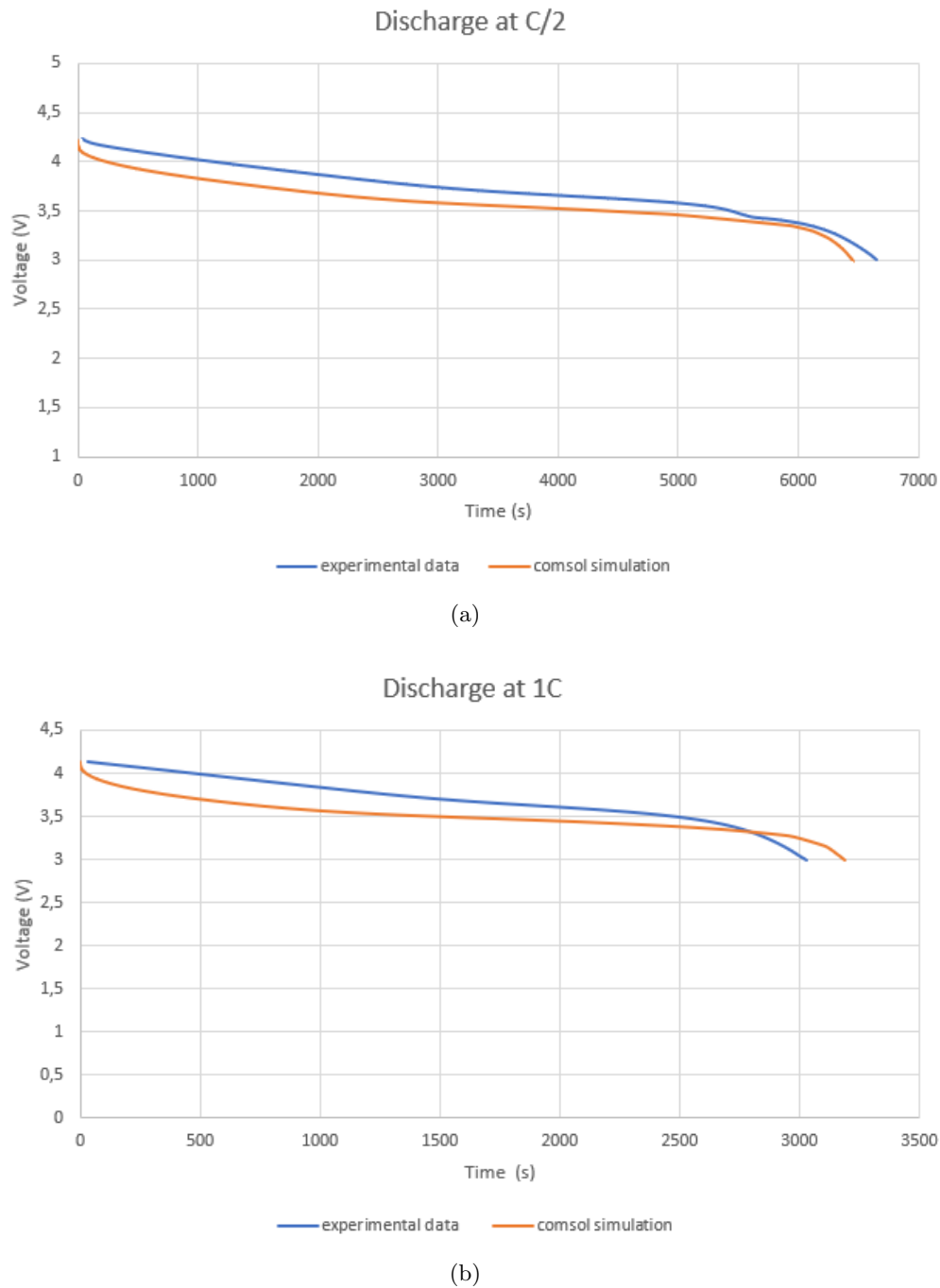


Figure 2.18: Voltage profiles of direct measurements (blue line) and model results (orange line) at C/10 (a) and C/5 (b)

2.4.2 Thermal analysis

Relating to the thermal behaviour of this system, it was not possible to make a comparison with experimental data of temperature profiles. Nevertheless, it is still very useful to analyse the simulation results. Hereby, few important concepts, already mentioned above, are recalled

to mind. Irreversible heat generation is the sum of different overpotential contributions: ohmic loss, charge transfer resistance and mass transport resistance due to diffusion phenomena. The rate of insertion and extraction of lithium, along with diffusion and conduction resistances, are always exothermic events, and are directly dependent with the current applied. Simultaneously to irreversible heat generation, changes in crystal lattice for hosting or extracting ions in the porous electrode can require both, to absorb some energy, along with generating a certain amount of heat depending on the SOC. Thus, this reversible heat generated by the arrangement of crystals to accommodate ions intercalation or deintercalation, can be exothermic or endothermic, and this behaviour dependent with the SOC is partially described by the entropy factor (paragraph [Entropy factor](#)). Hence, in figure 2.19, temperature curves for different C-rate, obtained by the simulations, are depicted. As expected, at lower C-rates the heat produced is lower than for

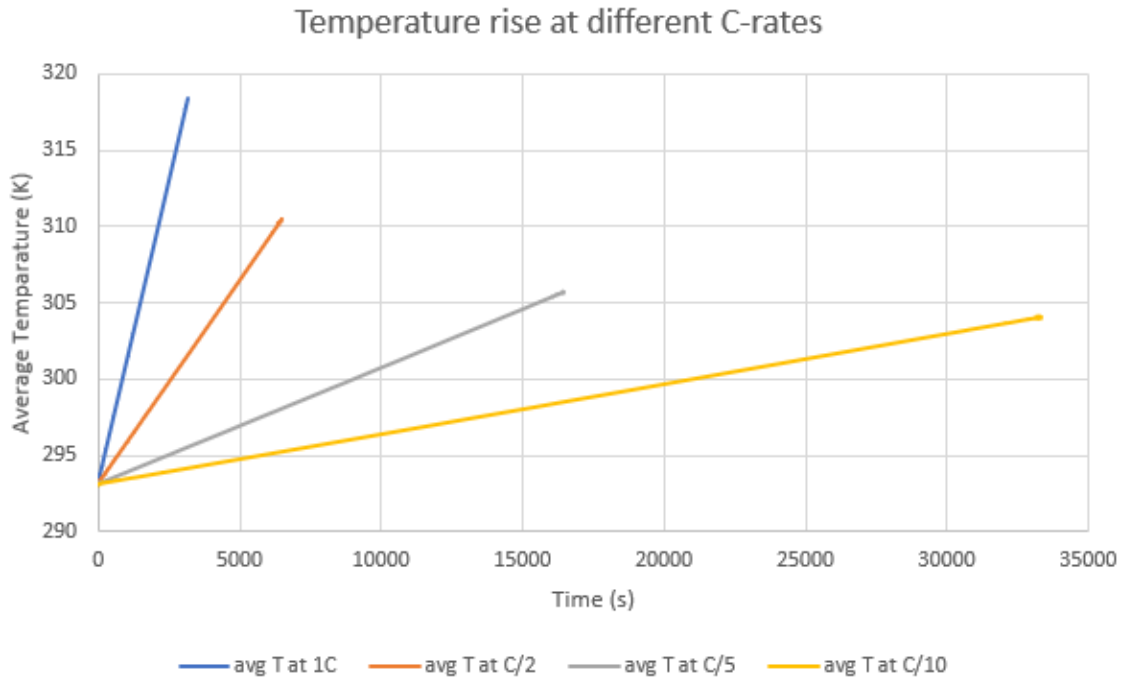


Figure 2.19: Temperature profile for simulations at 1C (blue line), C/5 (orange line) and C/10 (grey line)

higher C-rates, because reversible heat is practically the same for each current density, while the irreversibilities increase with the C-rate. Additionally, consistently with literature, the temperature during discharge is always increasing. Specifically speaking, in the separator layer the only heat generation to account for, is the irreversible source due to the diffusion of materials and, thus, is always exothermic. The reversible heat generation occurring in the electrode, due to the Li-ion intercalation and deintercalation, is quantified by the entropy coefficient. As observable from figure

2.12, reversible heat generation due to the intercalation of lithium (discharge) has a cooling effect for SOC lower than 20%, therefore in proximity of the finishing of discharge. This is because, at this Depth Of Discharge (DOD), where the concentration in the solid active material is near to the maximum one, intercalating is more energy demanding for each Li-ion. Along with this heat sink, irreversibilities generated in the electrode are almost constant for all the Depth of Discharge, but, internal resistance to diffusion and conduction is increased at the end of discharge, causing, as well, an increase of the heat generated. [33] In this way, for DOD around the 80%, a sort of heat compensation is taking place, resulting in no increase in the average temperature curve slope. Considering also that lithium deposition and stripping don't represent relevant heat sources, the entropy generation of the anode has been neglected. So, lithium anode do not participate to the heat generation, but it does to the heat transfer. Effects of this assumption are represented by the linearity of the average temperature increase. Heat generated in the electrolyte and cathode is equally distributed in all volume, where the one not responsible for heat generation, but able to absorb it, has the highest volume among the other layers. Finally, not very high temperature have been reached, besides convection and irradiation have not been modelled. This is because of lithium significant heat capacity. As visible from 3D representation of the cell layered structure 2.20, for discharge of 1C the temperature increases linearly from 293.15 to 318.54 K and uniformly in the volume, considering lithium high thermal conductivity.

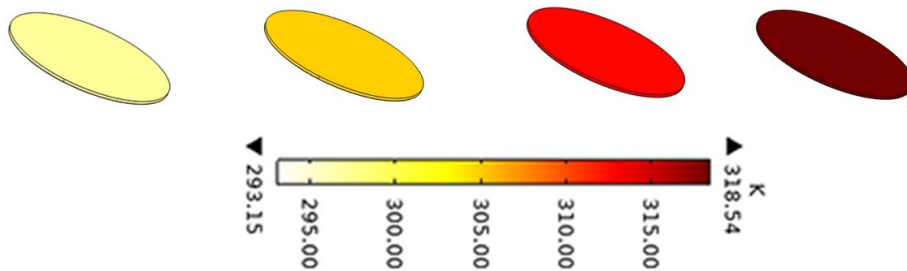


Figure 2.20: Evolution of average temperature in the cell volume throughout the discharge phase.

Chapter 3

Lithium protection

The safety problem of li-metal batteries plagued their practical application for a long time. As already mentioned in the first chapter, dendrites uncontrolled formation may cause a short circuit which eventually brings to a thermal runaway. Beyond accidental shorted out cells, other abusing, including overcharging and high temperature operation, lead to an increase in temperature that is also the initiator variable for the decomposition of cobalt oxides, used very often as cathode material. The released oxygen represents the first ignition source of consequent fire and explosion. Liquid electrolyte are usually solutions of organic solvent and inorganic salt, exactly like the one used in this work: two solvents, namely the ethylene carbonate (EC) and diethyl carbonate (DEC) enriched with lithium hexafluorophosphate LiPF_6 . This electrolyte is flammable and highly reactive with the released oxygen. Cathode and electrolyte thermal decomposition are exothermal; chemical reactions happening are exothermal too. The rise in temperature means that more particles are reaching the activation energy, starting a chain reaction which will generate gases increasing the inner cell pressure. The sum of all these dangerous factors leads to the ignition of the liquid electrolyte and eventually the cell is blasted to fragment. Against any design project, the cell is no more externally insulated, and the contact with the external air unavoidably provokes fires and explosions. [34] Therefore, safety issues hindered up nowadays further developments of high energy density Li-metal and high loading electrodes. An in-depth understanding and persistent investigations in material science and advanced design of the lithium anode and electrolyte interface are the main tools toward the protection of lithium anode and finally the appreciation of its incredible potential. For this purpose, polymer electrolytes are generating day by day more interest and enthusiasm from the research communities. Persistence of pioneering studies have found in them the requested

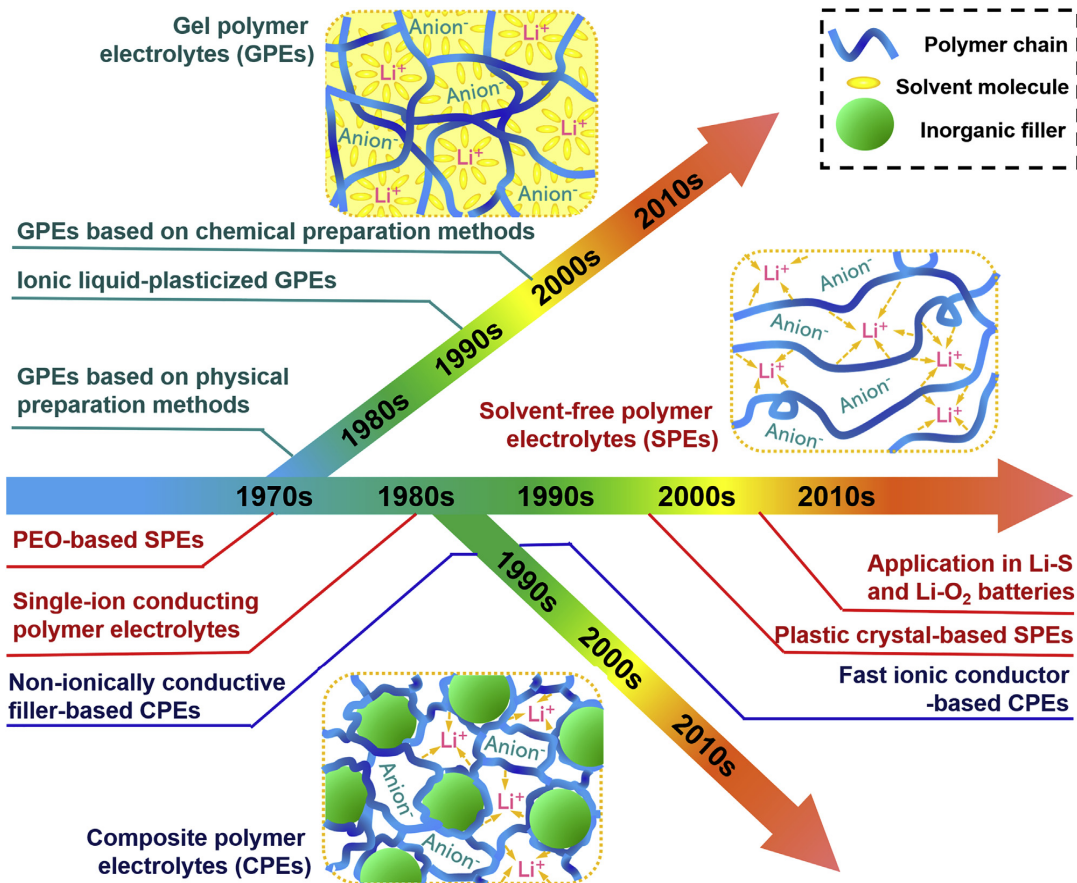


Figure 3.1: Pioneering development of polymer electrolyte throughout the years [39]

qualities for a safe electrolyte implementation: low flammability; easy processability to manipulate its parameters with no harsh material processing; good electrochemical and thermal stability; high ionic conductivity and Li-ion transference number; but above all its flexibility. The latter allows to explore assemblies of polymers with different molecular weight combined with other materials, such as plasticizers, inorganic ionic or non ionic fillers, cross-linking agents. Changing their proportions gives in output different performance parameters: higher mechanical strength to stress and strain, more tolerance to vibration and mechanical deformation, better ability to absorb mechanical shock, improved wettability of the anode and thus enhanced interfacial contact.[36] In figure 3.1 is represented schematically the chronological development of this exploration in polymer electrolyte. In 1973, Fenton et al. dissolved alkali salt in polyethylene oxide (PEO) obtaining a conductive complex which will be the first example of a Solvent-free Polymer electrolyte (SPE). [37] Five years later, Armand et Al. proposed a PEO matrix with Li salts solutes, performing a ion conductivity of $10^{-4} \frac{S}{cm}$. [38] Polymer of SPEs are required to have cation solvation nature for the salt dissociation, high dielectric constant for the charge separation of the salts, high molecular

weight for mechanical strength, and backbone flexibility of the amorphous phase which is the one responsible for the ion conduction through the electrolyte. [39] Since PEO at ambient temperature is mostly crystalline, its ion conductivity is quite low. In order to increase the latter, in 1975, Feuillade et al. introduced in the polymer matrix rich in salts, some liquid solvents acting as plasticizers obtaining a quasi-solid state material. [40] It was actually a Gel Polymer Electrolyte (GPE) characterized with better wettability for the anode interface, enhanced ion conductivity ascribed to the plasticizers containing dissolved Li salts, inherent safety for the minimized risk of fire and electrolyte leakage, and mechanical strength due to the polymeric matrix. However, for a high enough ion conduction too much liquid solvent is needed, decreasing safety, thermal stability, and mechanical resistance. [39] This has led to the breakthrough happened in 1988, when Skaarup et al. embedded ionic conductor fillers in the polymeric matrix gaining almost one order of magnitude of ion conductivity. [41] Incorporating ionic or non ionic conductor inorganic particles, improves mechanical properties and permits the retention of the polymer amorphous phase enhancing the ion mobility of the Composite Polymer Electrolyte (CPE). [42]

That was a very brief look to the polymer electrolyte possibilities due to their flexibility and their historical panorama from which the polymer electrolyte, proposed in this work, was born.

3.1 Composite Gel Polymer Electrolyte

Replacing conventional liquid electrolytes with polymer electrolyte has been recognized as a promising method to overcome Li-based batteries limitations. Especially in case of Li-metal and high voltage battery, like the one considered in this work, specific solutions have to be designed to accommodate the next-generation battery requirements.

- Polymer electrolytes exhibit high electrochemical oxidation resistance, allowing the implementation of electrodes with higher redox potential, like the NMC622 cathode. They can be electrochemically stable up to 4.45 V as evidenced by Dong et al. [43]
- Mechanical strength have been proven by Newman et al. to influence the dendrite growth: interfaces with shear modulus twice as high as the Li-metal one, can totally constrain the anode volume change.[44] Thus, a Young's modulus higher than 6 GPa is sufficient to inhibit the dendrite formation. [35] Polymer electrolyte matrix can show such characteristic by increasing their molecular weight, but also by introducing ceramic nanoparticles with high

hardness.

- When a cell is asked to operate at high current density, "Sand's time" occurs very soon. This is due to the fact that Li ions cannot shuffle fast enough through the electrolyte and a concentration polarization at the anode surface causes uncontrolled electrodeposition of ions onto protrusions and so dendritic nucleations. Enhancing the transport number and the ion conductivity by implementing polymer electrolytes, increases the Sand's time value (Sand's time = ∞ if lithium-ion transference = 1) and lowers the dendrite occurrence.
- Another effective way to avoid ion concentrations at the anode surface is by creating smooth Li-ion morphologies during plating and stripping. To achieve this goal, cross-linked polymer network offers micro-sized pathways for the ions through the membrane which they are forced to follow. In this way, if the current density is not exceeding the limiting one, li-ion concentration around nucleation point are retarded and a more homogeneous electrodeposition is attained.

Hence, a (butyl methacrylate)/poly(ethylene glycol)diacrylate (BMA-co-PEGDA) membrane in which different amount of inorganic zirconia nanoparticles were embedded, and further swollen with EC:DEC 1:1 $LiPF_6$, is the Composite Gel Polymeric Electrolyte evaluated in this project. The scope of this research is to take advantage of all the above listed possibilities by a protective and ion conductive CGPE. Every element of the membrane has its role in the electrolyte, so it is relevant to take a brief look at all of them.

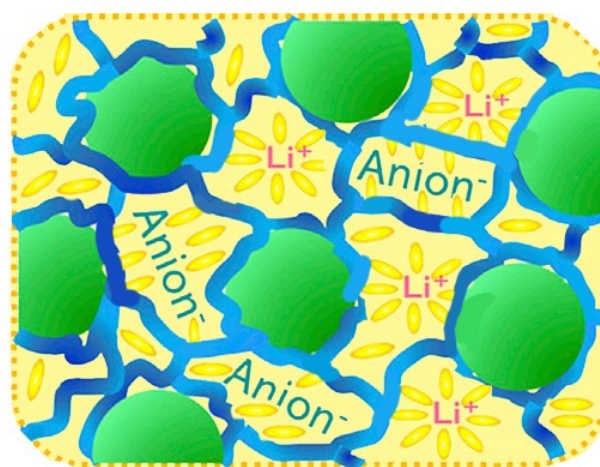


Figure 3.2: Composite Gel Polymer Electrolyte

3.1.1 Materials of interest

BPO

The benzoyl peroxide (BPO)(75% Acros Organics) is an organic peroxide and was implemented in this membrane for its thermal initiator property. It is made of two benzoyl group linked with a

peroxide bond which, if subjected to a certain heat flux, undergoes to an homolysis (displayed in figure 3.3). The breaking of this link leaves two benzoyloxy radicals, that having unpaired electrons, form two radicals very unstable and so are called free radical initiator. They are in fact very reactive against monomers. (Reference Polymer Properties Database)

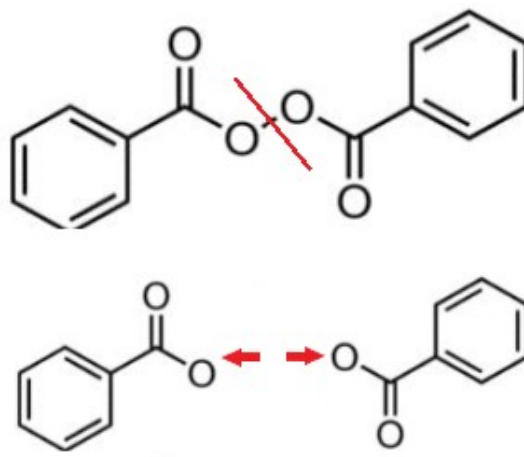


Figure 3.3: Structural formula of BPO

BMA

Considering the good results obtained by the preparation of a butyl acrylate-based membrane and showed in the report [29], the monomers buthyl methacrylate (BMA, 99% Acros Organics), was chosen, since the only difference between the two monomer is the presence in BMA of a methyl group in the place of one hydrogen of the vinyl group. With a slightly higher molecular weight with respect to BA, characteristic that can only provide stronger matrix, BMA presents a transition glass temperature T_g of 20°C, whose meaning will be explained hereafter. In figure 3.4 its structure is showed and the vinyl group responsible for polymerization is evidenced. (Reference Polymer Properties Database)

PEGDA

Polyethylene glycol diacrylate (PEGDA)(PEGDA575, Mn 575, Aldrich) is a long-chain, hydrophilic and crosslinking monomer. Its structure is shown in the figure 3.6. There are different reasons for adding this copolymer:

- 1) It is rich in ether-bonds which brings to a very good compatibility with ether-based liquid electrolyte, including the one used in this work, the EC:DEC. This compatibility allows the

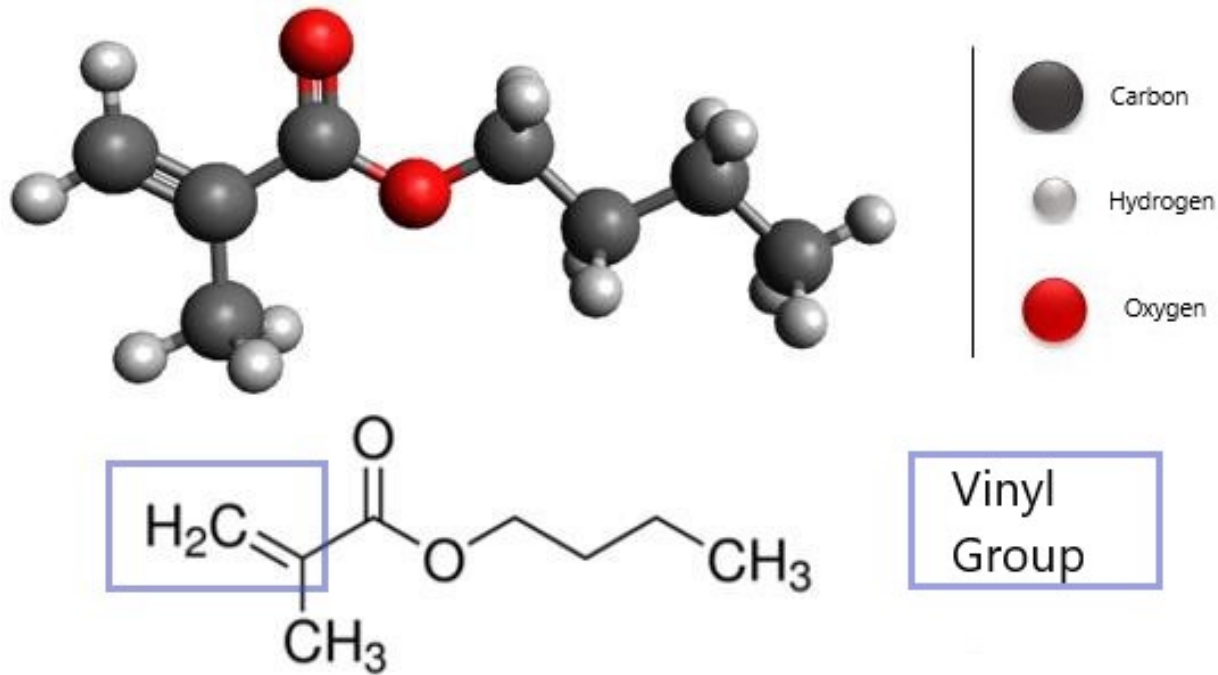


Figure 3.4: 3D representation and structural formula of BMA. The Vinyl group has been underlined

membrane to uptake the liquid, enhancing, as a result, the conductivity. [29] 2) As a significant part of the polyethylene group, they display a noticeable Li-ion conductivity that is ascribed to the segmental chain motion occurring in the amorphous phases, as schematized in figure 3.5. More is the amount of amorphous phase, more is the free volume which Li_+ can hop in and then diffuse out. By the common knowledge that lower is the glass transition temperature T_g of material, greater is the overall amorphous phase, as a matter of fact, PEGDA is characterized by the very low transition temperature of $-40\text{ }^\circ\text{C}$. Still, its very low T_g is responsible of another contribution to the ion conductivity: PEGDA shows Vogel-Fulcher-Tamman behaviour, which means that at the Vogel temperature T_0 the polymer backbone starts moving. Above T_0 lithium ion hopping site of the backbone are frequently shifting to open up at lithium ions to tether them. In the scientific world it is believed that very often, T_0 is 50°C lower than T_g , hence, such a low T_g implies faster segment movement.[31] Finally, PEGDA long chains of $-C-O-C$ also take part to the improvement of ion conductivity. [29]

3) Given its high cross-linking power, due to its double presence of vinyl groups (3.6), PEGDA allows to the formation of a highly reticulated frame, which represents for anions and cations a fine net of microsized pathways. So, Li-ions distribution is controlled and homogeneous, avoiding ions concentrations at the anode interface.

Still, PEGDA contribution to the ion conductivity is not enough since in polymer electrolyte is

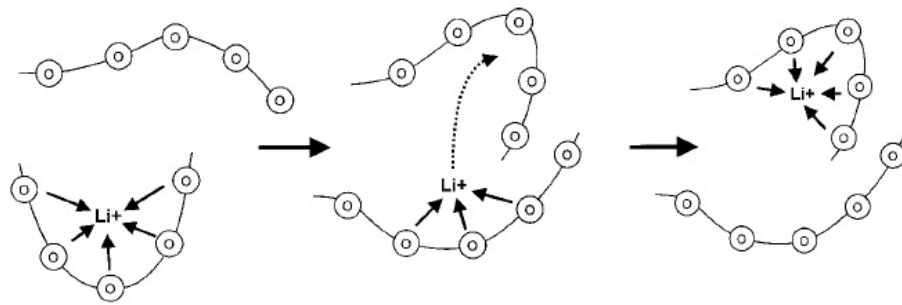


Figure 3.5: Schematic segmental motion of Li ions typical of ethers, including PEGDA [30]

always present a crystallization phase which counteracts the ion diffusion. A solution could be the addition of inorganic oxides. [30]

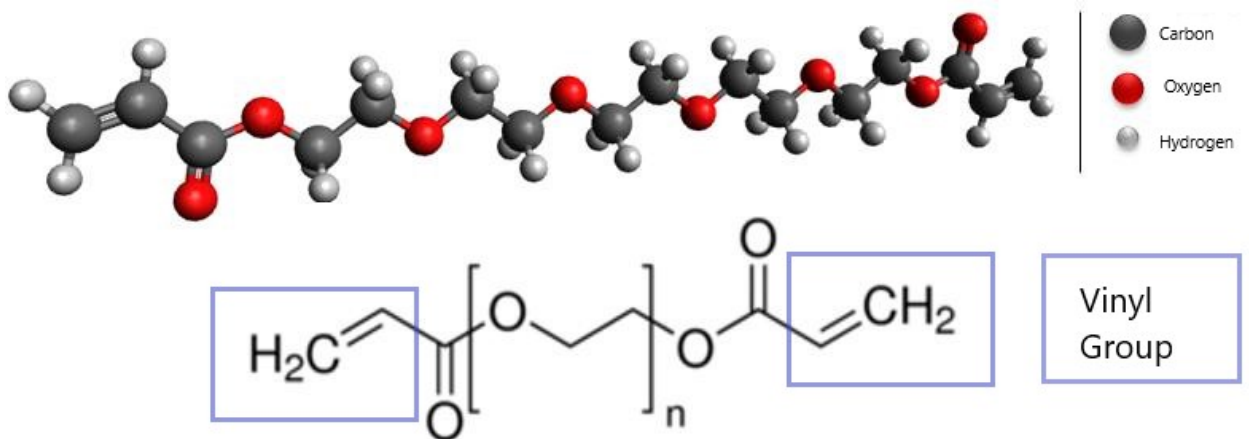


Figure 3.6: 3D representation and structural formula of PEGDA. The two Vinyl group has been underlined

Zirconia

Polymeric membranes can benefit from the agglomeration of ceramic nanosized powders, as the zirconia ZrO_2 (TZ0 Tosoh Co., Tokyo, Japan) exploited here. Ceramic fillers affect positively the ion conductivity, controlling the copolymers chain crystallization rate, up to actually hinder the crystalline regions formation. This is due to the powder large surface area which inhibits the polymer chain reorganization, preserving their degree of disorder.[42] Increasing the amorphous area is how fillers boost ion conductivity; along with the fact that zirconia is a good ionic conductor. [56]

3.1.2 Membrane synthesis

The membrane (BMA-co-PEGDA) synthesis occurs thanks to the thermally induced radical polymerization. The organic peroxide BPO, subjected to a heat flux, undergoes to an homolysis resulting in two free radical initiators. The latter are very unstable and reactive against the monomers' vinyl groups, to the point where they cleave their double bonds. As a result, at the BMA and PEGDA molecules tips there are reactive radicals, which are attracted by the other radicals to form bonds. Since BMA molecules have one vinyl group and thus one radical, these monomers will form long BMA chains; meanwhile, double radicals, at PEGDA's tips, bond with BMA chains creating a cross-linked network [3.7](#).

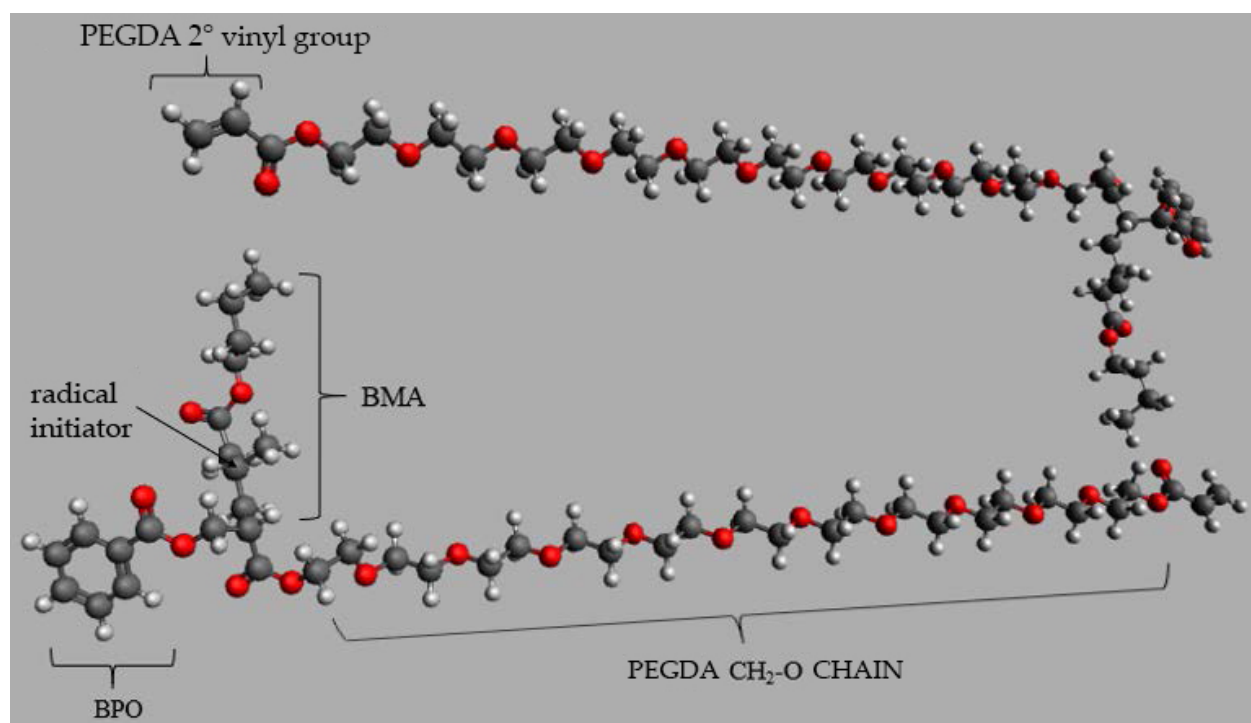


Figure 3.7: Schematic polymerization. Since PEGDA chain are characterized by two Vinyl group both of them can bond themselves with another BMA or PEGDA creating a network; this is the cross-linking

3.1.3 Membrane preparation

The butyl methacrylate/poly(ethylene glycol) diacrylate (BMA-co-10PEGDA) membranes were synthesized by thermo-initiated radical co-polymerization of BMA and PEGDA. The entire synthesis process takes place into the glove box in [Figure 3.8](#) under argon atmosphere, so that no oxygen can inhibit the polymerization. In a small glass vial is inserted firstly 0.01 g of BPO, then

different contents of ZrO_2 (32 wt%, 63 wt%, 83 wt%). By means of a micropipette, 1,12 μl of BMA and 89.3 μl (10 wt %) of the cross-linking agent PEGDA 575 are added. On a Magnetic Stirrer Hot Plate the so made precursors solution is stirred while heated up to a maximum temperature of 70°C. As soon as the blend starts becoming viscous, it is removed from the plate and casted onto a glass plate. Finally the polymerization is maintained at 45°C for 20 hours and afterwards for other 2 hours at 100°C. Whereupon the glass-slide is brought outside the glovebox, the network is peeled off in order to obtain membranes discs of 15 [mm] diameter, using a cutter. The as-prepared membranes are then dried at 90°C for 12 hours in a vacuum environment, in order to be carried again into the Glovebox argon atmosphere. Cut membranes display perfectly self-standing, smooth, flexible and translucent appearance, as showed in figures 3.9.



Figure 3.8: GloveBox MBrau® UNILab plus model

3.2 Physical-chemical characterization

3.2.1 Thermogravimetric Analysis

Thermogravimetric Analysis (TGA) is a technique to monitor the mass change of a sample when it is subjected to a heat flux, under predetermined heating rate and temperature conditions. The atmosphere is also controlled, since its composition contributes to the mass variation, given that

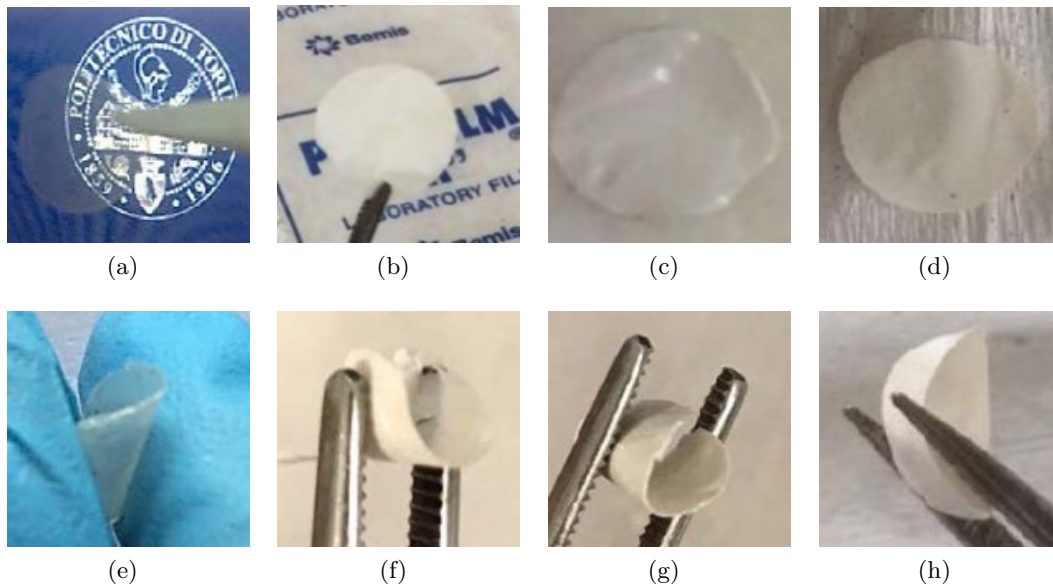


Figure 3.9: Evidence of translucent appearance and flexibility being blend of blank BMA10PEGDA(a,c), BMA10PEGDA38(b,f), BMA10PEGDA63(c,g) and BMA10PEGDA80(d,h)

chemical reactions might occur. Indeed, the gas control can be inert, oxygen, air or a particular mix of elements, depending on what is the scope of the analysis. While the furnace increases or decreases the temperature, a precision balance measures the changes in mass, quantifying the loss of water, solvents and plasticizers, decarboxylation, pyrolysis, oxidation, decomposition and weight percentages of fillers. However, the analysis lacks of chemical details about what is happening to the sample during the thermal events. Nevertheless, TGA is very useful, above all in case of polymeric samples, in order to assess their thermal and oxidative stability, their chemical composition within the weight percentages of each components [48], [49]. In light of this, for the purpose of characterizing the as-prepared membranes, the blank (BMA-co-10PEGDA), conjointly to the three membranes with different amount of ZrO_2 , have been inspected by a thermogravimetric instrument (TGA/SDTA-851 instrument, METTLER, Switzerland). Additionally, all the precursors have been individually analysed, namely BMA, PEGDA, and Zirconia, in order to cross-reference precursors and as-prepared membranes. The analysis has been performed in air, between 25°C and 800°C at the heating rate of 10°C per minute. The results are presented in the form of mass variation percentage as a function of the increasing temperature (figure 3.10).

TGA measurements allow one to assess the amount (in weight percentage) of nanoparticles of ZrO_2 that polymers are able to embed, still resulting flexible. Results give mass percentage of zirconia in the three membranes equal to 38%, 63% and 80%, respectively, that's why the three

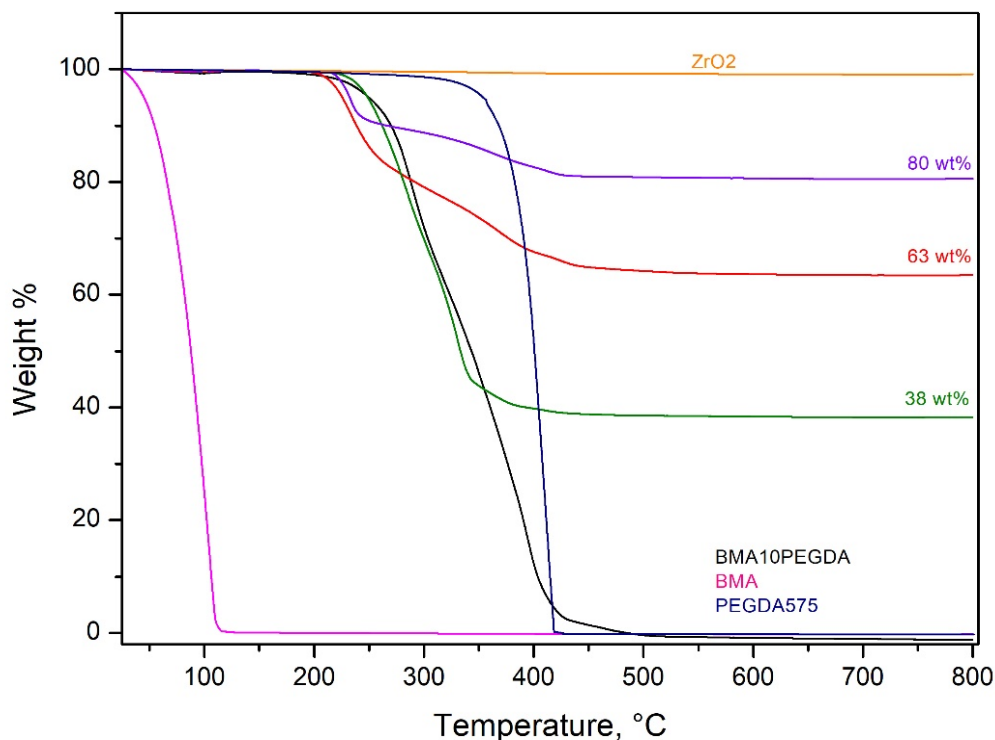


Figure 3.10: Weight percentage vs temperature curves of ZrO_2 (orange line), BMA (pink line), PEGDA (blue line), BMA10PEGDA (black line), BMA10PEGDA38 (green line), BMA10PEGDA63 (red line) and BMA10PEGDA80 (violet line).

membranes are named BMA10PEGDA38, BMA10PEGDA63 and BMA10PEGDA80. Moreover, the highest percentage is the proof of the feasibility of "polymer in ceramic" concept, since the sample keeps being still very flexible and self-standing. All the results are illustrated within the same graph to make comparisons and to better distinguish reactions arising in the samples. Therefore, it can be gathered, about the precursors, that BMA has a low thermal stability and is completely evaporated already at 100°C; PEGDA decomposition starts around 400°C, when the thermal energy is enough to break down C-C bonds; while, as expected, zirconia nanoparticles don't show any changes in their physical characteristics, having stronger molecular bonds. The blank (BMA-co-10PEGDA), instead, is stable until 250°C and completely decomposed at 400°C, as expected, considering its composition in BMA and 10 wt% PEGDA. Interesting to notice, just for the sake of comprehension, is that, adding zirconia, thermal stability decreases a bit. This is due to the fact that, above a certain amount of zirconia, the latter acts as a catalyst for polymers reacting with air. Those triggered oxidation reactions are distinguishable on the curve by a step

on both the BMA10PEGDA63 and BMA10PEGDA80 curves, near a temperature slightly below 250°C.

3.2.2 Fourier transform infrared spectroscopy

Fourier transform infrared spectroscopy (FTIR) is a very useful test to identify and characterize materials. The FTIR instrument basically consists of an infrared radiation (IR) source, the sample plate and the detector. A laser applies a beam on the inspected material sample, which can absorb a part of this radiation, converting this energy in vibrational or rotational energy. The theory behind this analysis is that different kind of bonds absorb radiations at different frequencies. Hence, a detector collects all the IR frequencies arriving from the sample, then, an interferometer produces an optical signal, so that, finally, applying the Fourier transformation mathematical technique, a software generates an infrared spectrum. The so-obtained graph displays the infrared light absorbance by the substance, against the wavelength of the radiation that had excited molecular vibration in the substance. The region of interest for this work case is the Mid Infrared (MIR), wherein the frequency is usually expressed as wavenumber $\nu = \frac{1}{\lambda}$, and ranges between 4000 and 200 cm^{-1} . Every molecule, molecular group and atomic bond has its unique fingerprint, which allows one to identify clearly which one is present in the sample. Detailed speaking, higher is the frequency of the absorbed infrared, stronger is the chemical bond that absorbed it. [50] To this end, all precursors and membranes have been detected by a Nicolet™ iS50 FTIR spectrometer (Thermo Scientific™) equipped with an attenuated total reflection (ATR) tool over the range 4000-400 cm^{-1} with a resolution of 4 cm^{-1} at room temperature. The FTIR analysis gave in

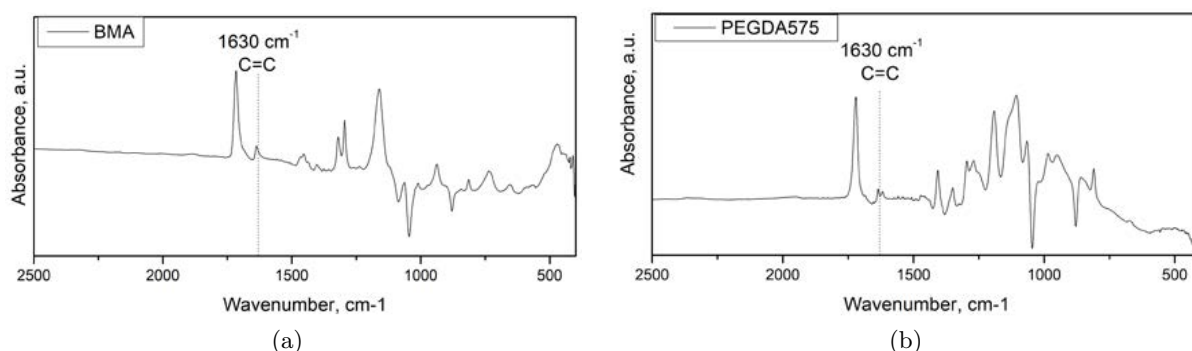


Figure 3.11: Absorbance spectrum of monomer BMA (a) and crosslinker PEGDA (b). The peak typical of vinyl group is underlined.

output infrared spectrum absorption for a qualitative analysis of polymer starting materials and

finished products. By inspecting at which wavenumber a certain peak is present, the spectrum gives information about the presence of specific functional groups. Considering the involved materials, that are polymer with vinyl and methyl groups, absorption bands of interest are in correspondence of about 1710 cm^{-1} for C=O, 1630 cm^{-1} for C=C and 1100 cm^{-1} for C–O–C [50]. As noticeable in figures 3.11, these three peaks prevails over the others. At this point, making a contrast, it can be assessed whether the polymerization of monomer and crosslinker has been accomplished or not. Still, also the spectrum of zirconia nanoparticles has been detected, in order to dismiss any possible ZrO_2 contribution in BMA10PEGDA38, BMA10PEGDA63 and BMA10PEGDA80 spectrum. Indeed, it can be seen in figure 3.12, that its bond are too strong to visibly vibrate, unless for very small wavenumber (high frequency).

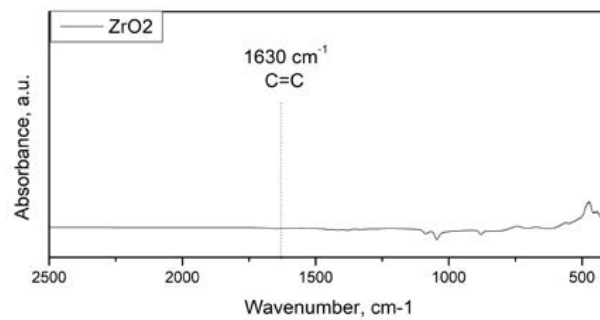


Figure 3.12: Absorbance spectrum of Zirconia nanoparticles. Infrared radiation don't have enough energy to excite ZrO_2 bonds

Checked that, inspection of figures 3.14 reveals the fading away or even total disappearance of C=C bond peak at 1630 cm^{-1} in all the membranes, with and without zirconia particles. This confirms the complete conversion of BMA and PEGDA, since no consistent number of vinyl group is present. [29]

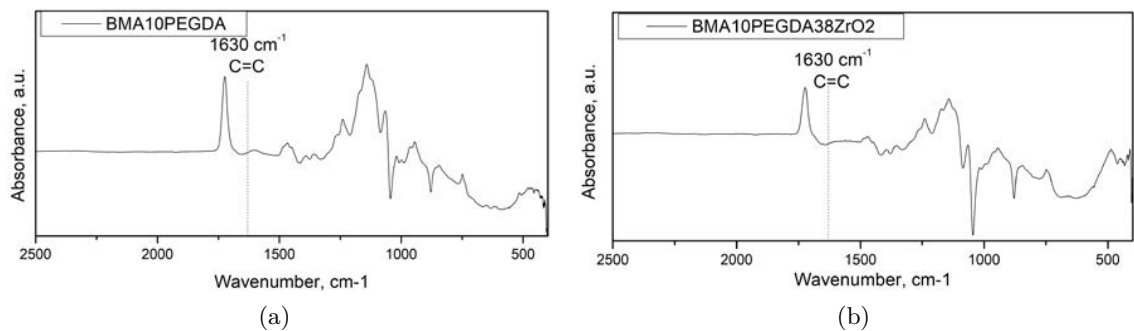


Figure 3.13: FTIR spectra for BMA10PEGDA (a), BMA10PEGDA38 (b), none of them shows the peak at 1630 ascribed to the stretching vibration of C=C bonds.

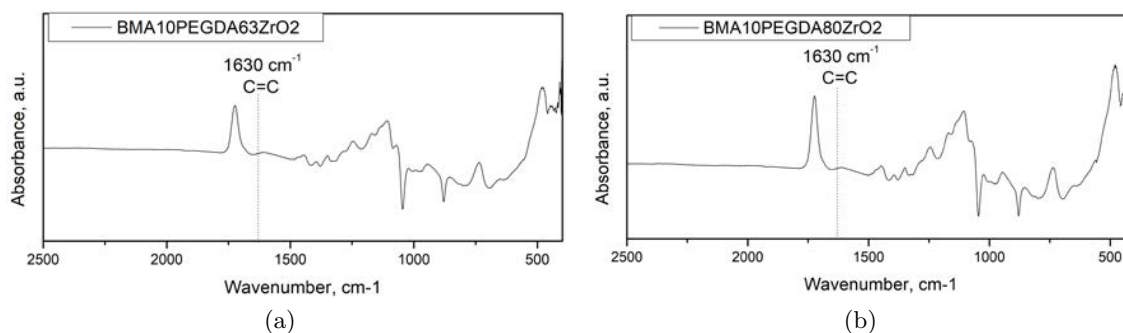


Figure 3.14: FTIR spectra BMA10PEGDA63 (a), BMA10PEGDA80 (b), none of them shows the peak at 1630 ascribed to the stretching vibration of C=C bonds.

3.2.3 FESEM Scanning

A Field Emission Scanning Electron Microscopy (FESEM) is used to visualize small topographic and morphologic details of surfaces and cross-sections of samples. It can examine structures even as small as 1 nanometer. The ability of FESEM to characterize materials is based on the same principle of the human eye: both of them use light as a mean to probe an object. What is different is the radiation wavelength, and thus the resolution of the image. The radiation used by a FESEM is an electron beam (with a wavelength $\lambda = 0.000004\mu\text{m}$) which if accelerated with 20-30 kV voltage can ensure images resolution of even less than 1 nanometer. Indeed, the working principle of this instrument consists of an electron beam, released by a field emission source (the electron gun), while accelerated by a high potential gradient, and sent into the electron column. In there, a system of lens and mirrors deflects and focusses the ray in order to bombard uniformly the sample. As a result, impacting electrons and samples electrons will interact in different ways. Depending whether the collisions are elastic or anelastic, the object will emit backscattered electrons or secondary electrons. The angles and velocity of the emitted radiation, provide information about the shape, the structure and the atomic number of the irradiated material components. Therefore, a detector gathers all these information and produces an electronic signal which is amplified and turned into a high resolution image. Additionally, in the electron column is usually created the vacuum, in order to avoid any gas molecule interacting with the electron beam and emitted electrons, preventing corrupted scans. [51] In this characterization, the morphology of the zirconia nanoparticles and membrane samples have been observed by the Field Emission Scanning Electron Microscopy (FESEM), ZEISS Supra. In figure 3.15 can be observed the regular spherical shape of zirconia particles, with around 50 nm of diameter. To pursue, the surface and cross-section images

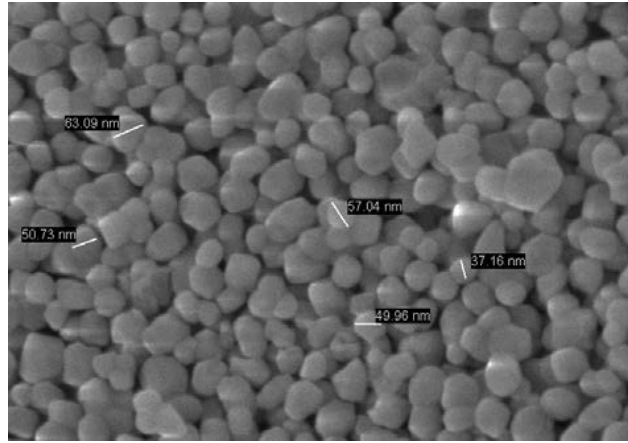


Figure 3.15: FESEM picture of pristine ZrO_2

of the extreme cases BMA10PEGDA and BMA10PEGDA80 have been compared. The pictures (a) of 3.16 shows BMA10PEGDA morphology which results globular, probably because of some gases release, occurred during the membrane preparation at temperatures exceeding the BMA thermal stability. By contrast, in image (b), a solid mix of nanoparticles and polymer matrix is observed.

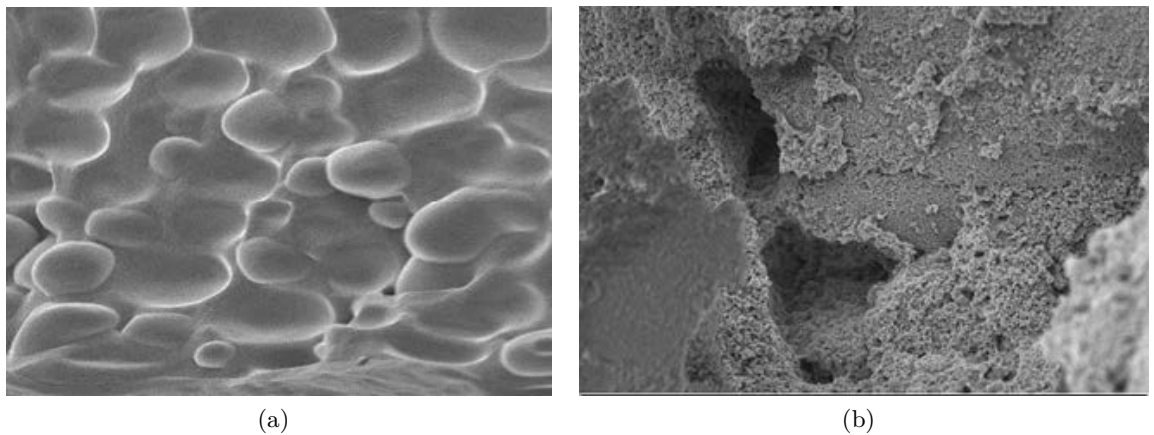


Figure 3.16: FESEM images of BMA10PEGDA (a) and BMA10PEGDA80 (b) cross-sections.

In figure 3.17, surfaces appear for the blank membrane (a) very smooth, whilst for the one with 80 % wt of ZrO_2 (b) a very regular agglomeration of particles covered by a thin polymeric layer.

In last, FESEM scans allowed to obtain a very precise measure of the membranes thickness, which are in average 10 μm and 60 μm for BMA10PEGDA and BMA10PEGDA80 respectively (3.18)

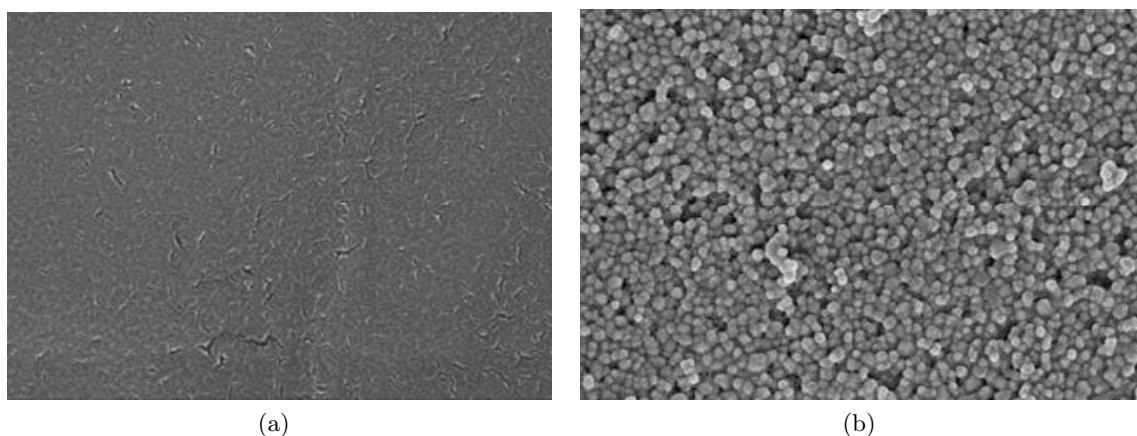


Figure 3.17: FESEM images of BMA10PEGDA (a) and BMA10PEGDA80 (b) surfaces.

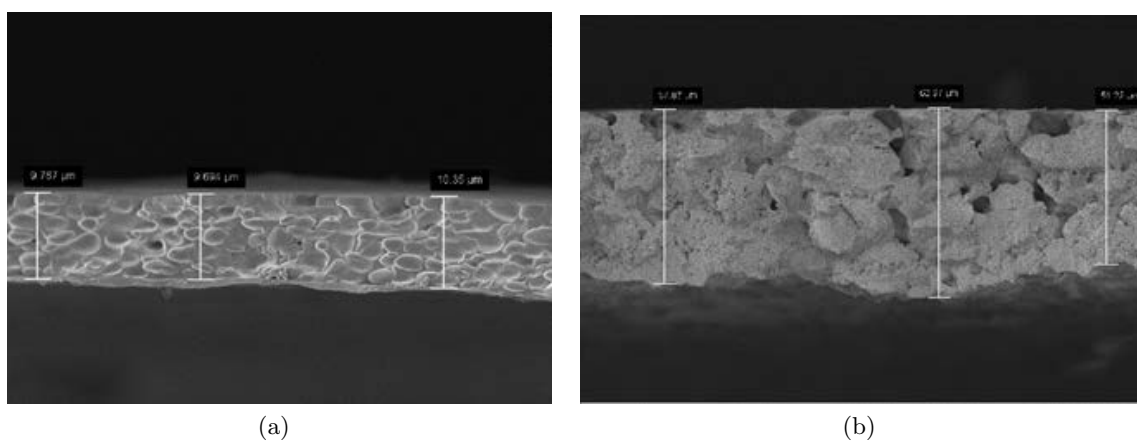


Figure 3.18: FESEM images of BMA10PEGDA (a) and BMA10PEGDA80 (b) cross-section, with thickness measurements.

3.2.4 X-Ray Diffraction

The X-ray diffraction analysis (XRD) is a technique used in materials science to identify crystalline phases and orientation, to determine structural properties of materials and atomic arrangements; it also provides information about deviation of actual structures from ideal one, which may lead to internal stress. It has a working principle very similar to the FESEM: a electrons source sends on the sample X-rays, which are scattered at electrons of the atomic shell of the sample. By measuring the intensities and scattering angles of the X-rays emitted by the inspected material, a diffraction pattern is obtained, and it is representative of the material structure. The diffraction angles θ of emitted rays are collected and sent to a photomultiplier, that provides in output a voltage difference to generate a current, which is used by a computer to translate results in a graph. The resulted one shows on the vertical axis the intensity of rays emitted for a certain angular position

and on the horizontal axis the angular position expressed by 2θ . [52] In this work, XRD diffraction patterns has been gathered for 2θ ranging between 5° and 90° , with a counting time of 10 s per step and 0.03° step size, using a PANalytical X'Pert (Cu K α radiation, $\lambda = 0.154187$ nm) diffractometer with a 2D solid state detector (PIXcel). As already mentioned in paragraph [Materials of interest](#), the total absence of crystallinity is preferred in order to fully exploit the polymer potential as electrolyte. Although, they do have a certain amount of crystalline phase, thus the first step was to verify that, by performing the XRD test on a blank BMA10PEGDA. Figure 3.19 clarify the

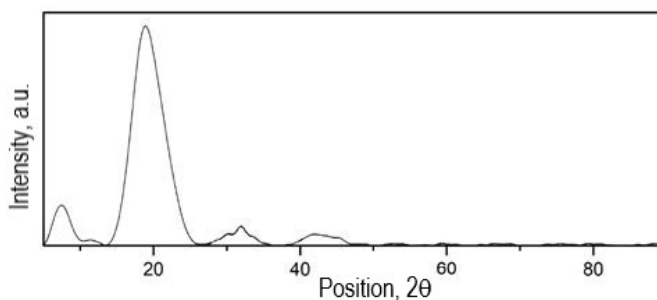


Figure 3.19: XRD spectra for BMA10PEGDA, with a visible peak in correspondence of 18.80° .

presence of crystallinity, proven by the peak in correspondence of $2\theta = 18.80^\circ$ degrees $2\theta = 18.80^\circ$, characteristic diffraction angle of crystallinity in polymers. Recalling the paragraph [Materials of interest](#), the agglomeration of ceramic particles during membrane preparation freezes the polymer structure to the amorphous phase, avoiding the crystalline phase formation. In order to verify this goal, firstly, zirconia pattern also was verified, as illustrated in 3.20, and compared with a spectra from the literature (blu bars). At this point, all the necessary data to validate the assumption have

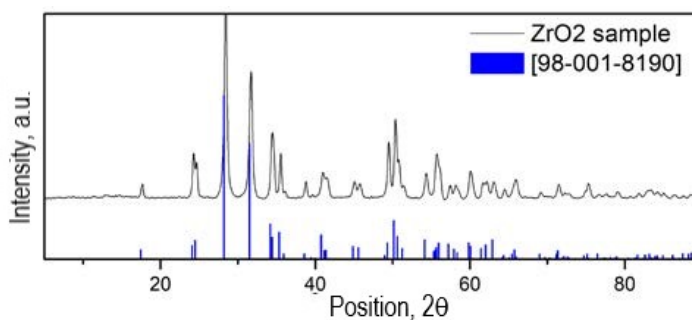


Figure 3.20: XRD spectra for ZrO₂ available in the electrochemical laboratory and for ZrO₂ took from literature.

been gathered. Thus, BMA10PEGDA38, BMA10PEGDA63 and BMA10PEGDA80 have been subjected to the XRD analysis, and spectra results are depicted in figure 3.21, respectively (a), (b) and (c). Curves show almost null intensity at $2\theta = 18.80^\circ$, confirming that no crystallinity has

formed during preparation. The remaining pattern is practically the unaltered one of the zirconia. ZrO_2 nanoparticles crystallinity has not been affected.

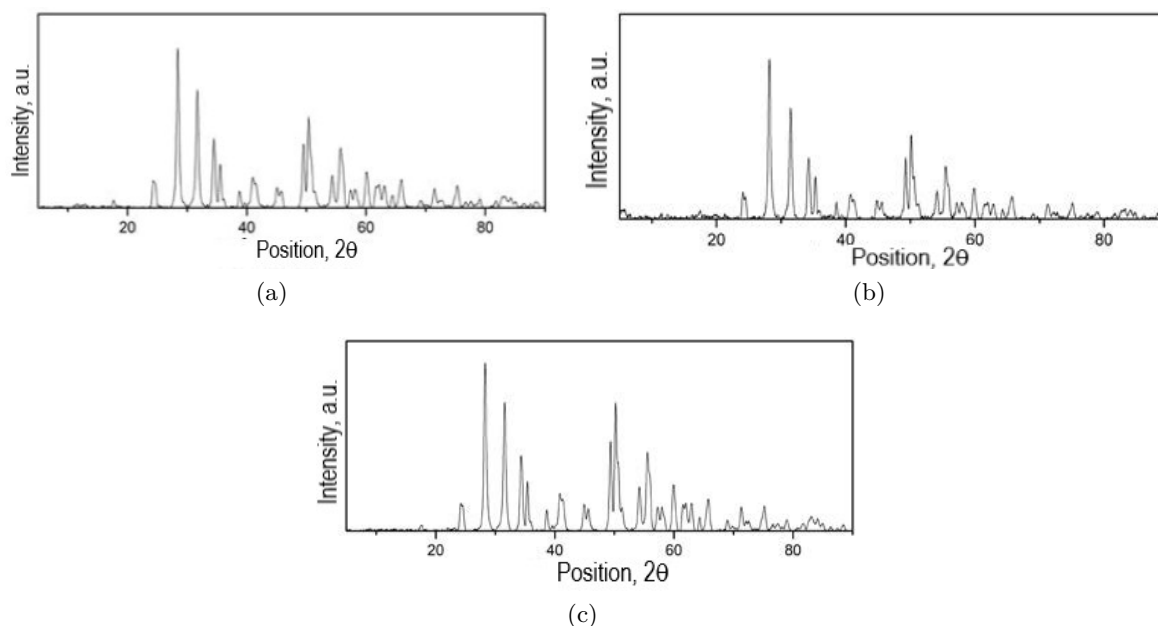


Figure 3.21: XRD spectrum for BMA10PEGDA38 (a), BMA10PEGDA63 (b) and BMA10PEGDA80

3.3 Electrochemical characterization

3.3.1 Electrochemical impedance spectroscopy

Once the membranes have been characterized by their physic-chemical parameters, and have fulfilled some expectations, including polymer flexibility (up to 80 wt% of ceramic particles agglomerated, still maintaining flexible and translucent appearance), achievement of complete polymerization and hindering of crystallinity rise, the electrochemical characterization has to follow. In particular, first step is to check whether the ion conductivity is enhanced, as predicted, or not. For this purpose, Electrochemical impedance Spectroscopy (EIS)(paragraph [Exchange current density](#)) has been performed. In order to investigate only the conduction ability of the electrolyte, El-Cell (ECC-Std)(paragraph [Cell assembly](#)) only made of membranes, swollen with liquid EC:DEC 1:1 LiPF_6 1M, and sandwiched between the stainless steel components of the cell, working as blocking electrodes, have been assembled. Having the cells no porous electrodes or active material-electrolyte interfaces, EIS spectra lack of impedances due to charge transfer at the interface and diffusion in porous electrode. Thus, their Nyquist graphs only consist in straight lines touching the horizontal

axis, and this is due to the fact that only the Warburg impedance, ascribed to the mass transfer, is present. The intersection point with the axis is the value of R_ω , the resistance of the electrolyte. Hence, EIS measurements, between 100 kHz and 1 Hz at open-circuit-potential, using a CHI potentiostat instrument, were conducted on the EL-Cells between 25 and 70°C. The measured R_ω have been used in order to calculate membranes ion conductivity σ [S/cm] at different temperatures through the equation:

$$\sigma = \frac{l}{AR_\omega} \quad (3.1)$$

where l is the membrane thickness [cm] and A is electrolyte discs surfaces [cm^2]. In order to contextualise the results, also for the Celgard separator the analysis has been performed. From figure 3.22 very interesting conclusions can be drawn. First thing, all membrane behaviours

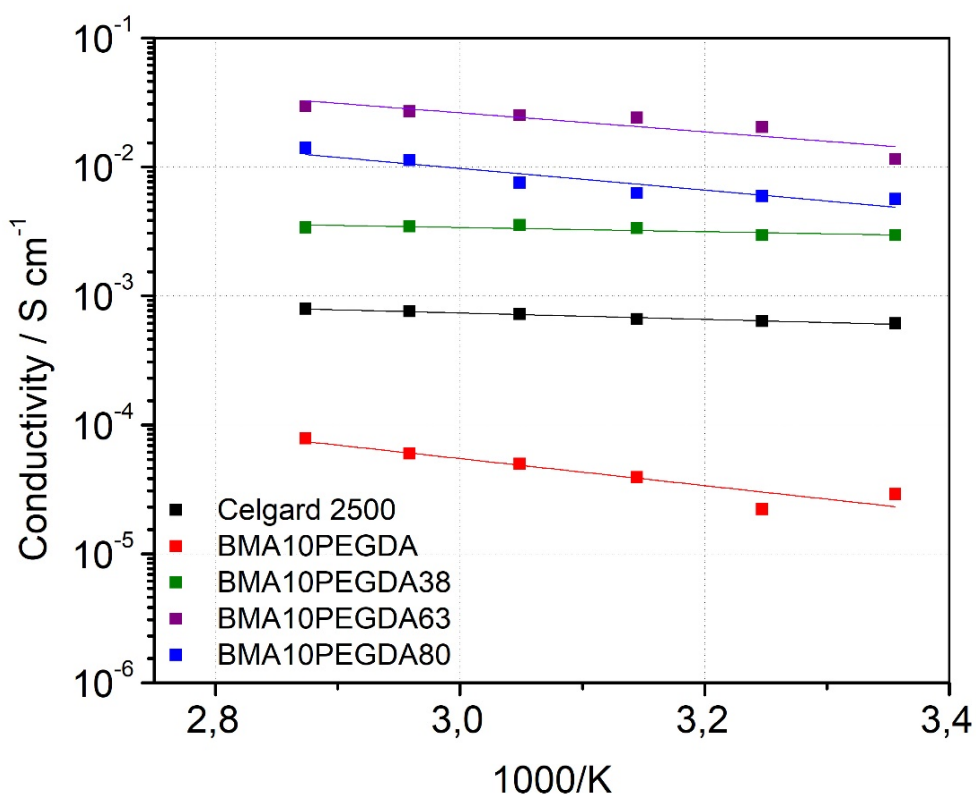


Figure 3.22: Ion conductivity results at different temperatures for all the membranes: Celgard (black line), BMA10PEGDA (red line), BMA10PEGDA63 (green line), BMA10PEGDA80 (blue line)

obey to the Arrhenius law: transport phenomena are improved for higher temperature. Blank BMA10PEGDA shows the lower σ among the others. The conductivity of the polymer matrix is increased for every composite membranes, achieving almost three order of magnitude increment

for the BMA10PEGDA63. The latter confirms that adding inorganic nanosized particles enhances the CGPE electrolyte performance due to the suppression of crystalline phases (verified by XRD analysis) and the ability of ZrO_2 of conducting Li_+ ions. But, interesting to notice is that an optimal amount of zirconia exists, in fact, for the BMA10PEGDA80 the ion conductivity is slightly lower than BMA10PEGDA63. The latter can be explained by the fact that a high number of solids increases the total interface area between crystal or grains, namely the grain boundary (GB). And, since ions diffuse more easily inside the particle than on the grain boundaries, too much grains lower a few the ion conduction. Given these consideration, only the best performing membrane, that's the one with 63 wt% of zirconia, has been further characterized, and it is called only Composite Gel Polymer Electrolyte (CGPE), instead of BMA10PEGDA63, from now on.

3.3.2 Linear sweep voltammetry

As widely explained in paragraphs [Lithium metal battery](#) and [Composite Gel Polymer Electrolyte](#), the stability window of an electrolyte is a crucial factor to be checked for the safe operation of a battery. Especially when dealing with high potential batteries, the proper electrochemical stability window is not a simple requirement to fulfil. For this reason, the voltage range bearable by the proposed CGPE has been evaluated through a Linear Sweep Voltammetry (LSV) test. The latter is an electrochemical analysis method that scans linear voltage with a chosen scan rate, inside the potential interval of interest, and measures the current in output, giving in return a curve of the response current over the increasing voltage. Results give informations about the electrolyte stability: if a current peak is recorded for a certain voltage, once it has been increased of the scan rate, this means that the cell has undergone to oxidation or reduction. If instead, while rising the cell potential, no sharp changes in current occur, it can be said that the electrolyte is electrochemically stable for that potential range. [54] Therefore, an El-cell (ECC-Std), consisting of its stainless steel base as current collector and working electrode, the swollen BMA10PEGDA63 as electrolyte, and lithium metal as both reference electrode and current collector, has undergone to an LSV test, in the potential range from 0 to 6.0 V, at a scanning rate of $0,5 \text{ mVs}^{-1}$ at room temperature. Results have been also compared with the LSV curve of an El-cell (ECC-Std) equipped with the commercial Celgard 2500, impregnated with reference liquid electrolyte, in the place of CPE. [55] Figure 3.23 shows the resulting curve with no changes in current up to 4.5 V, demonstrating that polymer electrolytes can offer a wide stability window, which, in this

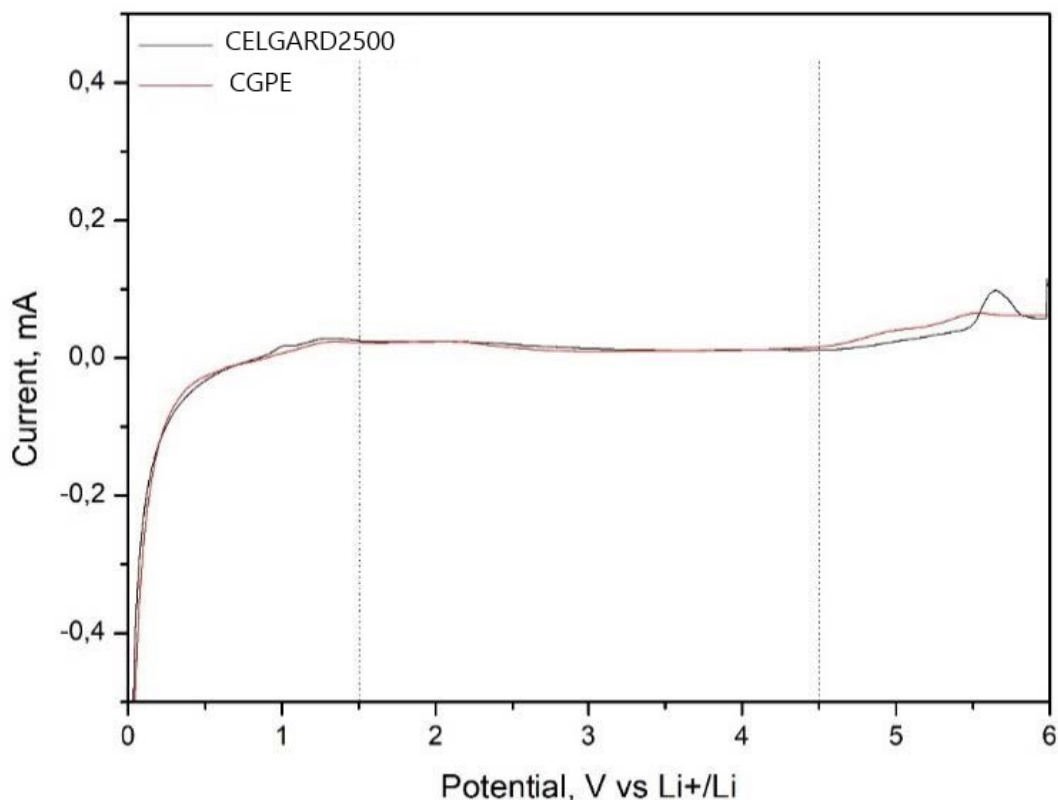


Figure 3.23: LSV for CPE and Celgard in the potential range from 0 to 6.0 V. Stability window is mapped out with two vertical dashed lines.

experiment, ranges from 1.5 V to 4.5 V, which is very similar to the behaviour of the widely used Celgard. This means that, for voltages higher than 4.5 V, redox reactions occur within the cell, and, given that the current recorded for the CPE is quite low, maybe the polymer decomposition is arising.

3.3.3 Chronoamperometry and EIS

Another significant advantage that a good electrolyte may lead to, is to lessen the ion concentration gradients at the anode interface. Recalling the concept explained above in paragraph 3.1, polymer electrolytes have been reported to perform high transference number because of their free chains motion behaviour [36]. Indeed, having a high ions conducting electrolyte, may also imply to have a high transference number. If it is so, it is less likely for the ion concentrations in the electrolyte to vary. Indeed, a high transference number t_{Li^+} implies that Li-ions flow on an homogenous cross-section and fast enough to promote uniform electrodeposition on the anode, avoiding, thus, dendrite growth. Therefore, Chronoamperometry technique, coupled with EIS measurements,

has been used in order to assess the CGPE transference number. This electrochemical technique consists in applying a potential step at the electrodes. As with all pulsed techniques, the response current shows a high peak which decays slowly until the steady state is reached. The lithium ion transference number t_{Li^+} is computed through the Bruce & Vincent model equation:

$$t_{Li^+} = \frac{I_s(\Delta V - I_0 R_0)}{I_0(\Delta V - I_s R_s)} \quad (3.2)$$

where ΔV is the step potential, I_0 is the initial current peak caused by the step, whilst I_s is the steady state current, along with R_0 and R_s being the initial and the steady state interfacial impedance, respectively. Thus, two symmetrical Li-Li cells, have been assembled for the chronoamperometry. In the first one a CGPE is sandwiched between two lithium discs, in the other one, for the sake of comparison, a Celgard 2500 impregnated with liquid electrolyte, is put in the place of CGPE. Employing a CH Instrument potentiostat, the as-assembled El-Cells (ECC-Std) have been subjected to chronoamperometry with potential step of 10 mV, and combined with EIS measures before and after the cell polarization. The former provides the current I_0 and I_s , whereas from the EIS spectra R_0 and R_s are computed. Figures 3.24 depict the results for the liquid electrolyte

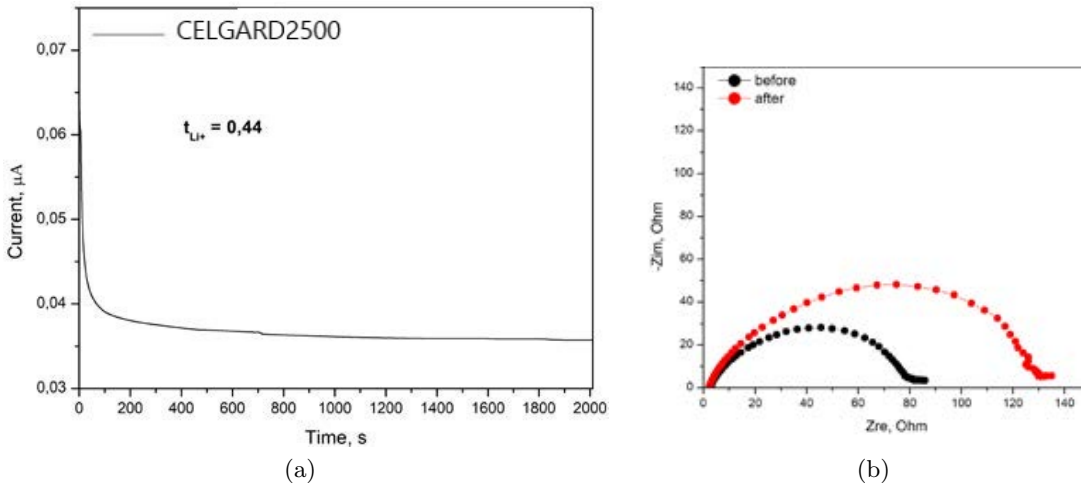


Figure 3.24: Results for the Li|Celgard + liquid electrolyte|Li of Chronoamperometry (a) and impedance measurement (b) before and after the the potential step.

EC:DEC 1:1 $LiPF_6$ 1M on the Celgard2500; herein, is quite noticeable the change in current caused by the potential pulse, as well as, the different EIS spectra as a result of the polarization. On the other hand, the current variation within the cell containing the CGPE is barely visible, and the polarization from EIS measurements is very low. The evolution of the response current with time reflects the rate of creation of concentration gradient of the electrolyte near the electrode. Thus,

CGPE transference number is expected to be higher, which actually is, with a value of $t_{Li^+} = 0.48$, slightly higher than the celgard impregnated, equal to 0.44. This is a noteworthy achievement,

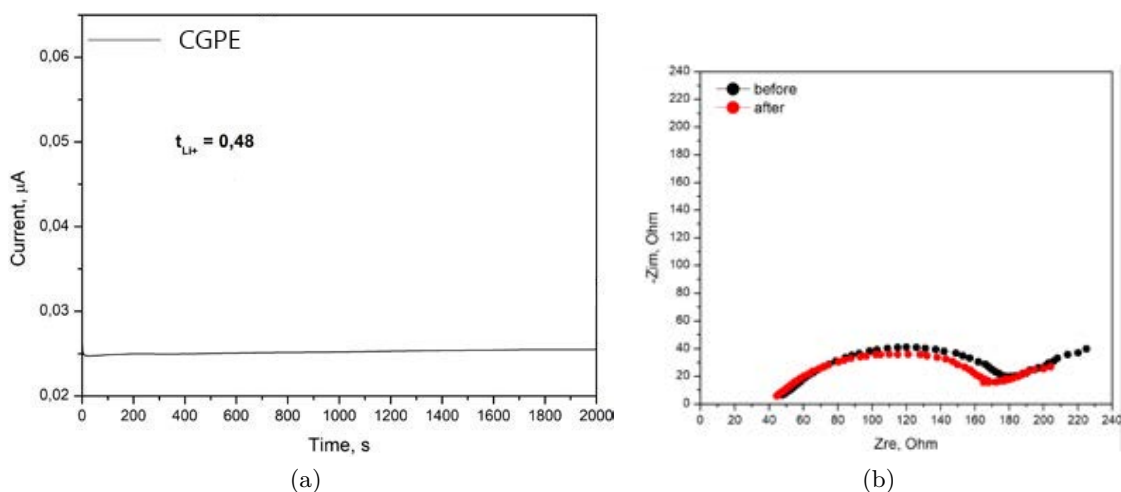


Figure 3.25: Results for the Li|CGPE|Li of Chronoamperometry (a) and impedance measurement (b) before and after the the potential step.

since this enhancement, which can lessen critically the dendrite formation, is the confirmation of the compatibility of ZrO_2 nanoparticles with cross-linked matrix, creating, as expected, preferential pathways for ions.

3.3.4 Galvanostatic cycling and EIS

The Galvanostatic cycling analysis is a constant current method based on measuring the potential changes over time under constant current charge and discharge. Performing this particular test is the last electrochemical characterization step to do, in fact, it is devoted to verify whether all previous assessed enhancements of parameters, achieved for the membrane, are actually effective against the lithium dendrite growth or not. For this purpose, different Li/Li symmetrical configurations, with membranes sandwiched in between, have undergone to a Galvanostatic cycling, followed by EIS measurements, in order to investigate the benefits of CGPE on the lithium ion plating and stripping phenomenon. For the analysis at CH Instrument potentiostat, three different El-cells (ECC-Std) have been assembled as follow:

- 1) Li/Celgard2500 + Liquid electrolyte EC:DEC (1:1) LiPF₆ 1M/Li
- 2) Li/blank BMA10PEGDA + Liquid electrolyte EC:DEC (1:1) LiPF₆ 1M/Li
- 3) Li/CPE + Liquid electrolyte EC:DEC (1:1) LiPF₆ 1M/Li

The analysis is performed through different steps:

- EIS measurement between frequency of 100 kHz and 1 Hz at OCV.
- 10 cycles at current density of 0.1 mAcm^{-2} and related charge/discharge capacity of 0.1 mAhcm^{-2}
- EIS measurement between frequency of 100 kHz and 1 Hz at OCV.
- 10 cycles at current density of 0.5 mAcm^{-2} and related charge/discharge capacity of 0.5 mAhcm^{-2} .
- EIS measurement between frequency of 100 kHz and 1 Hz at OCV.
- 10 cycles at current density of 1 mAcm^{-2} and related charge/discharge capacity of 1 mAhcm^{-2} .
- EIS measurement between frequency of 100 kHz and 1 Hz at OCV.
- 60 cycles at current density of 1 mAcm^{-2} and related charge/discharge capacity of 1 mAhcm^{-2} .

Absolving to the role of reference cell, in figure 3.26 Celgard results are presented. From the potential profile in figure (a) a pronounced overpotential can be noticed, caused by the high resistance due to the formation of native SEI. In the following cycles a slight decrease of the potential needed is noticeable, this is because of the breaks occurring in the SEI during plating and stripping, which frees new native SEI, less resistive and, thus, less voltage requiring. This is the first step toward the dendrite nucleation, which starts to be manifested by the voltage peaks on the curve, arising when the current density is increased in the second stage. Up to the final phase, at 1 mAcm^{-2} , where the contact is lost because of the short circuit caused probably by a dendrite needle that had reached the cathode. The latter is proven by the Bode graphs in figure 3.27 where $\log(Z) [\omega]$ stays constant at a value near to zero. An interesting difference in the potential curve of the blank membrane in figure 3.28 is the more uniform SEI and electrodeposition of ions on the electrode. This behaviour can be possibly proven by the almost stable voltage hysteresis while cycling at 0.1 mAcm^{-2} and 0.5 mAcm^{-2} , unless few important peaks in voltage, which are the overpotentials caused by dendrite growth that, also in this cell, is responsible for short circuit (figure 3.27). The BMA10PEGDA-based cell failure was expected since, even though preferential pathways permitted an homogeneous SEI, without inorganic material addition, the membrane is too low conducting and mechanically scarce, to resist above the limiting current. Thus, finally, all the

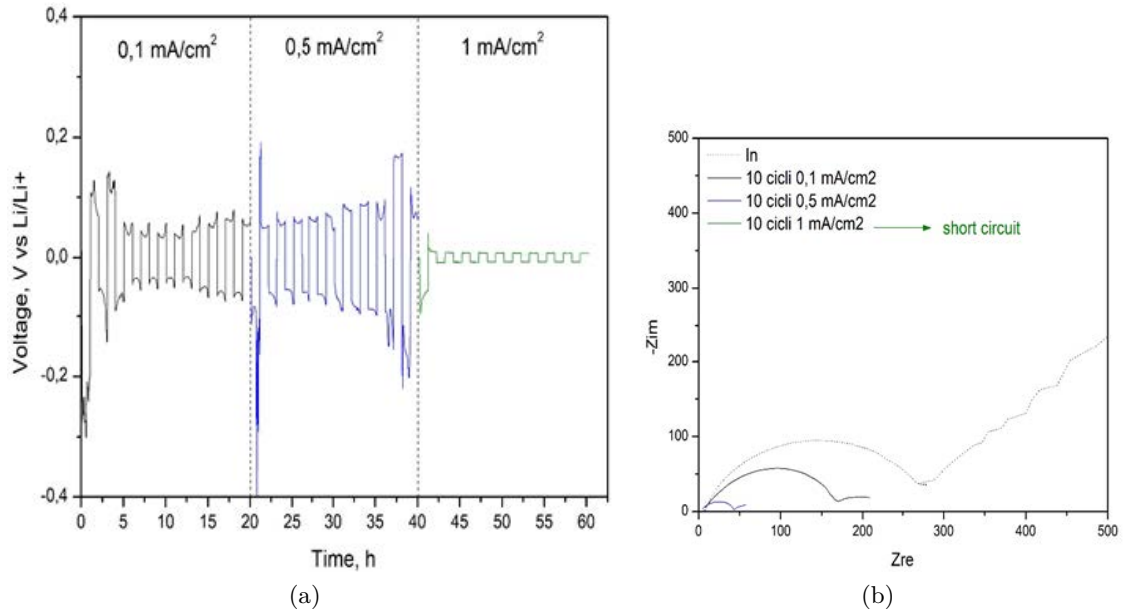


Figure 3.26: Results for the Li|Celgard + liquid electrolyte|Li of Galvanostatic cycling (a) and impedance measurements (b).

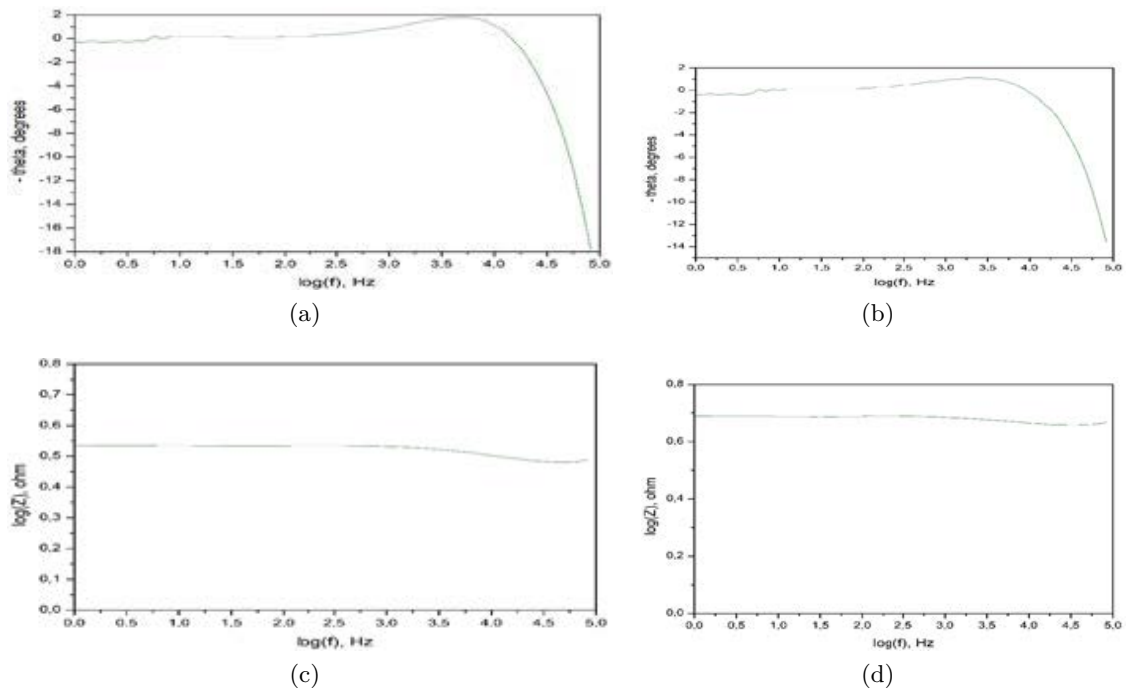


Figure 3.27: Bode graphs of EIS measurements after the short circuit occurred at 1 mA/cm² for the cell with Celgard (a),(c) and the BMA10PEGDA (b),(d).

benefits achieved by the implementation of polymer electrolyte combined with ceramic particles are verified by the satisfying voltage profile of CGPE-equipped EI-Cell (ECC-Std), depicted in figure 3.29. Besides the initial overpotential needed for the SEI formation, this cell excels among the other two in every aspect. Hysteresis of potential is practically the same during the first and

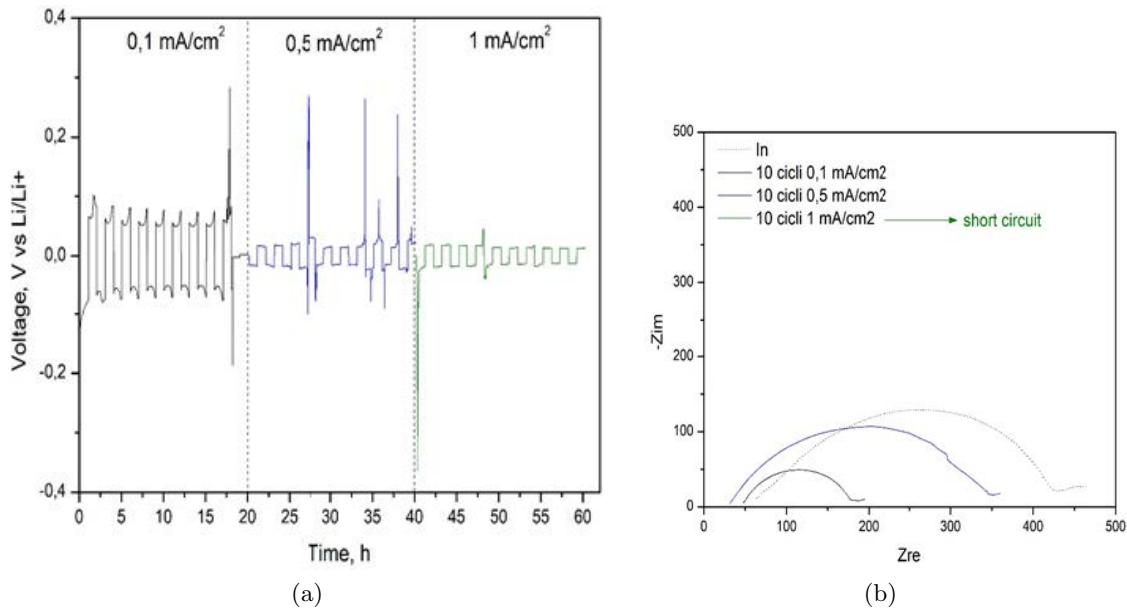


Figure 3.28: Results for the Li|BMA10PEGDA + liquid electrolyte|Li of Galvanostatic cycling (a) and impedance measurements (b).

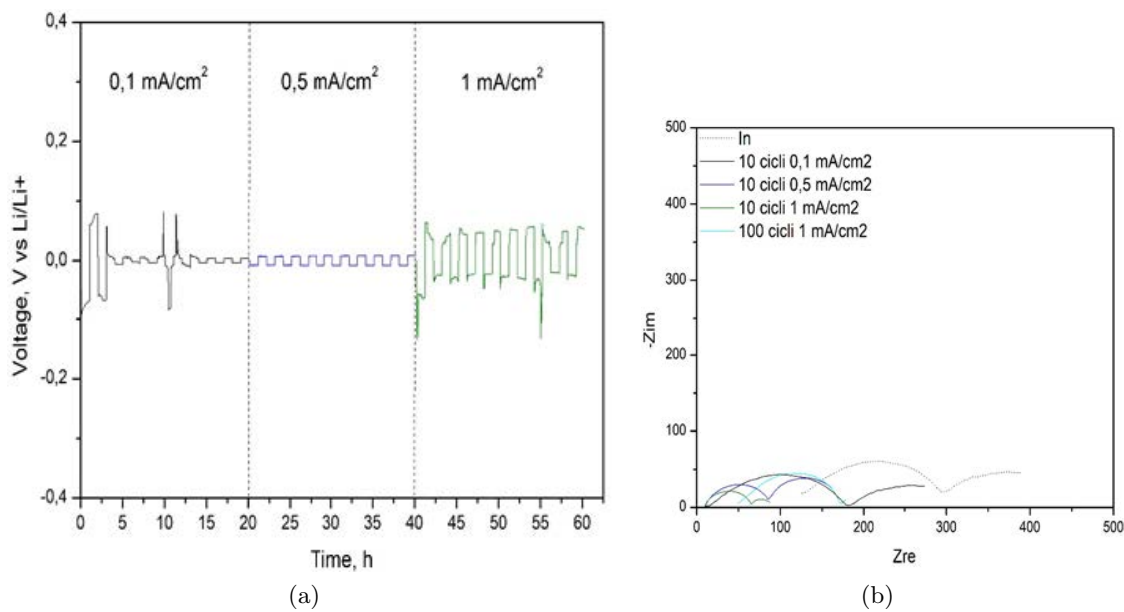


Figure 3.29: Results for the Li|CGPE|Li of Galvanostatic cycling (a) and impedance measurements (b).

second current density step; the overpotential, in general, is very low with respect to the others (almost zero against 0.1 V); some minimum peaks show up only at 1 mA/cm², but, even so, no important dendritic nucleation occurred, as the cell has been able to cycle for 200 hours without short circuiting (figure 3.30). And the latter is the most hoped result toward the ambition of lithium protection.

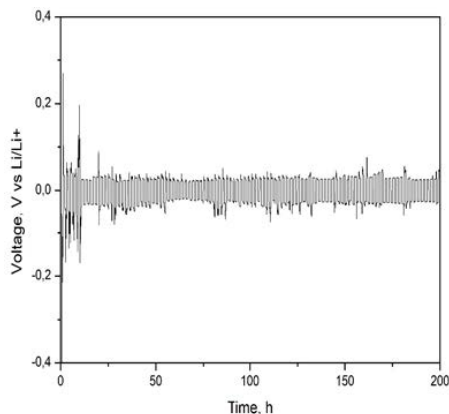


Figure 3.30: Symmetric El-Cel with CGPE cycling for over 200 hours with no short circuit verification.

3.4 Cell cycling

Once the CGPE has been characterized, it is time to verify if a complete cell equipped with the swollen BMA10PEGDA63 is able to cycle and, if it is so, what are its electrochemical performances. The system that is wanted to test is a full El-Cell (ECC-Std) composed by a Li-metal layer as negative current collector and negative electrode, the CGPE as electrolyte, an NMC622 layer as positive electrode and an aluminium foil as positive current collector. For this purpose, a battery tester, an Arbin instrument, has been used in order to test the full cell. It is a multi-channel charge and discharge cycling system for batteries and its working principle consists in applying a constant potential difference or constant current, for different steps, changing, whenever it is desired, the imposed condition of charging, discharging and resting. The latter can be done through the integrated software Arbin's MIT Pro, where it is possible to write a code program, specifying also the scan time for collecting the cell responses to the inputs. Thanks to this instrument, is possible to evaluate cell performances, including charge and discharge capacity, coulombic efficiency, capacity fade, as well as, to perform specific tests, as GITT and PITT. In this thesis, the cells have undergone to galvanostatic condition: a constant current, dependent with the amount of active material of the cathode, in condition of 0.1 C-rate, is applied in order to charge the cell up to 4.4 Volt, then the same negative current discharges the system down to 3 Volt, then again this cycle is repeated 100 times. The voltage response collected by the software is used to generate a graph of voltage profile during cycling versus time. In figure 3.31 are plotted the results for the full cell. Sadly, as can be observed, the system wasn't able to reach the cut-off voltage, behaving in this way at many tries. The two C-rate curves have been introduced in order to draw the attention on the fact that the cell failure occurs at any current density in the same

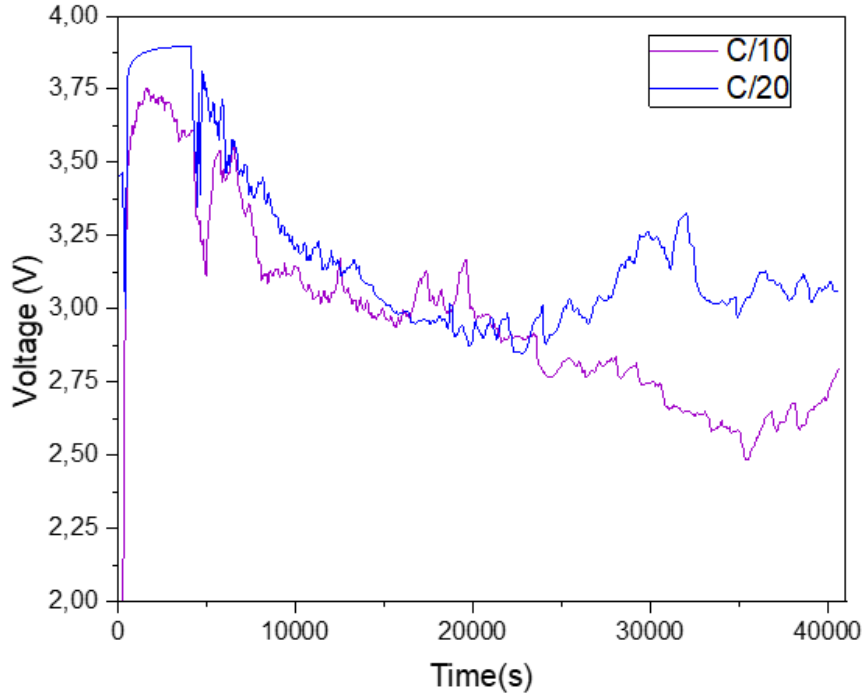


Figure 3.31: Voltage profile versus time for the full cell equipped with the CGPE. Results for C-rate of C/10 (purple line) and C/20 (blue line)

way, making difficult to predict and reproduce the phenomenon. Other different positive electrode materials have been implemented, namely LFP and NMC532, to better investigate the causes of this failure, but the results were almost the same. Thus, the cathode material responsibility can be excluded. But also, surely, it doesn't depend on the high voltage cathode, since the electrolyte is electrochemically stable up to 4.5 V (LSV test, paragraph [Linear sweep voltammetry](#)). Considering that it is experimentally challenging and not always possible to test the mechanical strength of the membrane, due also to the fact that lithium is very chemically unstable, this could be the first hit to the cause of the membrane misoperation. Indeed, Monroe and Newman reached the conclusion that an interface shear modulus, that is twice the Li-anode, is enough to suppress dendrite growth [58], but, unfortunately, in this work it wasn't possible to verify the membrane shear modulus. Keeping that in mind, looking at the random voltage profile, what is possibly happening within the cell is that very small lithium dendrites have grown on Li-anode during charge, and may have penetrated into the membrane, causing micro short circuits. [57] This would explain the arbitrary increase and decrease of voltage: micro shorts may counter acts the delithiation process (charge) by re-intercalating (discharge) lithium ions in the porous electrode through the micro dendrites. The result is a potential fluctuation, where imposed current contributes to the increase of voltage, while micro dendrites to its decrease. A schematic representation of what physically might be

occurring in the cell, and the resulting effect on the potential profile, is shown in figure 3.32

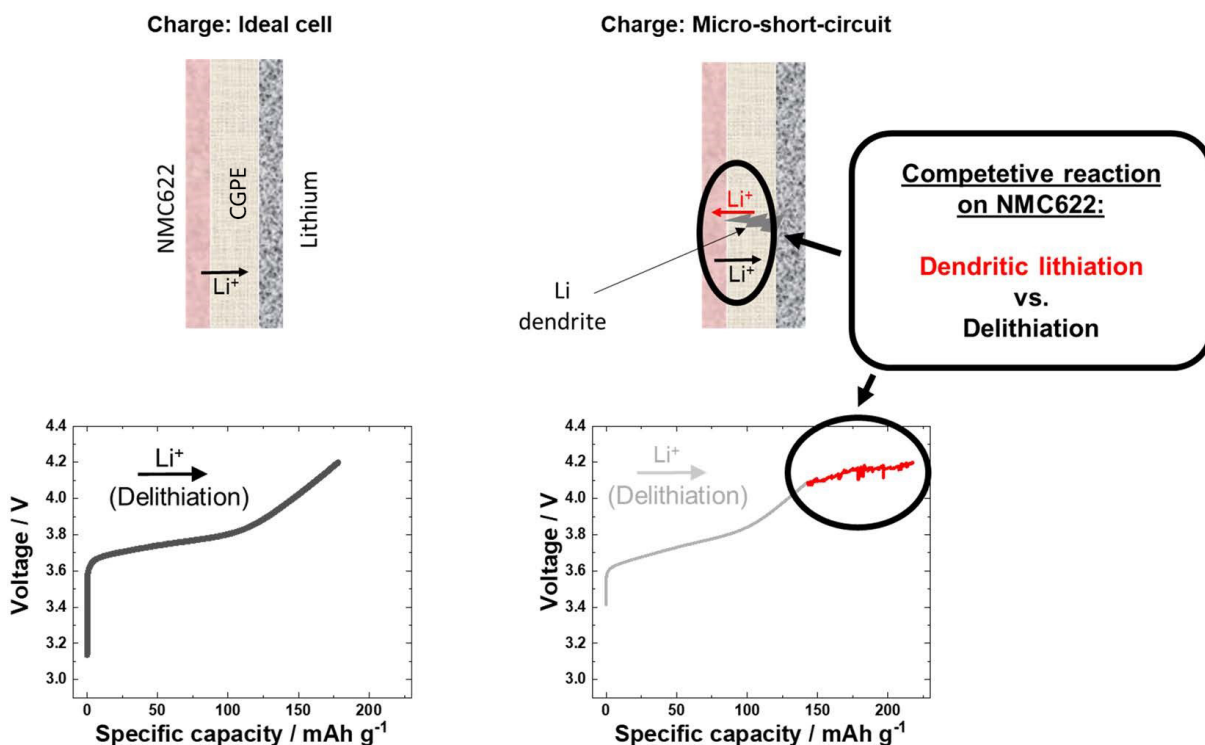


Figure 3.32: Schematic representation of an ideal cell on the left-hand and the intercalation/deintercalation competition causing the voltage noise on the right-hand. Modified figure from [57].

Following the possibility that the failure is due to the mechanical strength, some consideration have been drawn. It has been proven by Homann et al. [57], that increasing the molar weight of the polymer PEGDA doesn't affect in anyway the voltage noise, excluding this attempt. Then, another possibility was to increment the membrane thickness, so that the dendrite path would be too long. But the results showed, were the same. At this point, a mechanical stability observation was attempted: a CPE membrane disc has been swollen into the liquid electrolyte for three days and, afterward, its robustness has been checked. It has been observed that bending the swelled sample, in the same way depicted in figures 3.9 (e, f, g, h) for CPE without swelling, the membrane is very easily broken in two. This occurred in a more evident way, whenever the membrane was thicker. This was probably ascribed to the fact that more liquid electrolyte was incorporated in the membrane affecting increasingly the CPE mechanical properties. Thus, while the embedding of LiPF_6 EC:DEC increase surely the ion conductivity, it undermines the membrane mechanical resistance. Alongside, even if the total amorphous phase characterizing the CGPE allowed to reach unprecedented ion conductivity, it also causes decrease in mechanical stability when swollen with electrolyte. Thus, maybe, a tradeoff between ion conductivity of the amorphous phase and

the mechanical strength of crystalline one, could be a solution. Meanwhile, during this research, in order to increase the membrane strength and decrease the liquid content tangled along the sample thickness, the latter has been further decreased and then the membrane has been pressed at 100°C under a pressure of 10 bar. The as-processed sample were assembled in a full cell and have been galvanostatically cycled in a climatic chamber (Binder) where a temperature of 50°C was maintained. The result are positive since the voltage noise has disappeared in this case, as shown in figure 3.33. Considering that these final results have been obtained when being short of time,

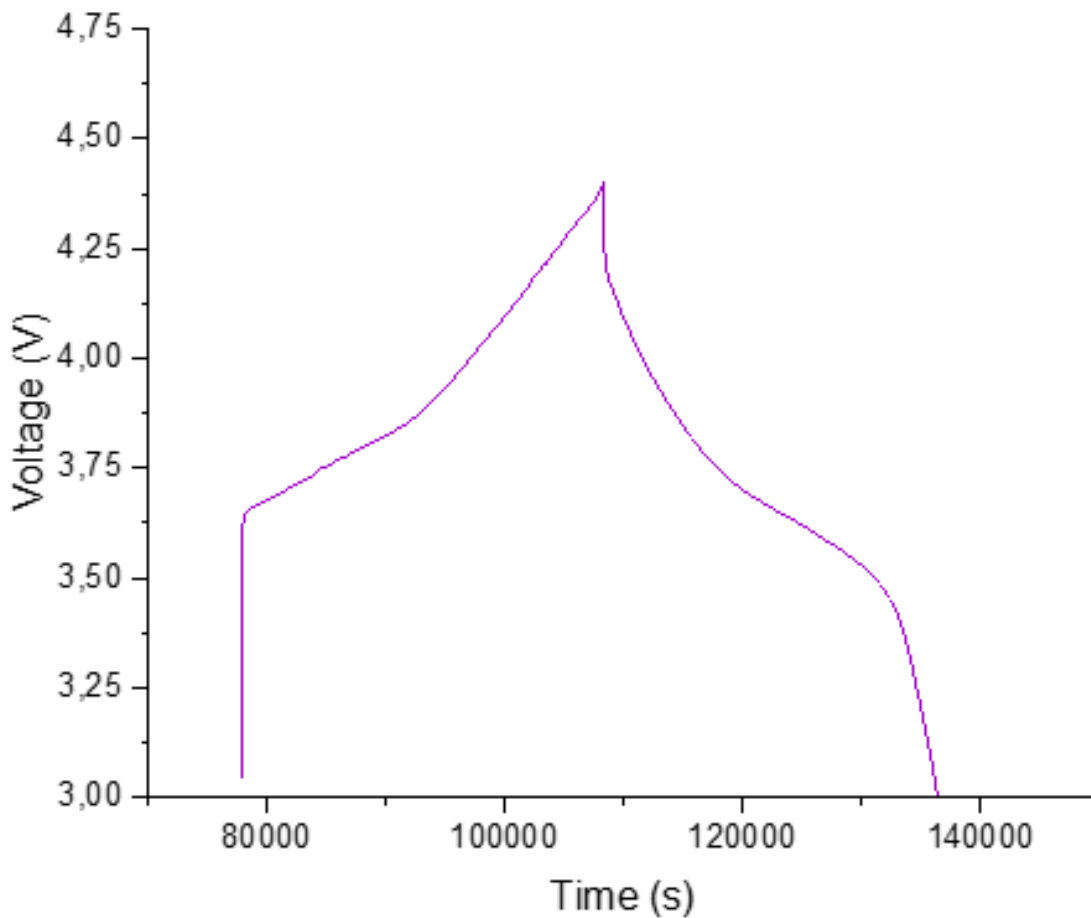


Figure 3.33: Charge and discharge at 50°C of a full cell with pressed CGPE. No voltage noises are present.

hereby comparison between capacity density (mAh/g) for commercial Celgard and pressed CGPE equipped cell cycled at 50°C, are displayed in figure 3.34 for their first 10 cycles. The capacity values for the CGPE is lower with respect to the Celgard, but is worth noticing that it is tending to stabilize, thus to stop fading. Anyway, this can be seen as the proof that mechanical limitation is the cause of the membrane failure. Pressing the membrane discs already gave significant results, achieving the most performing tradeoff between amorphous and crystalline phase, that means

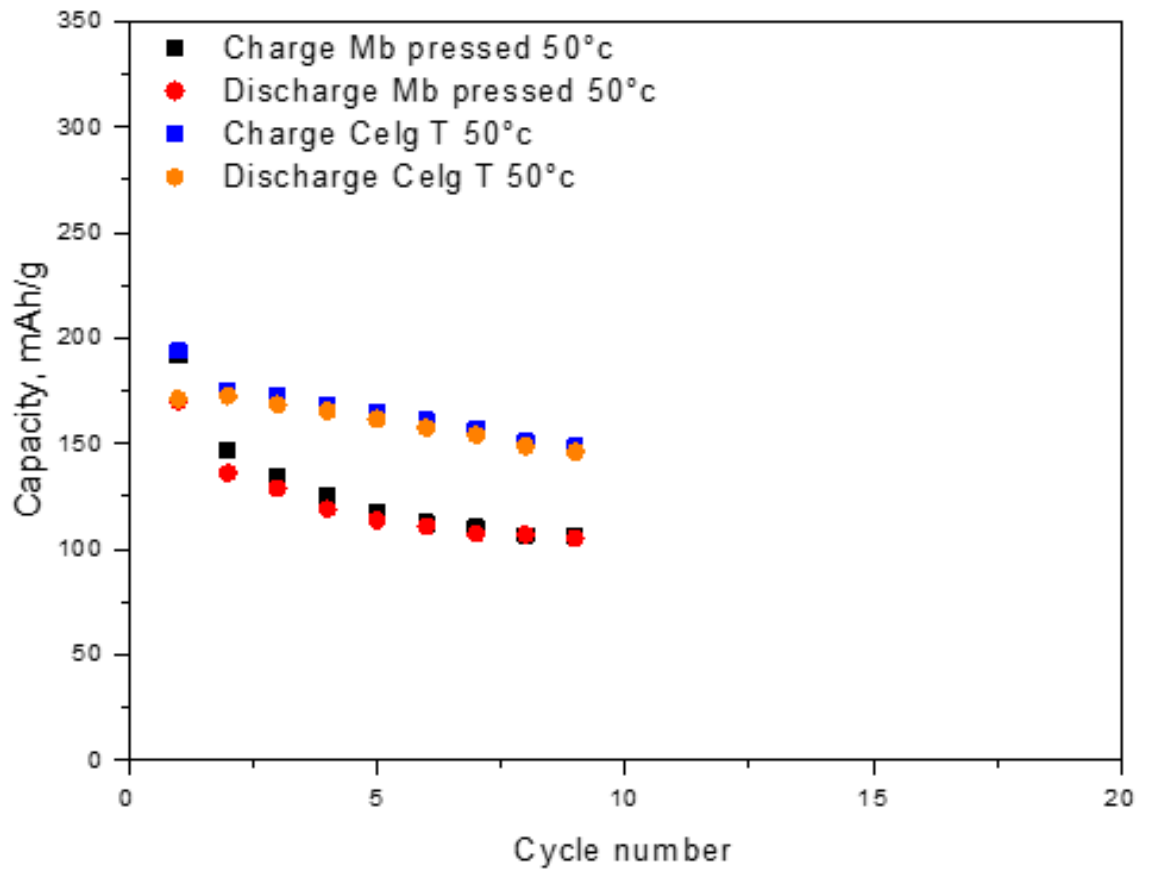


Figure 3.34: Two full cell equipped with Celgard and pressed CGPE are compared by their capacity density evolution through the cycles.

reaching a compromise among ion conductivity and shear modulus. Thus, is left to upcoming works the incipit to improve further this kind of promising polymer electrolyte.

Chapter 4

Conclusions

This research work has been conceived and conducted in order to contribute to the resolution of safety issues related to Li-metal battery. In order to manage possible thermal runaway or, in general, challenging battery working conditions, like high C-rates or long range operation, a mathematical model implementation may be helpful. A model, able to closely predict the performances, as well as, changes in cell parameters under certain operational conditions, is the main instrument to predict any problematic situation, find suited solutions to overcome such issues and design an always reliable battery. Since, when dealing with Li-metal batteries the safety issues became more predominant, a thermal-electrochemical model, inspired by previous modelling work on porous electrodes cell and Li-air batteries, and able to simulate the full discharge phase of a Li-metal cell, has been developed. Since one electrode, the lithium anode, is a conversion hostless electrode, while the other one, the NMC622 cathode, is an insertion hosting electrode, it was a kind of pioneering attempt to model this specific technology on the Comsol software. Indeed, neither the positive electrode material (NMC622) nor metallic Li as anode have been widely studied, up to now, in literature, with respect to NMC811 or NMC111. Therefore, the positive electrode material had to be fully parametrized experimentally, while some approximations and assumptions has been made for the lithium negative electrode. In fact, it has been modelled as a smooth surface, and no changes along its thickness have been considered, neither the possibility of an uneven ion deposition on its surface, both of which definitely involve further parameters and phenomena. Nevertheless, being the purpose of this study foreseeing the behaviour of a cycling cell at its firsts cycles, the model gave accurate and confident results which have been validated with direct measurements. Worth noticing is also that increasing the discharge C-rate, and thus the average temperature of the cell,

the agreement of simulations with experimental data resulted enhanced. This gives credit to an accommodating assumption made, and confirms an important achievement of this work: the former is that lithium plating and stripping heat generation can be neglected for the first cycles as done in the current work, while the latter is the utmost importance of integrating electrochemical model with a 3D thermal analysis in order to consider the effect of temperature on the cell parameters. To conclude, upcoming works may implement a thermal validation for the thermal-electrochemical model, as well as, simulate long life cell behaviour, including in the modelling dendritic and SEI formation phenomena. Speaking of which, the greatest action towards safe and durable Li-metal batteries is to actually suppress the dendritic growth and heterogeneous SEI formation. Polymer electrolyte characteristics are giving the stimulus and the chance to finally overcome these issues. The proposed, prepared and fully characterized (butyl methacrylate)/poly(ethylene glycol)diacrylate (BMA-co-PEGDA) membrane, additioned with inorganic zirconia nanoparticles, and swollen with EC:DEC 1:1 $LiPF_6$, to achieve the characteristics of a Composite Gel Polymeric Electrolyte, gave interesting results. Through many physical-chemical tests, the manageability and flexibility of polymers, compatible with a wide range of possibilities and materials, up to the "ceramic in polymer" concept feasibility, have been proved. Then, the uncertainty, for the polymer electrolyte to exhibit stability window wide enough, has been clarified by lab experiment. Suppressing any crystalline phase, allowed to reach unprecedented ion conductivity, along with competitive transference number, ascribed to the fine polymerization together with the high compatibility of ZrO_2 with the polymer matrix, whose combination creates preferential pathway for ions. Finally, the feasibility of the main purpose of the this research, that are the dendritic suppression and the uniform SEI formation, have been concretized by galvanostatic cycling results in which no short circuits, neither important overpotential, occurred, achieving more than 100 cycles with no damage erasing. For the sake of completeness of considerations, the promising electrolyte has been also cycled in full cells. Unfortunately, it didn't gave rapidly the hoped results, nevertheless, it has been possible to understand the reason of the failure. The latter has been attributed to micro short-circuits via penetrating small Li dendrites, and proved to be due to the mechanical characteristic of the polymer electrolyte. Considering, firstly, that it is not easy, in general, to achieve high shear modulus for polymers, also the difficulties in measuring experimentally this particular parameter, generated some doubt about ascribing the membrane misoperation to the poor Young's modulus. Indeed, having reached such high ion conductivity by the removal of crystalline phase, costed the decline of mechanical resistance, especially when

swollen with liquid electrolyte. Still, just increasing a bit the membrane robustness by pressing it, the failure has been identified and partially overcome. Thus, it is left to the future researches to improve the mechanical performances of the polymer electrolyte, maybe finding the optimal compromise between ion conductivity and shear modulus.

Acknowledgements

This study was carried out as part of the project ULTRA ENERBAT, "Development of ultrahigh energy density battery cells for long range EVs" between FCA-CRF and Politecnico di Torino.

Bibliography

- [1] Reiner K., *Lithium-Ion Batteries: Basics and Applications* Kriffel, Germania, Springer (2018), 415
- [2] J. Newman and W. Tiedemann. Porous-electrode theory with battery applications. *AICHE Journal*, 21, 1975.
- [3] Zubi G., Dufo-López R., Carvalho M., Pasaoglu G., The Lithium-ion battery: State of the art and future perspectives, in "*Renewable and Sustainable Energy Reviews*", June 2018, Volume 89, pages 292-308
- [4] International Energy Agency, *Global EV outlook 2020, entering the decade of electric drive?*, Technology report, June 2020
- [5] Gersdorf T., Schaufuss P., Schenk S., Hertzke P., McKinsey electric Vehicle Index: Europe cushions a global plunge in EV sales, McKinsey & Company, July 2020, 12.
- [6] Golubkov AW., Fuchs D., Wagner J., Wiltsche H., Stangl C., Fauler G., Voitic G., Thaler A., Hacker V., Thermal runaway experiments on consumer Li-ion batteries with metal-oxide and olivin-stype cathodes. *R Soc Chem Adv* ,2014,4,3633–42.
- [7] Golubkov AW., Scheikl S., Planteu R., Voitic G., Wiltsche H., Stangl C., Fauler G., Thaler A., Hacker V., Thermal runaway of commercial 18650 Li-ion batteries with LFP and NCA cathodes – impact of state of charge and overcharge, *R Soc Chem Adv*, 2015,70,57171–86.
- [8] Dingchang L., Yayuan L., Yi Cui, Reviving the lithium metal anode for high-energy batteries, *Nature Nanotechnology*, March 2017, Vol 12, pages 194-206, DOI:10.1038/NNANO.2017.16
- [9] Xin-Bing C., Rui Z., Chen-Zi Z., Qiang Z., Toward Safe Lithium Metal Anode in Rechargeable Batteries: A Review, ACS Publication, *Chemical Reviews*, July 2017, 117, pages 10403-10473 DOI: 10.1021/acs.chemrev.7b00115
- [10] Zhang Y., Qian J., Xu W., Russell S.M., Chen X., Nasybulin E., Bhattacharya P., Engelhard M.H., Mei D., Cao R., Dendrite-Free Lithium Deposition with Self-Aligned Nanorod Structure,

- Nano Lett, November 2014, 14, pages 6889–6896, doi.org/10.1021/nl5039117
- [11] Bin L., Ji-Guang Z., Wu Xu, Advancing Lithium Metal Batteries, Joule, May 2018, pages 833–845, doi.org/10.1016/j.joule.2018.03.008
- [12] Amnesty International, Democratic Republic of Congo: "This is what we die for": Human right abuses in the Democratic Republic of the Congo power the global trade in cobalt, January 2016, Index number: AFR 62/3183/2016
- [13] Chang-Hui Chen et al 2020 J. Electrochem. Soc. 167 080534
- [14] Di Domenico D., Stefanopoulou A., Fiengo G., Lithium-Ion Battery State of Charge (SOC) and Critical Surface Charge (CSC) Estimation using an Electrochemical Model-driven Extended Kalman Filter, January 2009
- [15] Lamorgese A., Mauri R., Tellini B., Electrochemical-thermal P2D aging model of a Li-CoO₂/graphite cell: Capacity fade simulations, Journal of Energy Storage 20, Pisa, Italy, 2018, pages 289-297.
- [16] Gresho P.M., Sani R.L., Incompressible Flow and the Finite Element Method, Wiley, United Kingdom, 1998, page 6.
- [17] Dong-Wong P., Win Won Kim, Jongwong Kim, J. Lee, Physicochemical Behaviors of Oxygen and Sulfur in Li Batteries, Appl. Chem. Eng., Vol. 23, No. 3, June 2012, pages 247-252.
- [18] Jokar A., Rajabloo B., Dèselets M., Lacroix M., Review of simplified Pseudo-two-Dimensional models of lithium-ion batteries, Journal of Power Sources 327, Canada, 2016, pages 44-55.
- [19] Wei Wu, Xinran Xiao, Xiaosong Huang, The effect of battery design parameters on heat generation and utilization in a Li-ion cell, Electrochimica Acta 83, USA, July 2012, pages 227-240.
- [20] Chang-Hui C., Ferran Brosa P., Kieran O'Regan, Dominika G., W. Dhammika W., Kendrick E., Development of Experimental Techniques for Parameterization of Multi-scale Lithium-ion Battery Models, Journal of The Electrochemical Society, 2020, 167 080534.
- [21] K.E. Thomas, R.M. Darling, J. Newman, Mathematical modeling of lithium batteries, in: W.A.V. Schalkwijk, B. Scrosati (Eds.), Advances in Lithium-ion Batteries, Springer Science & Business Media, 2002.
- [22] C.R. Pals, J. Newman, Thermal modeling of the lithium/polymer battery I, Discharge behavior of a single cell, J. Electrochem. Soc. 14 (10), 1995, 3274e3281.
- [23] W.B. Gu, C.Y. Wang, Thermal and electrochemical coupled modeling of a lithium-ion cell, Proc. Electrochem. Soc. 99 (2000) 748e762.

- [24] M. Guo, G. Sikha, R.E. White, Single-particle model for a lithium-ion cell: thermal behavior, *J. Electrochem. Soc.* 158 (2) (2011) A122eA132.
- [25] Galvanostatic Intermittent Titration Technique, Autolab Application Note BAT03, Metrohm Autolab b.v., March 2014.
- [26] Suihan C., Yi Wei, Tongchao Liu, Wenjun Deng, Zongxiang Hu, Yantao Su, Hao Li, Maofan Li, Hua Guo, Yandong Duan, Weidong Wang, Mumin Rao, Jiabin Zheng, Xinwei Wang, Feng Pan, Optimized Temperature Effect of Li-Ion Diffusion with Layer Distance in $\text{Li}(\text{Ni}_x\text{Mn}_y\text{Co}_z)\text{O}_2$ Cathode Materials for High Performance Li-Ion Battery, *Advanced Energy Materials*, 2016, China DOI: 10.1002/aenm.201501309.
- [27] A. Lamorgese, R. Mauri, B. Tellini, Electrochemical-thermal P2D aging model of a $\text{LiCoO}_2/\text{graphite}$ cell: Capacity fade simulations, *Journal of Energy Storage* 20, 2018, Pisa, pages 289-297.
- [28] Jung R., Strobl P., Maglia F., Stinner C., Gasteiger H., Temperature Dependence of Oxygen Release from $\text{LiNi}_{0.6}\text{Mn}_{0.2}\text{Co}_{0.2}\text{O}_2$ (NMC622) Cathode Materials for Li-Ion Batteries, *Journal of The Electrochemical Society*, 165, 2018, A2869-A2879.
- [29] Liping Sun, Han Li, Minglei Zhao, Gengchao Wang, High-performance lithium-sulfur batteries based on self-supporting graphene/carbon nanotube foam@sulfur composite cathode and quasisolid-state polymer electrolyte, *Chemical Engineering Journal* 332, 2018, pages 8-15.
- [30] Min Yang, Junbo Hou, Membranes in Lithium Ion Batteries, *Membranes* 2012, 2, 367-383; doi:10.3390/membranes2030367.
- [31] Zhi-Hong Huang, Dah-Shyang Tsai, Chun-Jun Chiu, Quoc-Thai Pham, Chong-Shyan Chern, A lithium solid electrolyte of acrylonitrile copolymer with thiocarbonate moiety and its potential battery application, *Electrochimica Acta* 365, 2021, 137357.
- [32] Albertus, Christensen, Newman, Experiments on and modeling of positive electrodes with multiple active materials for lithium-ion batteries. *Journal of the Electrochemical Society*, 156(7), A606-A618.
- [33] Wenjiao Zhao, Magnus Rohde, Ijaz Ul Mohsin, Carlos Ziebert, Hans J. Seifert, Heat Generation in NMC622 Coin Cells during Electrochemical Cycling: Separation of Reversible and Irreversible Heat Effects, *Batteries* 2020, 6, 55 doi:10.3390/batteries6040055.
- [34] Qingsong Wang, Jinhua Sun, Guanquan Chu, Lithium Ion Battery Fire and Explosion, *Fire safety science-proceeding of the eighth international symposium, Hefei 230026, 2005, China*, pp. 375-382.

- [35] Monroe C., Newman J., Dendrite Growth in Lithium/Polymer Systems : A Propagation Model for Liquid Electrolytes under Galvanostatic Conditions, *Journal of the Electrochemical Society*, 150, 10, 2003, A1377.
- [36] Zhang Xue-Qiang, Cheng Xin-Bing, Zhang Qiang, Advances in Interfaces between Li Metal Anode and Electrolyte, *Advanced Materials Interfaces*, 2017, DOI: 10.1002/admi.201701097.
- [37] Fenton D.E., Parker J.M., Wright, P.V. Complexes of alkali metal ions with poly(ethylene oxide)., 1973, *Polymer* 14, 589.
- [38] Armand M., Duclot M., Chabagno J. In proceedings of the second international meeting on solid state electrolytes, 1978 (St Andrews, Scotland).
- [39] Dong Zhou, Devaraj Shanmukaraj, Anastasia Tkacheva, Michel Armand, Guoxiu Wang, Polymer Electrolytes for Lithium-Based Batteries: Advances and Prospects, *Chem.* 5, 2019, 2326–2352.
- [40] Feuillade G., Perche P., Ionconductive macromolecular gels and membranes for solid lithium cells., *Journal of Applied Electrochem.* 5,1975, 63–69.
- [41] Skaarup S., West K., Zachau Christiansen B., Mixed phase solid electrolytes.,1988, *Solid State Ionics* 28–30, 975–978.
- [42] F. Croce, L. Persi, B. Scrosati, F. Serraino-Fiory, E. Plichta, M.A. Hendrickson, Role of the ceramic fillers in enhancing the transport properties of composite polymer electrolytes,*Electrochimica Acta* 46, 2001, 2457–2461.
- [43] Dong T., Zhang J., Xu G., Chai J., Du H., Wang L., Wen H., Zang X., Du A., Jia Q., et al. A multifunctional polymer electrolyte enables ultra-long cycle-life in a high-voltage lithium metal battery., *Energy Environ. Sci.* 11, 2018, 1197–1203.
- [44] Monroe C., Newman J., Dendrite growth in lithium/polymer systems a propagation model for liquid electrolytes under galvanostatic conditions. *J. Electrochem. Soc.* 150, 2003, A1377–A1384.
- [45] L. O. Valoen, J. N. Reimers, Transport Properties of *LiPF₆*-Based Li-Ion Battery Electrolytes, *Journal of The Electrochemical Society* 152, 2005, A882.
- [46] Chung D., Ebner M., Ely M. R., Wood V., Validity of the Bruggeman relation for porous electrodes, *Modelling and Simulation in Materials Science and Engineering*, Volume 21, Number 7, 2013, 074009.
- [47] Abboud A. W., Dufek E. J., Liaw B., Communication—Implications of Local Current Density Variations on Lithium Plating Affected by Cathode Particle, *Journal of The Electrochemical Society* 166 (4),2019, A667-A669.

- [48] Bruno Thorihara Tomoda, Patrícia Hissae Yassue-Cordeiro, Júlia Vaz Ernesto, Patricia Santos Lopes, Laura Oliveira Péres, Classius Ferreirada Silva, Mariana Agostini de Moraes, Chapter 3 - Characterization of biopolymer membranes and films: Physicochemical, mechanical, barrier, and biological properties, *Biopolymer Membranes and Films*, 2020, 67-95.
- [49] Yi-Yang Peng, Diana Diaz Dussan, Ravin Narain, Chapter 9 - Thermal, mechanical, and electrical properties, *Polymer Science and Nanotechnology*, 2020, 179-201.
- [50] N. A. M. D. E. J. Jeffrey S. Gaffney, «Fourier Transform Infrared (FTIR)», *Characterization of Materials*, University of Arkansas at Little Rock, Little Rock, Elton N. Kaufmann, John Wiley & Sons, 2012, pp. 1104-1136.
- [51] A. Ul-Hamid, «Components of the SEM,» in *A Beginners' Guide to Scanning Electron Microscopy*, Springer Nature Switzerland, 2018.
- [52] G. C. e. J. O. H. H. Bauer, *Analisi Strumentale*, Padova: Piccin, 1985
- [53] «EL CELL Electrochemical Test Equipment,» [Online]. Available: <https://el-cell.com/>.
- [54] Jung-Ki Park, *Principles and Applications of Lithium Secondary Batteries*, First Edition, 2012 Wiley-VCH Verlag GmbH & Co. KGaA. Published 2012 by Wiley-VCH Verlag GmbH & Co. KGaA.
- [55] Congxiao Wang, Yongyao Xia, Kenichi Koumoto, Tetsuo Sakai, All Solid-State Li⁺Li_{0.5}MnO₂ Polymer Battery Using Ceramic Modified Polymer Electrolytes, *Journal of The Electrochemical Society* 149, 2002, 967-972
- [56] P.K. Alaboina, S. Rodrigues, M. Rottmayer, S.J. Cho, In Situ Dendrite Suppression Study of Nanolayer Encapsulated Li Metal Enabled by Zirconia Atomic Layer Deposition, *ACS Appl. Mater. Interfaces*. 10 (2018) 32801–32808. <https://doi.org/10.1021/acsami.8b08585>.
- [57] Gerrit Homann, Lukas Stolz, Jijeesh Nair, Isidora C ekic Laskovic, Martin Winter, Johannes Kasnatscheew, Poly(Ethylene Oxide)-based Electrolyte for Solid-State-Lithium-Batteries with High Voltage Positive Electrodes: Evaluating the Role of Electrolyte Oxidation in Rapid Cell Failure, *scientific reports nature research*, 2020, 10:4390 | <https://doi.org/10.1038/s41598-020-61373-9>
- [58] C. Monroe, J. Newman, The impact of elastic deformation on deposition kinetics at lithium/polymer interfaces, *Journal of Electrochemical Society*, 2005, 152, 2, A396–A404.
- [59] Yazami R. Maher K., *Thermodynamics of Lithium-Ion Batteries*. In *Lithium-Ion Batteries: Advances and Applications*, Pistoia, G., Ed. Elsevier BV: Amsterdam, The Netherlands, 2014; pp. 567–604.

- [60] Ana Harabor, Cătălin-Daniel Constantinescu, Petre Rotaru, Use of heat flows from DSC curve for calculation of specific heat of the solid materials, *Annals of the University of Craiova, Physics*, January 2013.
- [61] Maheshwari Arpit, *Modelling, Aging and Optimal Operation of Lithium-ion Batteries*, Politecnico di Torino, Eindhoven University of Technology Library, 2018.

Ringraziamenti

Per poter concludere davvero questo elaborato, è per me indispensabile ringraziare tutte le persone che lo hanno permesso.

Innanzitutto, ringrazio il Professore Massimo Santarelli per avermi offerto l'occasione di intraprendere questa bellissima esperienza. Ringrazio la Professoressa Silvia Bodoardo per aver creato un ambiente di studio e ricerca speciale, in cui ogni donna può sentirsi rispettata e valorizzata. È poi per me di fondamentale importanza ringraziare anche Julia Amici, per avermi insegnato che la ricerca è passione e pazienza, Davide Dessantis, per averne avuta con me moltissima di pazienza, e tutto il gruppo di ricerca di elettrochimica, che mi ha fatta sentire sempre inclusa e ascoltata.

I miei più profondi ringraziamenti vanno alla mia stupenda famiglia, che con i loro numerosi controsensi mi ha sempre tenuta a galla. A mio padre e la sua costante apprensione che mi hanno fatta sentire sempre al sicuro; a mia madre e la sua ingenua leggerezza che hanno saputo tirarmi su anche nei momenti più bui; a mia sorella, eterna confidente e ancora di salvezza; a Riccardo e la sua sconfinata gentilezza; alle mie zie e ai mie zii, che sono stati per me più di mille madri e mille padri.

A Miriana, la quale è sempre stata e sempre sarà la mia più grande costante, in evoluzione continua, senza paura di cambiare senza paura di essere quello che è. Grazie per avermi resa una persona migliore, e più forte, per aver sempre avuto le parole e le orecchie giuste, grazie per aver sempre saputo, anche meglio di me, di cosa avessi bisogno. A Giuliano, al vincitore assoluto becchi e Tommy Wiseau per essermi stati accanto sia quando avevo bisogno di piangere che di ridere. Ringrazio Andrè per essere un'inesauribile sorgente di ottimismo e incoraggiamento e per non aver mai fatto una piega davanti ad ogni mia richiesta di aiuto.

A tutti i miei amici che mi hanno accolta a Torino fin dal primo giorno, grazie per tutti i viaggi, il troppo cibo e la comicità cinica, per le giornate intere passate in biblioteca a studiare insieme tra un dispetto e l'altro, grazie per tutte le meme e i pranzi in famiglia, grazie per tutto l'odio e per tutto l'amore che mi avete dato.

Ringrazio infine colui che mi è stato accanto notte e giorno, davanti ad ogni schermo e sopra ad ogni libro, distrazione continua e calamita per lo stress, amore più grande della mia vita; pensavo di essere io ad avere cura di te ma invece sei stato tu a condurmi fin qui. Grazie gattino speciale, grazie Cosetto.